IMPROVING VENTRICULAR CATHETER DESIGN THROUGH COMPUTATIONAL FLUID DYNAMICS

A Thesis Presented for the
Master of Science
Degree
The University of Tennessee, Knoxville

Sofy Hefets Weisenberg
May 2016

Copyright © 2016 by Sofy H. Weisenberg
All rights reserved.

ACKNOWLEDGEMENTS

I would like to thank all those who were involved in supporting the following thesis work. Without their guidance, expertise, and encouragement, this project would not have been possible. Specifically, I would like to thank the following people for their contributions:

My advisor, **Dr. Stephanie C. TerMaath**, who supported me in every step of the research process, as well as provided me with mentoring and guidance in the areas of scientific writing, team building, and leadership. Her efforts make a significant positive impact on those around her, as does her dedication to excellence in research and to creating valuable opportunities for students.

Project collaborators from Oak Ridge National Laboratory: **Dr. Charlotte N. Barbier**, and **Dr. Judith C. Hill**, who served to greatly advance the technical and scientific aspects of this project. Dr. Barbier took on a key role in this project early on, volunteering her time and invaluable expertise in fluid dynamics to help me in constructing substantial parts of the computational model. Dr. Hill provided excellent guidance in the areas of high-performance computing and optimization.

Collaborators from Arkis BioSciences: **Chad E. Seaver**, **Dr. James A. Killeffer**, and **Ishan Gaud**. They shared their valuable knowledge on the medical aspects of CSF shunts and ventricular catheters, as well as offering a unique perspective from the medical device industry.

Collaborators from the thermal fluids research group in the department of nuclear engineering, led by **Dr. Arthur E. Ruggles**, who performed PEPT experiments to allow for validation of the computational model: Cody Wiggins, Seth Langford, Roque Santos, and Nitant Patel.

Undergraduate students from the University of Tennessee, Knoxville who contributed to the research: Justin Splane, Madeline Hayes, Rebecca Kimberlin, Andre Molgaro, Hannah Hajdik, and Grant Rigney. They provided assistance in background research, lab setup, and running the computational models.

Lastly, I would like to thank my loving husband, **Niv Weisenberg**, who gave me the support at home that I needed to dedicate myself to this work. He gave me the strength and inspiration to overcome the challenges I faced during the project.

ABSTRACT

Cerebrospinal fluid (CSF) shunts are fully implantable medical devices that are used to treat patients suffering from conditions characterized by elevated intracranial pressure, such as hydrocephalus. In cases of shunt failure or malfunction, patients are often required to endure one or more revision surgeries to replace all or part of the shunt. One of the primary causes of CSF shunt failure is obstruction of the ventricular catheter, a component of the shunt system implanted directly into the brain's ventricular system. This work aims to improve the design of ventricular catheters in order to reduce the incidence of catheter obstruction and thereby reduce overall shunt failure rates.

Modern CSF shunts are the result of six decades of neurosurgical progress; however, in spite of revolutionary advances in engineering, the ventricular catheter remains largely unchanged in its functionality and performance from its original design. A thorough review of the history of ventricular catheter design, and the contemporary efforts to improve it, have given valuable insight into the challenges still remaining. One of the challenges is to better understand shunt flow in order to improve the flow performance of ventricular catheters. To characterize CSF flow through catheters, this work integrated computational fluid dynamics (CFD) modelling with experimental validation.

A fully-parametrized, 3-dimensional CFD catheter model was developed that allowed for exploration of the geometric design features key to the catheter's fluid dynamics. The model was validated using bench tests and advanced fluid imaging techniques, including positron emission particle tracking (PEPT). Once validated, the model served as a basis for automated, iterative parametric studies to be conducted. This involved creating a coupled framework between the CFD simulations and a parametric analysis toolkit. Sensitivity analyses and optimization studies were performed with the objective of improving catheter flow patterns. By simulating thousands of possible geometric catheter designs, much insight was gathered that can provide practical guidelines for producing optimal flow through ventricular catheters. Ultimately, those insights can lead to better quality of life for patients who require shunts, by reducing ventricular catheter obstruction rates and the need for revision surgeries.

TABLE OF CONTENTS

Chapter 1: Introduction and Background 1
1.1 Introduction 1
1.2 Background: Hydrocephalus 1
1.2.1 What is Hydrocephalus? 1
1.2.2 Hydrocephalus: Current Procedures and Surgical Techniques for Treatment 3
1.3 Background: Cerebrospinal Fluid Shunts 5
1.3.1 Complications and Causes for Shunt Failure 5
1.3.2 Ventricular Catheters and Shunt Obstruction 6
1.4 Research Approach 7
Chapter 2: Literature Review 8
2.1 Overview 8
2.2 Ventricular Catheter Development: Past, Present, and Future 9
2.2.1 Introduction 9
2.2.2 Historical Overview of the Pre-Shunt Era 9
2.2.3 Beginnings of Modern VC Development (1950-1980) 11
2.2.4 Maturation of the Modern VC (1980-2005) 12
2.2.5 Contemporary Ventricular Catheters (2005-2015) 15
2.2.6 Future Directions 18
2.2.7 Conclusion 18
2.3 Existing Fluid Dynamics Studies of Ventricular Catheters 19
2.3.1 Lin, et al. – 2D Computational and Experimental Study 19
2.3.2 Galarza, et al. – 3D Computational Study of 5 Existing Designs 20
2.3.3 Galarza, et al. – Suggestions for New Catheter Designs 20
2.3.4 Galarza, et al. – Parametric Study of Ventricular Catheters 21
2.3.5 How is this thesis innovative? 22
2.4 Physics of Shunt Flow 22
2.4.1 CSF Flow Characteristics In-Vivo 22
2.4.2 Understanding Shunt Flow Rates 23
Chapter 3: Materials and Methods 24
3.1 Overview 24
3.1.1 Computational Resources 24
3.1.2 Experimental Resources 25
3.2 Creating the CFD Model 26
3.2.1 CFD Software: OpenFOAM® 26
3.2.2 Initial 2D Model 27
3.2.3 Expanding the 2D model to 3D 34
3.3 Parameter Studies and Optimization 38
3.3.1 Building an Automated Simulation Framework: DAKOTA 39
3.3.2 Minimizing CFD Execution Time 42
3.3.3 Design Parameters 48
3.3.4 Selecting an Optimization Strategy 51

3.3.5 Running in Parallel 54
3.4 Experimental Validation 56
3.4.1 Water and India Ink Demonstration 56
3.4.2 Nuclear Imaging Test Using PEPT 57
Chapter 4: Results and Discussion 61
4.1 Overview 61
4.2 Parameter Study and Optimization Results 62
4.2.1 Parameter Sensitivity Studies 62
4.2.2 Latin Hypercube Sampling (LHS) Results 65
4.2.3 Optimization Results 67
4.3 Experimental Results 69
4.3.1 Water and India Ink Demonstration 70
4.3.2 Nuclear Imaging Test Using PEPT 71
Chapter 5: Conclusions and Recommendations 74
References 76
Appendix 85
Appendix A: Calculations 86
A-1 Reynold's Scaling Calculation for Nuclear Imaging Test 86
Appendix B: Computational Scripts 87
B-1 OpenFOAM Scripts 87
B-2 DAKOTA Scripts 96
Vita 100

LIST OF TABLES

Table 3.1 Domain size reduction study results 43
Table 3.2 Mesh refinement study results 45
Table 3.3 Solver tolerance study results 47
Table 3.4 Design considerations for parameter ranges 50
Table 4.1 Ranges and Sensitivity Indices of Parameters of Interest 62
Table A-1 Reynold's Scaling Calculation for Nuclear Imaging Test 86

LIST OF FIGURES

Figure 1.1 Diagram showing an implanted CSF shunt and indicating the location of the ventricular catheter within the brain. 3
Figure 1.2 Photograph showing 3 different styles of catheter tips with varying designs of inlet hole configurations. 6
Figure 3.1 OpenFOAM basic case directory file structure, before execution of a solver. *Note*: several files were added to reflect the cases run in this study. Individual case file structure may vary for other types of simulations. 27
Figure 3.2 *Top Left*: Diagram showing the 3D model of a catheter in a ventricular chamber. *Top Right*: Cutting plane used to generate a 2D cross-section of the 3D fluid domain. *Bottom Left*: Example of full 2D cross-section and *Bottom Right*: Example of half of the 2D cross-section. 28
Figure 3.3 *Top*: Example of a 2D fluid domain model (with redundant 3rd dimension along Z axis) showing partial coarse mesh in outer area. *Bottom*: Close-up view of finer mesh generated around the catheter inlet holes area. 30
Figure 3.4 Example of a quarter-section model of the 3D domain, obtained by using 2 cutting planes. 34
Figure 3.5: Results of running simulations in OpenFOAM with identical geometric parameters. *Top*: 2D planar domain velocity field. *Middle*: 3D quarter-domain velocity field (only XY plane shown). *Bottom*: Graph comparing flow rate distributions for the two simulations. 36
Figure 3.6 *Top*: Example of a 3D mesh over the entire domain. *Bottom*: Close-up views of the mesh around the hole inlets. Notice fluid filled holes extend in both +Y and -Z directions.....37
Figure 3.7 DAKOTA basic analysis directory file structure, before execution of an iterative method. *Note*: several files were added to reflect the typical analyses run in this study. Individual file structure may vary for other types of analyses.....40
Figure 3.8 Flowchart loop showing the DAKOTA-OpenFOAM "black-box" or "loosely-coupled” interface format.....41
Figure 3.9 Example of 3 sample domains tested in the domain reduction study. Note that the catheter length and other dimensions were kept constant, while only the chamber size X was changed. 44
Figure 3.10 Example close-up views of inlet hole meshes with increasing mesh fineness number *n*. *Left*: *n* = 5, *Middle*: *n* = 7, *Right*: *n* = 9. 46
Figure 3.11 Example graph of CFD simulation numerical residuals. Ux is velocity in x-direction, Uy is velocity in y-direction (Uz is the same), and p is pressure. Note that the simulation ends at around 675 iterations, converging prior to the 1000 iteration limit.....48

Figure 3.12 Cross-sectional schematic of catheter geometric parameters: a) distance from catheter tip to the first inlet hole, b) first hole spacing, c) subsequent hole spacing, d) interior hole diameter, e) degree of hole tapering, f) catheter wall thickness. 49
Figure 3.13 Coverage of 5-dimensional parameter space, in this case the radii of holes 2 to 6, sampled by 1000 samples using LHS. Parameter space is decomposed to 25 pairs of 2-parameter combinations. 53
Figure 3.14 Schematic of the parallel organization used to run DAKOTA and OpenFOAM on the Darter supercomputer, utilizing 20 compute nodes. 55
Figure 3.15 Water and India ink demonstration setup. 56
Figure 3.16 Photo of the test section and catheter in the bore, connected to the peristaltic pump. 57
Figure 3.17 Schematic of the scaled catheter in the test section within the scanner bore 58
Figure 3.18 Plot of the number of lines of response (LORs) per millisecond, proportional to the positron detections by the PET scanner, over the course of the test. 60
Figure 4.1 Parameter sensitivity study results, showing 2D plots with the parameter of interest as the independent variable and the objective function as the dependent variable. 63
Figure 4.2 Parallel coordinate plot of LHS results on a 5-dimensional parameter space of hole diameters 2-6. *Top*: all 1000 runs. *Bottom*: 6 most successful runs. 65
Figure 4.3 LHS results shown as 2D colored scatter plots of parameter pairs in a 5-dimensional parameter space of hole diameters 2-6. 66
Figure 4.4 Optimized design results. *Top*: CFD results from high-fidelity OpenFOAM simulation. *Mid*: Parameter values for optimized design. *Bottom*: Graph showing relative flow rate distribution among inlet holes, with minimized objective function at 0.30%. 68
Figure 4.5 Water and India ink demonstrations. Images are taken at 1 second intervals. *Left*: Using a 5-hole per row catheter design. *Right*: Using a 8-hole per row catheter design. 70
Figure 4.6 *Top*: Plot of the averaged particle velocity, computed based on a 1 mm x 1 mm grid. Catheter shape is overlayed. *Bottom*: Close-up of proximal hole set region with arrows indicating the influx of particles through the inlet holes. 72
Figure 4.7 *Top*: Comparison of results for the scaled OpenFOAM simulation (left) and averaged experimental particle velocity (right). Catheter shape is overlayed. *Bottom*: Comparison of results for scaled and unscaled OpenFOAM simulations. 73

CHAPTER 1:
INTRODUCTION AND BACKGROUND

1.1 Introduction

The objective of this research is to minimize the potential for the obstruction in ventricular catheters through the characterization and optimization of flow through these catheters. Ventricular catheters are a component of cerebrospinal fluid (CSF) shunt systems, fully implantable medical devices that are used to treat patients suffering from conditions characterized by elevated intracranial pressure, such as hydrocephalus. These catheters are surgically inserted into the ventricular cavities of the brain and therefore operate in a dynamic and complex environment. While in many cases, ventricular catheters and shunt systems save lives and greatly improve the quality of life of patients, relatively high rates of shunt malfunction often require patients to undergo repeated invasive surgeries.

In order to improve the performance of these catheters, this research identifies possible design modifications to reduce the high rates of shunt failure. Specifically, the fluid dynamics of CSF flow through the catheters is explored and characterized in an effort to create more favorable flow conditions which may make malfunctions less prevalent. The physics of CSF flow in the human brain and through shunt systems is dynamic and is affected by many variables. Though this flow is not easily replicated outside the human body, the following work simplifies certain aspects of this complex flow problem to take advantage of fluid imaging techniques and computational simulations for the purposes of design evaluation and optimization.

1.2 Background: Hydrocephalus

1.2.1 What is Hydrocephalus?

Hydrocephalus is a condition primarily characterized by intracranial hypertension due to the excessive accumulation of cerebrospinal fluid (CSF) in the cavities surrounding the brain (collectively called the ventricular system). Widening of the ventricles due to this increased fluid volume results in potentially harmful pressure on the brain tissues [1]. Hydrocephalus has historically been and continues to be one of the leading causes for invasive neurosurgery in modern medicine.

Congenital hydrocephalus, resulting from inherited genetic abnormalities or developmental disorders, is estimated to be present in 3-5 per 1000 live births in developed countries [2], and 1-2 per 1000 live births in the United States [1]. The economic impact of this condition is also alarmingly high, with annual US hospital charges of $1.1 to $2 billion being reported for the treatment of pediatric hydrocephalus alone [3, 4]. Therefore, finding safe and effective treatments for this condition has been a major goal of neurological research for many decades.

Normally, CSF is produced continuously by the ependymal cells in the brain's choroid plexus, and is then reabsorbed by the body's vascular system via arachnoid granulations which act as one-way pressure differential valves. Before reabsorption into the bloodstream, CSF flows through the narrow passages of the four ventricles, bathing the brain tissue and spinal cord. It functions in shielding the brain from shocks by keeping it buoyant, in delivering nutrients, and in removing waste from the area surrounding the brain. It also compensates for changes in intracranial blood volume by flowing between the cranium and spine.

Approximately 500 mL of CSF is produced and absorbed each day by a healthy individual, with only about 100-160 mL present in the ventricular system at one time. Thus, in a healthy individual the intracranial pressure is maintained at a steady level (approximately 16-24 mmHg, while the individual is sitting up) [5]. For individuals suffering from hydrocephalus, this steady level of CSF is no longer maintained by the body. Hydrocephalus may be present at birth (congenital) or may develop at a later stage of life (acquired), and thus can affect people of all ages. The condition can be classified as communicating, where CSF can still flow between the ventricles, or non-communicating, where CSF is blocked from flowing through one of the narrow passages connecting the ventricles. Aqueductal stenosis, a common cause for hydrocephalus, is of the latter type. Stroke, traumatic brain injury, infection, tumors, or complications from surgeries can also lead to other types of secondary hydrocephalus, such as hydrocephalus ex-vacuo and Normal Pressure Hydrocephalus (NPH), a condition affecting an estimated 375,000 older Americans [1].

Hydrocephalus affects various individuals in different ways, resulting in some difficulties in correctly diagnosing this condition. In infants, the most obvious symptom is a rapid increase in the circumference of the head due to the newly formed skull's ability to expand to accommodate the buildup of CSF. Infants may also show signs of vomiting, sleepiness, irritability, downward deviation of the eyes (also called "sun setting"), and seizures. Additional symptoms may be experienced by children and adults suffering from hydrocephalus, including severe headaches and cognition/memory loss. However, these symptoms are not exclusive to

hydrocephalus. Especially in the elderly, NPH is often misdiagnosed since the symptoms may be mistaken for the onset of other diseases affecting older individuals such as Alzheimer's disease, Parkinson's disease, and Creutzfeldt-Jakob disease [1].

Once diagnosed with hydrocephalus, it is imperative that a patient receive the proper treatment in a timely manner. When left untreated, progressive hydrocephalus may be fatal. NPH has symptoms that worsen if left untreated, especially in older individuals. Children and adults who are diagnosed early and are properly treated have a very high survival rate; and, especially when treatments are coupled with rehabilitative therapies, these individuals may go on to lead normal lives with few limitations [1].

1.2.2 Hydrocephalus: Current Procedures and Surgical Techniques for Treatment

The most common surgery performed to treat hydrocephalus is the insertion of a shunt into one of the brain's fluid-filled ventricular cavities. A shunt is a mechanical device that diverts excess fluid from the brain to another part of the body where it can more readily be absorbed into the blood stream. Typically the flow is diverted to the peritoneum (abdominal cavity), but sometimes to the right atrium of the heart, pleural (lung) cavity, or other areas (see Figure 1.1). A shunt often relies on 3 main components to accomplish this diversion: a ventricular catheter, implanted into the patient's brain; a differential pressure valve, which acts

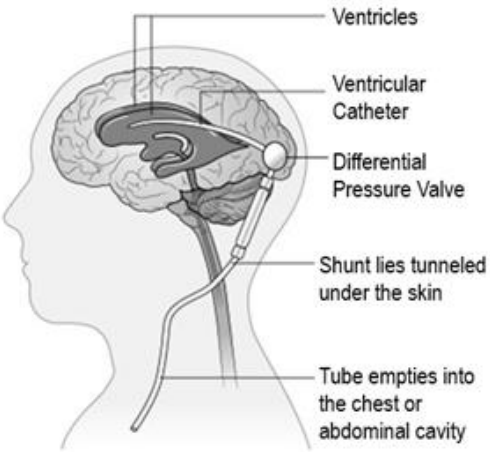

Figure 1.1 Diagram showing an implanted CSF shunt and indicating the location of the ventricular catheter within the brain.
(Image attributed to Cancer Research UK. Licensed under CC BY-SA 4.0 via Wikimedia Commons.)

as a regulatory mechanism for the flow; and a distal catheter, which drains the diverted CSF to the desired area of the patient's body.

Surgical techniques not requiring the implantation of any mechanical device are relevant for a smaller percentage of cases, but generally have high rates of success. These techniques still pose the same risks as other neurosurgical operations, including intracranial bleeding and infection, but avoid the complications associated with shunts: most importantly, the need for revisions due to device failure. Endoscopic surgery has been employed successfully on a smaller scale, though it requires neurosurgeons with highly specialized training. In neuroendoscopy, a surgeon utilizes an endoscope: a tube-like device which includes an integrated light source, to look inside a body cavity or organ. The endoscope is inserted through a small burr hole made in the skull, and then depending on the procedure, a probe may also be inserted through the working channel of the endoscope and used to fenestrate (or perforate) the membrane blocking the flow of CSF [6].

Endoscopic third ventriculostomy (ETV) is a surgical procedure aimed at creating a new communication (i.e. connection of flow) between the ventricular system and the subarachnoid space. This is achieved through fenestration of the third ventricle floor. ETV has been performed most successfully for cases of hydrocephalus in which the normal mechanism for CSF absorption still exists at the arachnoid granulations (for instance, cases caused by aqueductal stenosis, or compression of the aqueduct or fourth ventricle by tumors) [6]. Success of ETV is dependent on many factors, including the age of the patient and the type of hydrocephalus.

In cases of multiloculated (or multicompartmental) hydrocephalus, endoscopic fenestration may be performed in order to reduce the number and/or complexity of the shunts needed for successful treatment. This can be greatly advantageous since the placement of multiple ventricular catheters increases the probability of catheter malposition and thus, the need for surgical revision. Endoscopy can be a versatile tool used in various procedures to consolidate the number of catheters, including fenestration of the septum pellucidum and intraventricular septations, foraminoplasty, aqueductoplasty, and ETV [7].

Treatment for hydrocephalus must, of course, first begin with a correct diagnosis. As mentioned previously, this is often difficult to achieve. Correct diagnostic tools must be selected based on an individual's age, symptoms, and known/suspected abnormalities in the brain or spinal cord. A physician may use cranial imaging techniques after performing a clinical neurological evaluation, which often includes a spinal tap to measure CSF pressure. These techniques may include a combination of ultrasonography, CT, and MRI [1].

1.3 Background: Cerebrospinal Fluid Shunts

1.3.1 Complications and Causes for Shunt Failure

Though established as the standard procedure for most hydrocephalus treatments, the cerebral shunt system still has many inherent flaws. Complications arising after implantation are unfortunately common, requiring close monitoring and regular medical follow-ups of patients after the initial shunt placement. Complications requiring a subsequent surgery to remove or alter the shunt fall under two main categories: those arising from changes in the patient's condition and those caused by device malfunction. Both categories constitute a failure of the shunt system to perform its given task: maintaining a steady, healthy level of CSF in the patient's ventricular system. Although shunts serve as the default treatment for hydrocephalus, shunt failure rates are still alarmingly high. Well over 50 percent of pediatric shunts require revision over the course of their lifetime, most within the first or second year after the original surgical intervention [8-10].

Changes in a patient's condition during the course of hydrocephalus may result in underdrainage, overdrainage, infection due to faulty placement, or the need to adjust the shunt tube length. Overdraining can lead to ventricular collapse, during which blood vessels may be torn, causing the patient to experience severe headaches [1]. In a randomized study performed on 344 hydrocephalic children and published in 1998 [10], shunt failure was observed in 150 patients (43.6% of the test group) and was categorized by the cause of failure. Of those 150 cases, 108 (31.4%) were attributed to shunt obstruction, 28 (8.1%) to infection, 12 (3.5%) to overdrainage, and 2 (0.6%) to loculated ventricles. Post shunt implantation, 61% of the group were observed to be shunt failure-free after 1 year and 47% after 2 years. The median shunt failure-free duration for the group was 656 days, or just under 2 years.

Another study [11] performed a multivariate analysis on prospectively collected shunt failure data. The multivariate model allowed for an analysis of the effects of ventricular size, catheter location, catheter environment, and the cause of the hydrocephalus. Three-quarters of the model variability was accounted for by the ventricular catheter location and its environment, pointing to these as the most significant risk factors. Catheters placed in the occipital horn had a lower hazard ratio than those placed in the frontal horn. A lower hazard ratio was also observed when the ventricles were expanded, allowing the catheter to be completely surrounded by CSF. Therefore, catheter placement is a critical factor for shunt success.

1.3.2 Ventricular Catheters and Shunt Obstruction

This work focuses specifically on the ventricular catheter, a thin, flexible tube made of an extruded silicone (PDMS) based polymer. Most ventricular catheters feature an internal diameter of approximately 1.0 – 1.6 mm and are closed off at one end with a rounded tip. A set of small holes, generally each between 0.285 – 0.975 mm in diameter, near the catheter tip serve as inlets for CSF to enter the shunt on the ventricular end (see Figure 1.2). In many cases, these small holes often become occluded by an accumulation of cells or floating debris, or by fronds of choroid plexus, a CSF-producing structure within the ventricles [12-15]. At best, these obstructions can cause CSF to be drained less effectively, or at worst they can completely block CSF flow, leading to shunt failure.

As shown in the randomized study mentioned in the previous section [10], 31.4% (108 out of 344) of the total observed cases failed due to shunt obstruction, which equates to 72% (108 out of 150) of the total cases of shunt failure. Of those cases, one-third (36 out of 108) were due specifically to ventricular catheter obstruction. The study featured the use of 3 different valves in the implanted shunt systems. The shunt systems featuring the Orbis-Sigma valve by Cordis, a flow-limiting device, experienced the least number of failures due to ventricular catheter obstruction, but a higher number of valve failures. This may suggest that the action of the valve improved flow through the catheter perforations, but that the site of obstruction may have simply moved downstream toward the valve itself [16].

Catheter placement weighs heavily on the probability for an obstruction to occur, as the proximity of the catheter inlet holes to the choroid plexus is an important factor. Given that the average length of a catheter's inlet segment is

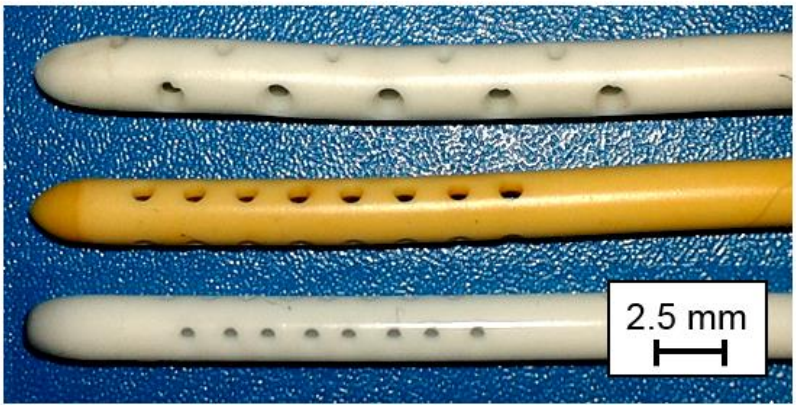

Figure 1.2 Photograph showing 3 different styles of catheter tips with varying designs of inlet hole configurations.

between 1.6 - 2 cm and that the average intraventricular distance available for catheter placement in the frontal horn is less than 1.6 cm [17], most catheters will likely be placed only a troublingly small distance away from the invasive fronds of the choroid plexus.

Surgical placement techniques have improved over the years, reflecting the increased accuracy of added technological intervention to assist the widely used freehand technique [18-21]. These methods all aim to assist the surgeon in placing the catheter in a favorable position such that it is surrounded by CSF and is not in contact with tissues, to the degree possible. In cases of slit-like ventricles, this becomes nearly impossible as the ventricles have very little fluid filled volume. When an obstruction is suspected, there are some methods, such as shunt taps, to test for patency and attempt to solve the issue. Although several methods of recanalization or cannulation of the catheter have been developed over the years [22-24], almost all cases encountering catheter obstruction require revision surgery [25].

1.4 Research Approach

Though ventricular catheter obstruction is a complex issue involving many factors, including catheter placement and individual patient CSF composition, one of the few factors that may be directly influenced by researchers aiming to improve shunt success rates is the catheter design. Modifications to design can change flow parameters in such a way as to prevent, or significantly reduce, the chance of obstruction-induced shunt failure. Catheter design is therefore the focus of this research. It is systematically broken down into its constituent parameters and examined for areas of possible improvement with regard to the fluid dynamics of the catheter.

A significant part of this work deals with modeling and characterizing the flow through a catheter within the ventricular space. Certain assumptions are made in order to allow for a practical computational model to be created, evaluated, and then modified for design exploration of the ventricular catheter. An experimental fluid imaging approach complements and aids in validating the computational models. In addition, by taking advantage of high-performance computing resources and an automated, iterative framework, the model is used as a basis for geometric optimization. These characterizations and fluid dynamic simulations will serve to inform future efforts of catheter design.

CHAPTER 2:
LITERATURE REVIEW

2.1 Overview

Prior to performing computational analyses or experimental tests on ventricular catheter design, it was critical to conduct a thorough review of the existing literature on the subject. Since the topic of this research is interdisciplinary, requiring knowledge from several fields including neurosurgery, fluid dynamics, and computational sciences, the literature was gathered from multiple databases. Most of the material on shunts, and more specifically ventricular catheters, was located by conducting key word searches in PubMed, a free online search engine provided by the United States National Library of Medicine. This database consolidates scientific publications in the fields of life sciences and biomedical applications, making it a powerful tool for such preliminary research.

Understanding the history of ventricular catheter design, within the context of shunt evolution, was an important first step in the literature review process. In examining the beginnings of shunt engineering, it was clear that the modern ventricular catheter of the 1950s and 60s was a great improvement over the iterations of previous decades. Advancements throughout the past 50 years in the fields of materials science and biomedical engineering have since improved these catheters even further, but several major challenges still exist. One of these challenges remains the high rate of catheter obstruction among patients. Though many innovations aimed at reducing obstruction rates have been attempted over the years, none have been proven clinically successful.

One of the suggested improvements to catheter design has been to modify the configuration of inlet holes at the tip of the catheter in order to influence the fluid dynamics of CSF flow through the catheter. More specifically, several computational studies have been performed to demonstrate the effect of changing catheter hole configurations on the distribution of inlet flow rates along the length of the perforated segment. Most current designs feature a configuration in which a majority of the flow is concentrated in the hole sets closest to the catheter outlet. This design potentially favors failure-inducing obstructions. Therefore, the goal of previous studies in this field has been to provide better flow uniformity among the holes, to statistically prevent such an occurrence. This work also focuses on this goal, this time through systematic parametric optimization.

2.2 Ventricular Catheter Development: Past, Present, and Future

Disclaimer

This chapter section contains material that has been published in the Journal of Neurosurgery, under the article title "Ventricular catheter development: past, present, and future" [26]. Authors are Sofy H. Weisenberg, Stephanie C. TerMaath, Chad E. Seaver, and James A. Killeffer.

Permission has been granted by the authors and the Journal of Neurosurgery to republish the article in this academic thesis. Images and figures have been removed from the article published here, so as not to infringe on any copyright restrictions. The article's formatting has been modified to reflect the formatting of the remainder of the thesis. References for the article are included at the end of the thesis, as part of the general references section, so reference numbers are not as they appear in the original article.

2.2.1 Introduction

The most common treatment for both congenital and acquired hydrocephalus is the placement of a CSF shunt that diverts excess CSF from the ventricles to a part of the body in which it can be readily absorbed. While effective, newly placed shunts require on average 2 to 4 revision surgeries within the first 10 years after implantation [27, 28]. A large percentage of these revisions occur within the 1st year after placement, and most [28] are required within the first 2 years [29-31]. Ventricular catheter (VC) obstruction is the cause of nearly one-third of shunt failures, making it the most common reason for revision surgery [9, 31, 32].

Reducing shunt failure rates remains a major goal of shunt development, and improving VC performance would constitute a major step in that direction. Although several reviews have addressed the historical development of the shunt system as a whole [33-38], none to date have focused specifically on the VC. The object of this paper is to highlight the evolution of VCs in order to inform modern efforts at improving their effectiveness and reliability.

2.2.2 Historical Overview of the Pre-Shunt Era

Following Joseph Lister's discoveries of the benefits of aseptic surgery in the 1860s [39], methods involving cannulation of the ventricles became feasible and were attempted with varying degrees of success. The first sterile ventricular

puncture and external ventricular drain (EVD) insertion was performed in 1881 by Carl Wernicke [40]. External drainage via catheter-like devices, including horsehair, silk, and catgut wicks, became quite popular during the late 19th century [41]. However, in response to the risks posed by open drainage, attempts were made at the beginning of the 20th century to introduce mechanisms for internal CSF diversion [42]. Rerouting CSF from the ventricles to the subdural space was first accomplished in 1893 by Polish-Austrian surgeon Jan Mikulicz-Radecki, who inserted a mass of glass wool in the shape of a nail into the ventricles of a child [33, 43]. The child not only survived the procedure, but progression of the hydrocephalus in this case was effectively stopped. In the later part of the 1890s, gold tubes [44] and bundled strands of catgut [45] were also utilized for such "ventriculo-subdural" shunts. In 1903, Nicholas Senn performed the first recorded surgery using a perforated rubber tube, a crude predecessor of the modern VC, for subcutaneous drainage of CSF [42].

Most of these attempts ended badly, however, as patients developed fatal infections in addition to the already present mechanical obstruction. As early as 1899, Adolf Dehler reported failure of an implanted gold tube due to "stoppage" [43]. These obstacles were not easily addressed by the medicine of the times, and a lack of effective antibiotics made it difficult to combat infections once they were identified. Nevertheless, surgeons practicing between 1908 and 1926 pursued many variations on this type of ventricular drainage including the use of glass tubes [46], split-ended silver tubes sewn to the pericranium [47], and even strips of omentum [48] (peritoneal tissue). In 1917 the neurological surgeon William Sharpe reported some success with the use of linen threads. Out of the 41 patients in Sharpe's clinical study, 28 survived the procedure, and 22 of those showed marked improvement [49].

Transplanted human or calf blood vessels were also implanted in various experiments and routed to the superior sagittal sinus, the jugular vein, or the common facial veins [43]. In this case, the valves in the veins were used to prevent backflow and direct the CSF out of the ventricles. These early decades of the 20th century also saw many other innovations in the treatment of hydrocephalus, including the first descriptions of Kocher's point and Frazier's point, the optimal cranial sites for catheter insertion that are still used today [50]. Although these early attempts created the foundation for the modern VC, the mid-20th century would see the first truly successful breakthroughs in its implementation.

2.2.3 Beginnings of Modern VC Development (1950-1980)

Arne Torkildsen developed the most notable precursor to the modern internalized shunt. The Torkildsen shunt furthered the widespread use of implanted catheters during the 1940s and 1950s and, until the introduction of ventriculoatrial and ventriculoperitoneal shunts, was the most widely used means of CSF diversion. Introduced in 1939, it consisted of a rubber catheter used to cannulate the lateral ventricle and divert CSF to the cisterna magna in cases of noncommunicating hydrocephalus [51]. Because the Torkildsen shunt used a catheter to simply bridge 2 CSF-filled cavities, one favorable outcome was a very low incidence of catheter obstruction, which would come to be a serious issue in more complex shunt systems [13, 52, 53].

The advent of the modern, fully internalized shunt system is generally credited to the innovations of Frank Nulsen and Eugene Spitz. In their landmark 1951 paper, they described the first successful attempt to treat hydrocephalus by means of a ventriculojugular shunt [54]. Although this paper is commonly credited with introducing the first 1-way flow-regulating device in a ventriculojugular shunt, it also describes the use of a specific 12-Fr soft rubber catheter inserted into the ventricle.

In the meantime, the search for improved biomaterials continued. Franc D. Ingraham, a pioneer in pediatric neurosurgery, published a report in 1947 on the use of polyethylene as a new synthetic plastic for use in neurosurgery, suggesting that it could safely implanted into the tissues of the ventricular system [55]. Until this period, rubber tubing had been the standard material used in the Torkildsen and in the first Nulsen-Spitz shunt. Ingraham's findings led to the choice of polyethylene as the material for a new generation of VCs. Polyethylene, however, ultimately proved to be an unsatisfactory shunt material due to complications on the distal end, prompting a search for a better polymer [56]. This search led to polydimethylsiloxane (PDMS), or silicone rubber. Originally investigated as insulation material for electric motors and generators, PDMS was studied as a potential biomaterial throughout the 1940s due to its elasticity, thermal stability, and bio-inertness [57].

In 1948, the first successful replacement of a male urethra by a narrow silicone catheter was accomplished [58], which led to the consideration of other clinical applications for silicone catheters. In 1957, Robert Pudenz reported on the successful use of a ventriculoatrial shunt made completely of silicone rubber [59]. The first silicone ventriculoperitoneal shunt was implanted in 1958 by Richard Ames, and 9 years later he reported promising results after performing 120 additional procedures using silicone tubing [56]. This period marked an increase in the popularity of silicones, in part due to their prominent use in the Apollo space

program, and there was a significant transition to the almost exclusive use of medical-grade silicone (marketed as Silastic by the Dow-Corning Corporation) tubing in shunts, and specifically in VCs.

With this successful shift in materials, engineers began to focus on how to solve the other problems inherent in shunts, particularly the prevention of VC obstruction. In his 1969 report [13] on the nature of VC hole occlusion, Salomon Hakim identified the main cause of obstruction as the invasion of choroid plexus via the catheter holes. Hakim, as well as other neurosurgeons, attempted to remedy this problem by modifying VC architecture. He introduced the “shepherd crook” or J-shaped catheter, the tip of which was curved, with holes on the inside of the curve so as to distance them from invasive fronds of choroid plexus. Despite some early recorded success with this design, the experience with this particular catheter was disappointing overall, as elongated filaments of choroid plexus were still able to reach the catheter tip, obstructing the orifices [13, 28].

Another design was the Portnoy flanged catheter, introduced in 1971 [60]. Although seriously flawed, this design has seen relatively prolonged use in the neurosurgical community. The original design included several soft silicone rubber “umbrella” flanges positioned between the catheter holes; these were intended to protect the holes from brain parenchyma during insertion and from invasion of choroid plexus in the ventricles [61]. The flanges folded back over the holes during insertion and opened once the catheter tip was inside the ventricle. Although there was some early clinical evidence that this design reduced catheter occlusion, and therefore the need for shunt revision [61], this initial conclusion was later reexamined in a report that found evidence of a higher risk of proximal occlusion with long-term use of the flanged design. Moreover, the presence of the flanges was detrimental to those patients who did require revision, in that the flanges made catheter removal extremely dangerous by creating a risk of hemorrhage and permanent damage to surrounding brain tissue.

2.2.4 Maturation of the Modern VC (1980-2005)

Root cause investigations of ventricular catheter failures during the 1980s offered new insights into the mechanisms of shunt failure, particularly occlusion, and new countermeasures to circumvent problems were devised. In 1981 Go, et al. [29] histologically examined explanted catheters and identified dead cell-related obstructions that developed within 1 month of implant and choroid plexus invasion occurring within 3-6 months. In 1982, Sekhar, et al. [62] identified adsorbed tissue types including connective, inflammatory, granulomatous, glial, and choroid plexus as sources of occlusion. Characterization of obstructions and obstructed flow

through VCs were also studied via mathematical models [63] and shunt reservoir taps [64], and a number of investigations of materials and methods to circumvent this problem were subsequently undertaken. A 1982 design included a floating catheter that included an air cell integrated into the catheter. This was intended to provide some distance between the ventricle walls and the center of the ventricle in order to avoid significant choroid plexus contact and invasion [65]. Other patented approaches similarly attempted to protect the catheter holes from occlusion [66, 67].

Several modifications in material were also experimentally evaluated during this period. One of the most notable investigations included the testing of what eventually developed into Codman's Bactiseal antimicrobial catheter. In 1981, Bayston and Milner [68] evaluated the addition of various antibiotics to silicone catheters as a means of reducing of obstructions due to microorganism colonization, which was believed to develop from skin bacteria (e.g., *Staphylococcus albus*) proximal to catheter incision sites. This study evaluated various antibiotics introduced at 4 different process steps of silicone vulcanization. Other patents [69, 70] issued in the 1980s used meshlike porous materials, formed by processes such as ion beam sputter-etching [69], to promote a more favorable biological response. A further investigation presented by Medow [71] also suggested that such a catheter material, which is permeable to most components of CSF, but not to prokaryotic or eukaryotic cells, could help prevent catheter obstruction.

In contrast to the silicone (PDMS) catheters that were widely used during the 1980s, Wong, et al. [72], in a 1991 publication, evaluated construction of catheters from pHEMA (2-hydroxyethyl methacrylate), a semi-wettable polymer that is essentially a gel-like material in water. pHEMA materials, which began to be studied for biocompatibility in the 1960s [73], reportedly hinder protein adsorption and cell binding by offering a strongly hydrophilic surface composition. Although Wong's study showed intriguing promise for pHEMA construction, the device design used in the study consisted of a subdural shunt configuration, in which fibrous subdural catheter encapsulation developed. Consequently, the evaluation was inconclusive and the possible benefits of pHEMA as an anti-fouling catheter material were obscured. In 1992, Gower, et al. [74] evaluated expanded polytetrafluoroethylene (e-PTFE) as another alternative to silicone. Commonly known as Gore-Tex, this material is currently used as a long-term implant in vocal cord treatments, arterial grafts, orthopedic joint implants, and facial plastic surgery because it is associated with minimal adverse tissue reactions. However, Gower found that, although e-PTFE is successful in other applications and is safe as a

cerebral implant, the porosity of the material, which is on the order of only 5 µm, unfortunately permitted tissue ingrowth and catheter obstruction.

An additional material modification included a VC coated with polyvinylpyrrolidone (PVP) for surface functionalization. Introduced in 1995 by Medtronic under the brand name BioGlide, PVP is a hydrophilic substance that can covalently bond to the surface of silicone as a hydrogel, providing a “water jacket” by virtue of water absorption and thereby creating a slippery surface. A 2004 study showed that such functionalization indeed provides some resistance to bacterial colonization [75]. However, the BioGlide’s surface was so slippery that the catheter lumen would sometimes slip out of the connectors attaching it to the valve in the shunt system, a problem that caused it to be removed from the market in 2010 [15, 76].

At the turn of the millennium, new advancements for VCs were introduced by commercial conglomerates, including Johnson & Johnson and Medtronic. Codman (J&J) investigated the antimicrobial-impregnated lumens previously researched by Bayston and Milner, and the resulting catheter, branded Bactiseal, was approved by the FDA in 2001. The catheter featured impregnation of 2 anti-microbials, Rifampicin and Clindamycin HCL, into the silicone matrix [77]. A few years later in 2008, Medtronic introduced extracted silicone catheters, having unpolymerized oligomers removed for treatment in silicone sensitive patients [78].

On the design front, a wide variety of proposed catheter geometries were patented during this time, though few were actually adapted for clinical use. Lin, et al. published a landmark study [79] in 2003 that demonstrated, through computational fluid dynamics and experimental validation, that the commonly used 12- to 32-hole perforation patterns in VCs make them highly prone to the type of obstructions that cause shunt failure. The study showed that only the most proximal hole sets (those furthest from the catheter tip) actually experience significant flow rates (50-75% of the entire flow volume) during CSF drainage, while the distal holes (those nearest to the tip) have substantially lower flow rates in comparison. The study suggested that a more uniform flow distribution among the catheter holes could help prevent shunt failure by decreasing the probability of occlusion of the proximal hole sets and that, in the case of a distal hole occlusion, at least some of the functionality of the catheter would be preserved. The resulting improvement was later approved by the FDA and introduced to the market in 2007 as Medtronic’s Rivulet catheter. This device utilizes a configuration 4 parallel rows comprising holes of decreasing size, with the distal hole set being the largest. The uniformity of flow distribution of this design was verified again more recently in computational simulations by Galarza, et al. [80, 81]

2.2.5 Contemporary Ventricular Catheters (2005-2015)

The last decade of shunt development has seen a renewed interest in VC design, as well as the incorporation of new materials and coatings. Today, most VCs are made of silicone polymer tubing and are available in straight configurations, which may be cut to the appropriate length intraoperatively, or angled configurations, which have a set length. Inner diameters of the tubing range between 1.0 mm and 1.6 mm and outer diameters between 2.1 mm and 3.2 mm [35]. Holes are usually arranged in 3 or 4 rows, equally spaced around the catheter diameter in the 1.0-1.5 cm nearest the catheter tip, with rows arranged either in parallel or staggered configurations, generally with 4-8 holes in each row. Holes within a row may be the same size, typically measuring between 0.25mm and 0.5 mm at the outer catheter surface, or may change along the length of the row. Many holes feature a conical shape, slightly tapering toward the inner surface. Hole number, size, shape, and spacing vary among the different manufacturers [35, 80, 81].

Material Considerations

Limiting the adhesion of proteins and cells that can cause catheter obstruction or infection has been a primary focus of VC research. Surprisingly, it has been found that high CSF protein concentrations may actually inhibit bacterial adhesion due to rendering the generally hydrophobic silicone more hydrophilic [82]. Protein adsorption alone has not been shown to cause accumulations in great enough amounts to generate occlusions, and the thin albumin film which most often forms may actually serve to improve the biocompatibility of the catheter [83]. A 2010 report showing that astrocyte adhesion was positively correlated to fluid flow through VCs [84] may explain the favorable initial results of experiments evaluating the cell growth characteristics of electrospun polyurethane catheters, which are microporous in nature and would have inherently lower flowrates than most catheters [85]. Another approach to reducing obstruction is to limit contact of the VC holes with brain tissues during ventricular puncture, so as to avoid the ingestion of parenchymal cells by the catheter. A peel-away sheath technique has been implemented by some neurosurgeons to protect the VC holes from brain debris during insertion. However, a randomized study, performed in 2012 by Kehler, et al. [86] in 177 patients with ventriculo-peritoneal shunts, showed no statistically significant difference in the number of obstructions among patients in which a peel-away sheath insertion technique was used.

A focus on catheter surface properties and coatings has also led to recent advancements. In 2007, a National Institutes of Health-sponsored workshop on the priorities for hydrocephalus research indicated the need for more in-depth research into the possible benefits of antibiotic-impregnated catheters [87]. In vitro and preclinical studies have shown that various forms of polyethylene glycol, a non-degradable hydrophilic polymer, may reduce protein adsorption and macrophage and astrocyte attachment when used as a catheter coating [88, 89]. The addition of silver-nanoparticles to such coated catheters also produced a notable drop in catheter-related infections [62]. Another possible improvement that has been suggested is diamond-like carbon coatings that are produced by plasma-assisted chemical vapor deposition [90]. By acting as an effective ion diffusion barrier, such coatings can protect the patient from ions released from the catheter while at the same time protecting the catheter from the harsh biological environment. The incorporation of other surface-modifying coatings and additives, including surfaces that mimic native extracellular matrix or endothelial cell layers, incorporation of pharmaceuticals, bioactive agents, self-locating fluoro-oligomeric additives, and antithrombogeneic agents, show promise for further investigation [15].

Design Considerations

Along with material and surface improvements, inlet hole design may also be key to improved VC functionality. It has recently been shown that macrophage and astrocyte adhesion to catheters is greater in flowing fluid conditions than in static fluid conditions, making flow rate through each of the holes an important parameter to consider [84]. In addition to flow rate, the number and size of holes may also affect the rate of cell adhesion. Decreasing the number of inlet holes or the hole diameters causes fluid wall shear stress at the hole surface to increase, and increased shear stress has been linked to increases in cell adhesion (although at the other extreme, very low shear stress may increase cell adhesion as well) [91]. Further investigations into the influence of these factors on obstructions resulting from cell adhesion and inflammatory response are necessary, but changing hole configurations may be an inexpensive way to make meaningful advancements in VC design. The fabrication of these inlet hole configurations is also of interest since the techniques currently used sometimes result in the creation of inherently rough hole surfaces. Improving these techniques or adding secondary manufacturing steps to smoothen the hole surfaces, after hole punching processes for example, may help to reduce cell adhesion to these surfaces as well as decrease the incidence of thrombogenesis at the inlet holes [15, 91].

Optimizing hole design and configurations has also been investigated as a means to reduce catheter obstruction. Along with the computational fluid simulations done by Galarza, et al. [80, 81] on different catheter configurations, an experimental study published in 2010 by Thomale, et al. [92] examined VCs with substantially fewer perforations. These experimental catheters were designed with a total number of either 4 or six 6 (as opposed to the more common 12 - 32 holes) located closer to the catheter tip, thereby reducing the length of the perforated catheter segment. The study was conducted in response to the hypothesis that proximal holes in the catheter may, on occasion, be positioned outside the ventricle, thereby increasing the risk of obstruction, especially in cases of slit-like ventricles. It was demonstrated clinically that catheters with fewer perforation holes, when correctly positioned within the ventricles, are sufficient to maintain shunt function and flow capacities. This finding confirms an earlier study [93], which argued that the same pressure-flow correlations may be observed in catheters bearing as few as 2 holes as well as those with the standard 32 holes. Both studies suggest that designs utilizing more than 2 holes do not necessarily correlate to improved drainage through the catheter.

Methods of response to VC obstruction have also been improved in recent years. Invasive techniques of catheter recanalization, which require surgical exposure of the catheter, have been investigated over the past 2 decades. These techniques include pulsed laser energy delivered via a flexible optical fiber [24], ultrasound waves transmitted over a fine wire [94], and percutaneous endoscopic recanalization via electrocautery [50]. However, focus has more recently turned to finding non-invasive treatments. When an occlusion is suspected, a new non-invasive imaging method combining pulsed laser light and ultrasound techniques has been proposed to allow surgeons to view the occluded catheter through the skull [95]. Once an occlusion has been identified, another recent study reports that transcutaneous vibration in the 50-60 Hz range, applied in short intervals, has been shown to maintain in vitro catheter performance and clear catheters that were completely occluded [22]. In addition, the novel inclusion of MEMS (Micro Electro-Mechanical Systems) in the form of magnetic microactuators, has been studied as another alternative to clear blocked holes. These microactuators may prove advantageous, as they can be controlled noninvasively and require no integrated circuits or power sources [23].

Some of the recently patented design improvements to VCs have shown more of this novel thinking. One design features a rounded transparent tip which allows for the concurrent insertion of an endoscope through the catheter during surgery [96]. This can provide continuous visualization for intraoperative navigation of the catheter tip while in the fluid-filled ventricle. The tip's round shape

is specifically designed to minimize contact with tissues that could potentially obstruct the view of the implant site. Another configuration features a biocompatible housing made up of several components. This housing may be fitted onto a standard catheter to specifically combat the potential for occlusions, particularly those initiated by an inflammatory response [97].

2.2.6 Future Directions

Overall, shunt development could benefit from a more holistic approach to VC engineering, taking into consideration the component's biocompatibility, surface properties, surroundings, lifespan, and mechano-fluid dynamics. Evaluating the effectiveness of antimicrobial impregnated catheters as well as other infection prevention mechanisms should be a priority as these technologies continue to mature. Alongside material advancements, design optimization through systematic fluid flow testing of catheter hole configurations, for example, may also prove beneficial and remains a largely underexplored area for improvement.

Another particular emphasis in several recent publications [11, 98, 99] has been on the role of VC placement in overall shunt success, especially in patients with smaller or abnormal ventricular anatomy. Achieving optimal positioning with the VC completely surrounded by CSF remains challenging. Radiopaque indicators, typically utilizing barium sulfate or tantalum and incorporated into the VC polymer, are included in most commercially available catheters today and aid in verifying VC positioning. Still, the push for more accurate VC placement processes has certainly had an effect on surgical technology [18-21] and may have future effects on VC design.

2.2.7 Conclusion

Advances in the fields of biomaterials and biomedical engineering have made significant contributions to the ability of this implanted device to allow many patients to lead relatively normal lives. Unfortunately, VC development has been disappointingly slow, and this component remains plagued by both mechanical and bio-adaptability issues. Additionally, the environment into which VCs are implanted is unique and complex, making it difficult to attain a comprehensive understanding of their in vivo functionality. Detailed imaging of operational VCs in action is not available, and in vitro experiments cannot accurately mimic what a VC would encounter over the course of its implanted lifetime. The solution to catheter obstruction continues to elude engineers and neurosurgeons alike, due to the many variables that influence obstruction rates. These include location of the

catheter tip, varying CSF composition and flow characteristics among patients, and differences in catheter geometry among the many competing commercial designs available today [15]. By gaining an improved understanding of each of these mechanisms and their interactive effects, the scientific community can optimize VC design to resist or prevent obstructions, thereby reducing emergency interventions, revision surgeries, and their associated risks to the patient.

2.3 Existing Fluid Dynamics Studies of Ventricular Catheters

The optimization of ventricular catheter design first requires a thorough understanding of CSF flow through the perforated catheter tip. Since observing the actual flow through implanted catheters is very difficult and costly, even with today's advanced medical imaging capabilities, the simulated fluid flow requires observation through ex vivo experiments and computational models. The thesis work following this literature review will be heavily based on the latter form of simulation, employing computational fluid dynamics (CFD) principles to model both the 2D and 3D cases of catheter flow. Several previous CFD studies on flow through ventricular catheters, Lin et al. [79] and Galarza et al. [80, 81, 100], have provided a significant basis for the current study and will be discussed here in more detail, though they are mentioned in the previous section as well. These studies are important as they have formed a basis for much of the current work of this thesis and have allowed for validation and comparison.

2.3.1 Lin, et al. – 2D Computational and Experimental Study

The first study specifically focusing on the flawed fluid dynamics of ventricular catheters was published in 2003 by Lin et al. [79]. The study featured a 2-dimensional (2D) CFD analysis on a standard catheter model featuring an inner diameter of 1.2 mm and 8 inlet holes per row, equally spaced and with equal diameters. It was concluded that most of the CSF mass flow enters the catheter via the most proximal holes (those furthest from the catheter tip), with 58% entering through the first most proximal set of holes and over 80% entering through the first and second most proximal sets combined. The authors validated their results with 2D water table experiments and a 3D water and ink experiment using a commercial catheter. Occluded ventricular catheters were also systematically collected from shunt revision surgeries during a 6-month period, and the majority of occlusions were indeed observed to occur at the proximal sets of holes.

These observations led the authors to conclude that blockages are more likely to occur at the proximal holes where they effectively block any flow entering

from the more distal holes, thereby rendering the catheter unusable. Their proposed solution was to use varying hole dimensions and hole spacing to generate a more uniform mass flow rate distribution across the entire catheter tip, with the assumption that this will allow for a more equal probability of occlusion at each of the hole sites. If a more distal hole were blocked, the proximal holes could still function and so the chances for complete shunt failure would be reduced.

2.3.2 Galarza, et al. – 3D Computational Study of 5 Existing Designs

Influenced by the landmark study by Lin, et al., another group more recently revisited the problem of flawed fluid dynamics in ventricular catheters in 2013. Galarza et al. [81] developed 3D CFD models of 5 commercially available catheter designs. Their model used a 60 cc rigid cylinder to simulate the hydrocephalic ventricle. The 3D catheter models were generated using the Salome v6.6 software package, and then imported to an OpenFOAM CFD numeric solver which utilizes a finite volume method. The s*nappyHexMesh* utility was used to form the 3D mesh, and the *icoFoam* solver was used for the computations. Non-slip and non-penetration conditions were applied to the wall boundaries. For the inlet, flow was set to a constant 100 cc/day with a zero-gradient condition on pressure, and for the outlet, the pressure differential was set to 15 cm H_20 with a zero-gradient condition on velocity.

To obtain the flow rates for the 3D model, the catheters were analyzed by observing segments of equal length in the inlet hole section. Each segment contained the same number of inlet holes. Their conclusions were similar to those of Lin et al., showing the same uneven flow distributions in catheters with both intercalated and strictly parallel hole row arrangements, with the exception of the “Rivulet” catheter style which showed relatively uniform flow rates with a maximum in the medial hole sets. This design was developed to increase flow rate distribution uniformity between the inlet holes, and was indeed shown to be superior in this ability compared to the other designs analyzed. In all designs, higher flow velocities were observed at the most proximal holes, as well as elevated wall shear stress numbers which can increase cell adhesion [101] and impact the flow at each hole.

2.3.3 Galarza, et al. – Suggestions for New Catheter Designs

Galarza, et al. followed this paper with another 3D CFD study in 2014 [80] in which they proposed a series of 5 prototype catheter tips to improve upon the commercial designs analyzed in their previous paper. The same basic CFD model

was utilized for this study as well, only requiring modifications to the design of the catheters. Since the “Rivulet” design had previously shown the most uniform flow rate distribution, all of the prototypes utilized the Rivulet’s strictly parallel hole configuration. Some of the prototype configurations double the number of hole rows in the distal hole sets while still maintaining the parallel alignment. In this way, they were able to obtain relatively homogenous flow patterns, as those observed in the Rivulet design, but without necessarily changing the hole diameters, which previously required the use of very small holes. Other designs featured an increased degree of hole tapering at the proximal hole sets.

2.3.4 Galarza, et al. – Parametric Study of Ventricular Catheters

The third and most recently published paper in this series by Galarza, et al. [100] is a parametric study of ventricular catheters, with similar goals to that of the following thesis work. The authors expanded their CFD model to 12 new catheter prototypes, all featuring 2.5 mm outer diameter, 1.5 mm inner diameter, and conical holes in which the outer diameters remained constant but internal diameters were subject to change. As in their previous work with new designs, some of the catheters featured segments with different numbers of holes, so that the strictly parallel configuration was not maintained. They accounted for this in their flow rate calculations with a formula to normalize flow rates to the total inlet area in each segment. The study also featured ink and water tests to validate 3 of the designs and show that the hole with most prominent flow could be shifted depending on the prototype design selected. The study concluded with a summary of 5 design principles:

1. Flow rate distribution is strongly influenced by the intersegment distances. These distances should be greater than 1 mm to maintain the catheter’s structural integrity.
2. A hole distribution featuring decreasing inter-segment distances, as one moves away from the tip, contributes to a more uniform flow rate pattern.
3. The actual number of holes in the catheter’s perforated segment does not significantly influence the flow rate pattern.
4. Fewer segments over a given perforated area contributes to a more uniform flow rate pattern, provided that the inlet areas follow a set mathematical formula (presented in the paper).
5. Rotating the inlet segments relative to each other around the axis of the catheter does not significantly influence the flow rate pattern. Also, the same is true of adding a patent hole at the tip end of the catheter.

2.3.5 How is this thesis innovative?

As can be seen by the previous studies described in this section, this thesis is not the first to explore the subject of changing ventricular catheter design based on improvements to the catheter's fluid performance. The previous studies developed both 2D and 3D CFD models to simulate the flow through a catheter, and 2 of the studies also featured some validation bench testing. The conclusions from these studies provided useful insight into the complexity of the problem and gave evidence that pursuing improvements in the catheter's fluid performance could reduce failure rates.

Increasing the catheter's inlet flow distribution uniformity was suggested as the most readily identifiable improvement, so it is also the goal of the current research. However, whereas previous studies tested only a few prototype designs, the work in this thesis will test thousands of designs in a systematic way in order to optimize the catheter's flow distribution. In such a way, this work will be a strong basis for future catheter design optimizations and will inform the efforts of future design engineers by creating an automated, iterative design exploration framework for investigating more complex optimization objectives.

2.4 Physics of Shunt Flow

2.4.1 CSF Flow Characteristics In-Vivo

The hydrodynamics of cerebrospinal fluid (CSF) within the human body are extremely complex. They have been studied for many years [102-105], with varying degrees of success in understanding the many aspects influencing the flow rates, direction of flow, and interaction with other fluid systems in the body. Adding pathophysiological conditions such as hydrocephalus to the analysis makes matters even more complicated as such conditions may affect the production, circulation, and absorption of CSF in-vivo [106, 107]. Generally, in a healthy individual, CSF flows from the ventricles, through the various aqueducts into the subarachnoid spaces, and finally to its sites of absorption at the arachnoid granulations or villi. Three-dimensional CFD modeling has been attempted to simulate CSF flow within the ventricular system, and it was found that velocity is highest during passage through the aqueduct of Sylvius [108].

The pulsatile nature of CSF flow is related to the cardiac cycle and blood flow. CSF is generally produced at a relatively constant rate of 0.35 mL/min [109]. Production is itself due to arterial pressure and both active and passive transport in the choroid plexuses and the brain tissue. Since the volume of the cranium is

fixed, the brain and its surrounding fluids have a finite combined volume. Due to expansion of the cerebral vasculature during each cardiac cycle, in which the brain receives approximately 20% of the cardiac output, the other fluids (including CSF) are compressed. This creates a “pulse” in CSF flow, forcing fluid out of the ventricular system and cerebral subarachnoid space into the more compliant spinal sub-arachnoid space [107]. This pulsatile flow can be seen through cine-MRI imaging techniques [110, 111].

2.4.2 Understanding Shunt Flow Rates

In order to characterize shunt hydrodynamics, basic understanding of the physics of CSF flow in-vivo is required, as well as an understanding of the influence of hydrocephalus and elevated intracranial pressure on this flow. In addition, the resistance provided by the shunt system’s tubing [112] and valves must be taken into account as these can greatly affect the achieved flow rates for a given device. It has been shown that CSF flow in most shunts is not governed by a constant flow rate [109, 113]. In a study utilizing a Doppler flowmeter to monitor “bubble-marked” in-shunt flow rates [113], it was shown that flow can fluctuate between 0.01 mL/min to 1.93 mL/min based on the individual’s supine position at an given point throughout the day. Changes in posture and head elevation can change flow rates by as much as 0.04 mL/min, and respiratory events, such as coughing, can have significant effects as well.

The effects of gravity and induced pressure elevations, such as coughing, make it difficult to estimate pressure requirements for shunt systems which must remain effective under all circumstances. The addition of a regulating differential-pressure valve attempts to reduce the effects of these fluctuations in pressure, as does the addition of anti-siphon devices that are meant to counteract the influence of gravity on shunt hydrodynamics and reduce overdrainage. Most valves on the market today are normally closed and open only at a certain threshold of intracranial pressure. Most manufacturers provide bench test data in their catalogs showing flow rates for given differential pressure settings.

However, these characterizations usually do not include in-vivo measurements of shunt flow rates – of particular interest would be the instantaneous flow rates associated with a “valve opening” event. It has been hypothesized that such events, after periods of static CSF containment in the ventricles, are potentially responsible for catheter occlusion. It has been argued in one publication [109], that valveless shunts that try to maintain a physiological flow rate of 0.35 mL/min would therefore stand a better chance of resisting occlusions by allowing a continuously slow and steady flow of CSF out of the ventricles.

CHAPTER 3:
MATERIALS AND METHODS

3.1 Overview

The computational modelling, simulation, characterization, and optimization of ventricular catheters was the primary focus of this research. These tasks were accomplished by creating computational fluid dynamics (CFD) models to simulate catheter flow, and subsequently by using these models as a basis for optimization in a high-performance computing setting. Initially, a two-dimensional (2D) model was simulated in order to gain an understanding of the basic properties and patterns involved in catheter flow. Once this model was mature, it served as a basis for a more realistic three-dimensional (3D) quarter model. Both the 2D and 3D models were fully parametrized and so allowed for geometric exploration of the catheter's design. All fluid modeling and simulation was accomplished using the open-source CFD software package, OpenFOAM®.

As it provided more realistic results, the 3D model was chosen as a basis for sensitivity studies and optimization. The CFD simulations were coupled to an iterative parametric analysis framework, DAKOTA®. This framework provided the necessary algorithms to systematically sample the parameter space of the catheter's geometric variables, and ultimately to perform optimization studies. The computational portion of the research required knowledge of CFD, scripting languages, including C++ and Python, and basic concepts in parallel computing.

Simultaneous experimental testing both informed model development and provided validation data for the computational work. Both qualitative and quantitative experiments were performed via in-vitro bench testing setups. Visual experiments with India ink and water allowed for initial qualitative pattern analysis, and a more advanced fluid imaging technique, positron emission particle tracking (PEPT), was used to gather quantitative experimental flow data. Both the computational and experimental work provided substantial insight toward a better understanding of the complexity of CSF shunt fluid dynamics and the reasons for frequent cases of obstruction.

3.1.1 Computational Resources

Much of the CFD modeling and some of the preliminary optimization were executed on a single Dell Precision T1650 workstation at the Department of Mechanical, Aerospace, and Biomedical Engineering on the University of

Tennessee, Knoxville campus. This workstation features 3.40 GHz Intel Xeon processor with 4 cores (hyper-threading enabled), and 16 GB of RAM. For the later stages of the study, a high-performance computing cluster system was utilized. The supercomputer “Darter”, located at the National Institute for Computational Research at Oak Ridge National Laboratory in Oak Ridge, Tennessee, facilitates computationally intensive research at the University of Tennessee, Knoxville and collaborating institutions. Darter is a Cray XC30 system with an Aries interconnect and a Lustre storage system. It has 11,584 physical compute cores and boasts a peak performance of 240.9 Tflops, or 10^{12} floating point operations per second. By running the simulations in parallel over many cores at once, execution time was significantly reduced for the larger-scale simulation runs.

Since the computational software used in the study is largely script-based and most effectively controlled by commands executed in a command terminal, it was determined that it would be beneficial to install a lightweight, programmer-friendly operating system (OS) on the single workstation. Ubuntu, one of the most popular free distributions of Linux, was selected as a favorable operating system since most open-source software (including OpenFOAM, and DAKOTA, which are discussed later in this chapter) are supported on this platform. In order to run a Linux OS on a workstation with a Windows OS already installed, a third-party hypervisor software Oracle VM VirtualBox (Version 4.3.16, Oracle Corporation) was used to create a “virtual machine”. This allowed a certain portion of the workstation’s processing capabilities and memory to be allocated to running an instance of Linux “on top” of the existing Windows OS. Ubuntu 64-bit (Version 14.04) was installed, and all computational analyses were subsequently run on this “virtual machine”. Using a Linux OS also facilitated the transition to high-performance cluster computing, in which most user interaction is strictly limited to a command terminal interface.

3.1.2 Experimental Resources

The validation experiments for this research work were conducted at the University of Tennessee, Knoxville campus. Commercial ventricular catheters were used for initial qualitative flow testing. For the quantitative experiments, a scaled-up version of a sample catheter was machined out of clear plastic (PETG) tubing. The experimental chambers were also made from plastic and required minimal machining. All machining was done in-house at the University of Tennessee, Knoxville.

For the quantitative experiments, imaging techniques were employed that required the collaboration of several fellow researchers familiar with these

techniques. The nuclear imaging technique of positron emission particle tracking (PEPT) was performed at the Science and Engineering Research Facility on the University of Tennessee, Knoxville campus. Access to imaging equipment was generously provided by the collaborating research group, and the imaging itself was performed by researchers certified to work with radioactive materials. The author of this thesis contributed only to the pre- and post-processing stages of these experiments, and in the comparison of experimental results to the relevant computational simulations.

3.2 Creating the CFD Model

3.2.1 CFD Software: OpenFOAM®

The main purpose of the CFD model in this study was to serve as a parametric template for running the numerous HPC studies. Because of the large number of simulations required, a model that minimized computational requirements while still capturing the necessary physical behavior was developed. The computational resources required to run the software was a critical component, as an instance of the software would need to be run for each separate simulation. Therefore, both the geometric modeling technique and the CFD software were selected with this criterion in mind.

The free, open-source software Open Source Field Operation And Manipulation (OpenFOAM®, Version 2.3.1, OpenCFD Ltd.) was selected. It includes utilities for building the computational domain and mesh, numerically computing the flow fields, and extracting relevant post-analysis data. OpenFOAM was also chosen because it can be controlled completely via user-written scripts and, therefore, lends itself well to design exploration and automated execution in an HPC setting. Additionally, OpenFOAM was the software used in the most recent published studies of catheter CFD simulation [80, 81, 100]; thus, results obtained using this software can be compared to previous relevant work in this field.

As with most computational simulations, OpenFOAM's operation can be divided into 3 main categories: pre-processing, solving, and post-processing. It has a standard directory structure and all of its operations are initiated via a command terminal by typing the relevant commands, found in the OpenFOAM user guide. An OpenFOAM case directory contains all of the files and scripts that are required for simulating a fluid dynamics model. The case directory initially contains 3 subdirectories: "0", "constant", and "system"; after the solving process, it may contain additional subdirectories. The "0" subdirectory contains all information pertaining to initial conditions (at time $t = 0$), namely the initial pressure and

velocity fields. The “constant” subdirectory contains all information about the fluid properties, geometry, mesh, and velocity/pressure boundary conditions. Lastly, the “system” subdirectory contains all computational information pertaining to the solver, including discretization schemes, tolerances, and simulation control parameters such as the number of allowed iterations. The scripts and dictionaries contained within these subdirectories follow standardized formats and are written in the C++ coding language. Simulation parameters, therefore, can be easily changed by the user by modifying and saving these text files accordingly. An example of OpenFOAM’s standard file structure is presented in Figure 3.1.

3.2.2 Initial 2D Model

The initial model of the CSF flow through a catheter was limited to two dimensions. The motivation behind starting the CFD modeling with a two-dimensional (2D) model was to gain a conceptual understanding of catheter flow and of the properties required for an adequately accurate CFD simulation in OpenFOAM. Some discrepancies between the flow observed in the 2D model and the later three-dimensional (3D) model precluded the use of the 2D model as an adequate representation of real catheter flow for parameter sensitivity and optimization studies. However, creating the model was a crucial first step for initial characterization of CSF flow. Because the 2D model was lightweight computationally, many iterations could be performed in a relatively short period of time to accelerate model progression. These preliminary trials were the basis for later modifications implemented in the 3D model, including the identification of key

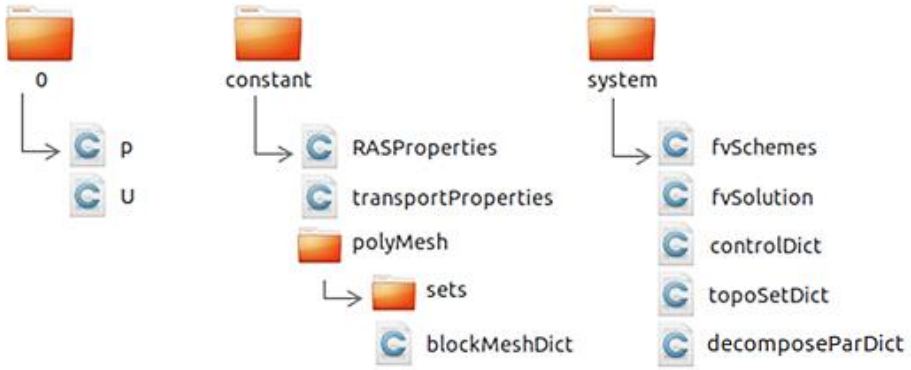

Figure 3.1 OpenFOAM basic case directory file structure, before execution of a solver. *Note*: several files were added to reflect the cases run in this study. Individual case file structure may vary for other types of simulations.

geometric parameters, meshing and sampling methods, and gaining a general familiarity with OpenFOAM.

Model Geometry and Mesh Creation

The 2D geometry of the model was taken as a cross-section of a generalized three-dimensional (3D) fluid domain (see Figure 3.2). Domain symmetry was used as a justification to further cut this cross section in half. Since all geometries in OpenFOAM must be described in 3 dimensions, the cross-section was given an arbitrary thickness in the z-direction, which was necessary but had no impact on the 2D model solution. The generalized domain consists of a catheter placed in the center of a cylindrical chamber representing an enlarged, CSF-filled ventricle. The catheter outlet is located outside the walls of the chamber. This simulates the placement of a catheter in-vivo as it extends past the ventricle into the brain parenchyma and out of the patient's cranium, where it then connects to the rest of the shunt device. The model simulates a case of non-communicating hydrocephalus, in that the catheter is the only outlet for CSF to exit the ventricle and the only inlet flow is from the slow, steady production of CSF within the ventricle. Fluid-solid interactions between the CSF and the catheter or ventricle were not included in this simulation, as the fluid flow is very slow and is not

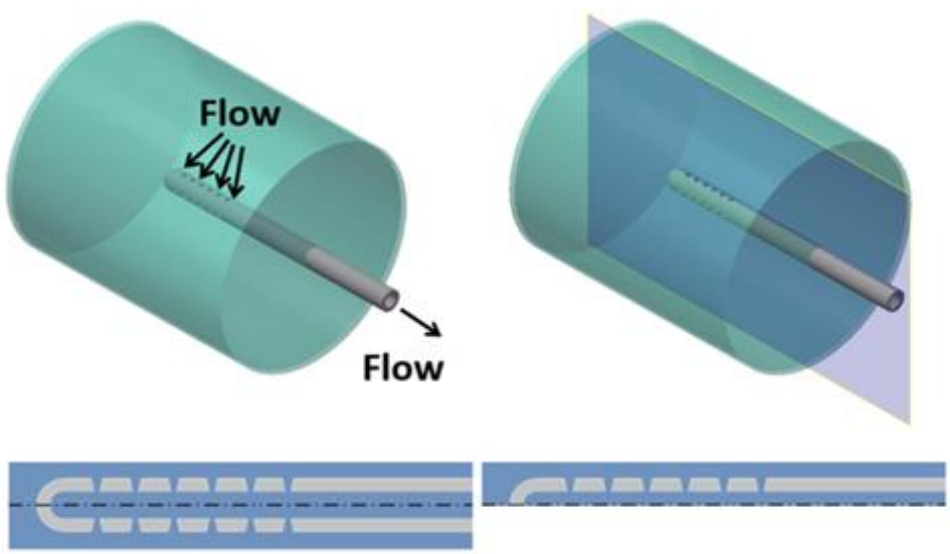

Figure 3.2 *Top Left*: Diagram showing the 3D model of a catheter in a ventricular chamber. *Top Right*: Cutting plane used to generate a 2D cross-section of the 3D fluid domain. *Bottom Left*: Example of full 2D cross-section and *Bottom Right*: Example of half of the 2D cross-section.

expected to influence the geometry of either body considerably (in this case, the ventricular “chamber” is of constant volume and the dynamic effects of a shrinking ventricle are not considered). Therefore, the fluid domain was the only one of interest for this model. The solid parts of the catheter and chamber were not modeled, but only included as boundary “walls” with no thickness.

In OpenFOAM, both the fluid domain geometry and the computational mesh are defined in the “constant” subdirectory. The fluid domain and catheter geometry were modelled with OpenFOAM’s *blockMesh* utility, using the dictionary file *blockMeshDict*. When run, *blockMesh* defines the boundaries of the geometric shapes (points, edges, arcs, etc.), and dividing them into “blocks”, which are then divided into finer grids based on the user’s specifications outlined in *blockMeshDict*. This utility can produce a highly predictable, structured mesh, comprised solely of hexahedron or “brick” type elements. It was selected, instead of some of the more complex unstructured mesh utilities offered in OpenFOAM, because the user can systematically control all meshing parameters to build the mesh “by hand”. The final mesh has finer grids along the areas of interest, around the catheter inlet holes, and coarser grids around the borders of the cylindrical chamber (see Figure 3.3 on following page).

Now the domain and mesh generation could be controlled via a template that receives input parameters. For this model, and later for the expanded 3D model, a Python script called *preProcessing.py* was written as such a template, to create a unique mesh when supplied with a catheter’s geometric parameters. Each time parameters were supplied to the script, a new set of point, edge, arc, and block definitions were generated for a new *blockMeshDict* file. The command *blockMesh* then used that file to construct a new mesh for the supplied geometry. Building such a well-defined mesh template was key to ensuring the ability to reproduce a mesh of reliable quality in the later automated stages.

Fluid Properties and Boundary Conditions

To complete the model setup, fluid properties and boundary conditions also had to be specified for the simulated fluid domain. Since CSF is comprised mostly of water (see Section 2.4.1), it is acceptable to substitute its fluid properties in the simulation for those of water, which are more well established in the literature. As part of OpenFOAM’s calculation of the Reynold’s number, $\mathrm{Re} = \frac{\mathrm{d}|\mathrm{U}|}{\nu}$, a value for the fluid’s dynamic viscosity ν must be specified. For water at a body temperature of 37 °C, $\nu = 0.6959 \times 10^{-6}\ \mathrm{m}^2/\mathrm{s}$. This value is set within the *transportProperties* file in the “constant” subdirectory. Additionally, the turbulence model,

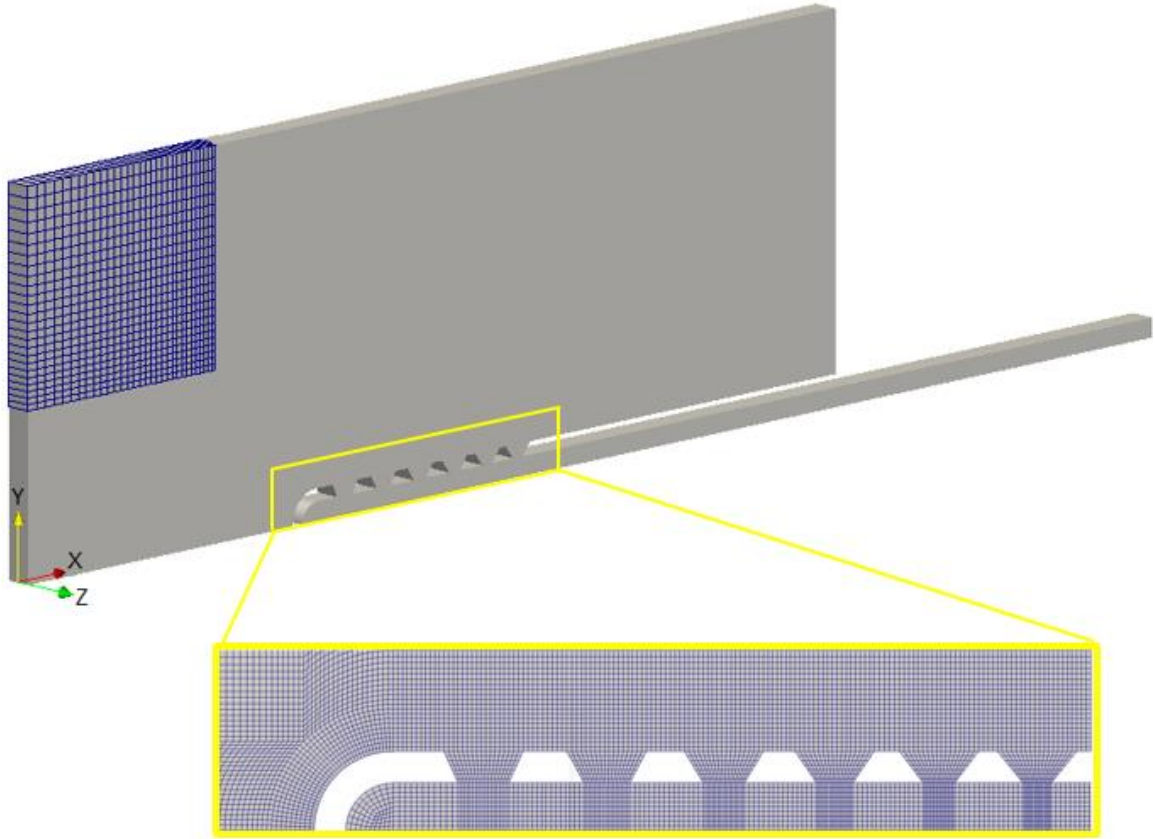

Figure 3.3 *Top*: Example of a 2D fluid domain model (with redundant 3rd dimension along Z axis) showing partial coarse mesh in outer area. *Bottom*: Close-up view of finer mesh generated around the catheter inlet holes area.

or lack thereof in this case, is defined in the *RASProperties* file, located also in the "constant" subdirectory.

The initial velocity and pressure conditions are set in the "0" time directory, in the files p and U respectively. Since this simulation solves for the steady-state case, the initial conditions are the boundary conditions. For the boundary faces normal to the z-direction (thickness of cross-section) the "empty" keyword is used, as there is no flow occurring in this direction. Since the cross-sectional domain has also been cut in half lengthwise along the catheter axis, a "symmetry" boundary condition is applied to the face created along this cut. The inlet is designated as the face of the cylinder opposite to the catheter outlet, the circular face from which fluid exits the catheter. The outlet velocity is set to match a constant physiological flow rate of 0.35 mL/min. For a catheter with inner diameter 1.5 mm, this velocity is equal to 0.0033 m/s. Varying the catheter inner diameter causes the velocity to change in order to maintain the same flow rate. The inlet is given a boundary condition of "zero gradient" so that the outgoing flow is equal to the incoming flow. As for pressures, since the exact pressure values for an incompressible flow in a channel are not of interest, but only the pressure differences, the pressure is set to be a fixed value of 0 at the inlet and "zero gradient" on the outlet.

Solution Algorithm and Settings

With the mesh created and boundary conditions set, the next step of the simulation is to run the CFD solver. OpenFOAM offers several standard solution algorithms that each are best suited to solving different flow regimes and cases. For incompressible, steady-state flow of a Newtonian fluid, the *simpleFoam* solver is well-suited, and so this solver was selected for the catheter flow simulations. This solver couples the Navier-Stokes equations with an iterative procedure. This iterative process is performed at each of the nodes of the computational mesh and each finite volume is related to its neighbors via volumetric flux. The Navier-Stokes equations describe the relationship between pressure and velocity in a fluid.

In three dimensions, the steady-state Navier-Stokes equations are formulated as shown on the following page, with ρ as the fluid density, μ as the fluid viscosity, p as the fluid pressure, and u, v, w as the components of the velocity in the x, y, z directions respectively. Note that gravity is accounted for as a body force, with the values of g_x, g_y, g_z dependent on the orientation of gravity with respect to the chosen set of coordinates. This set of equations must be solved numerically, as no analytical solution is available for $p, u, v,$ and w.

Continuity:
$$\frac{\partial u}{\partial x}+\frac{\partial v}{\partial y}+\frac{\partial w}{\partial z}=0$$

Momentum: (x-direction)
$$\rho\left(u\frac{\partial u}{\partial x}+v\frac{\partial u}{\partial y}+w\frac{\partial u}{\partial z}\right)=-\frac{\partial p}{\partial x}+\mu\left(\frac{\partial^2 u}{\partial x^2}+\frac{\partial^2 u}{\partial y^2}+\frac{\partial^2 u}{\partial z^2}\right)+\rho g_x$$

Momentum: (y-direction)
$$\rho\left(u\frac{\partial v}{\partial x}+v\frac{\partial v}{\partial y}+w\frac{\partial v}{\partial z}\right)=-\frac{\partial p}{\partial y}+\mu\left(\frac{\partial^2 v}{\partial x^2}+\frac{\partial^2 v}{\partial y^2}+\frac{\partial^2 v}{\partial z^2}\right)+\rho g_y$$

Momentum: (z-direction)
$$\rho\left(u\frac{\partial w}{\partial x}+v\frac{\partial w}{\partial y}+w\frac{\partial w}{\partial z}\right)=-\frac{\partial p}{\partial z}+\mu\left(\frac{\partial^2 w}{\partial x^2}+\frac{\partial^2 w}{\partial y^2}+\frac{\partial^2 w}{\partial z^2}\right)+\rho g_z$$

The solver *simpleFoam* uses the SIMPLE (Semi-Implicit Method for Pressure-Linked Equations) algorithm to numerically approximate $p, u, v,$ and w. The algorithm performs the following 8 steps in an iterative manner:

1. Set the boundary conditions.
2. Solve the discretized momentum equation to compute the intermediate velocity field.
3. Compute the mass fluxes at the cells faces.
4. Solve the pressure equation and apply under-relaxation.
5. Correct the mass fluxes at the cell faces.
6. Correct the velocities on the basis of the new pressure field.
7. Update the boundary conditions.
8. Repeat until a converged solution has been reached.

A given solution's convergence status is based on assessing the equation residual, a measure of the normalized error for a given variable (pressure, velocity, volumetric flow rate) over successive iterations of the method. The residual acts as a measure of the solution's accuracy. When *simpleFoam* is run, a log is generated that includes information pertaining to the initial residual, evaluated at the beginning of an iteration based on current *p* and *U* field values, and a final residual calculated at the end of each iteration after the fields have been re-evaluated.

All solver settings reside within the "system" directory. The numerical and discretization schemes are set within the file *fvSchemes*. This allows the user to designate what methods are used for approximating gradients and interpolations. "Gauss linear" and "Gauss upwind" schemes were selected as they have been proven to work well with similar steady-state, incompressible flow cases. Numerical convergence criteria and relaxation factors also influence the numerical setup; these are changed within the file *fvSolution*. After discretization, solving the

sets of linearized equations is done by a preconditioned (bi-) conjugate gradient algorithm: PCG/PBiCG for solving symmetric/asymmetric matrices respectively.

The solver is set up to stop iterating once one of the following convergence criteria are met: if the residual falls below a specified tolerance, if the ratio of current to initial residuals falls below a specified relative tolerance, or if the number of iterations exceeds a maximum specified in the file *controlDict*. In order to achieve a sufficiently accurate solution, the tolerance was set to 1×10^{-6} and the relative tolerance was set to 0.01 for both *p* and *U*. The maximum number of iterations was set to 1000. Under-relaxation is a technique for improving computational stability, particularly in solving steady-state problems, by introducing a relaxation factor $0 < \propto < 1$. The relaxation factors for both *p* and *U* were set to 0.7 in order to balance solution convergence stability, which increases as $\propto$ gets larger, and the rate of convergence, which slows as $\propto$ gets smaller.

In addition to setting the maximum number of iterations, the *controlDict* file is also responsible for specifying the outputs for the simulation. The number of time directories (for steady-state simulations these are simply iteration directories) kept and purged is specified here as well as the precision of the data recorded and how often the data is recorded. Additionally, the values to be sampled from predetermined locations in the computational domain and mode of their sampling are also defined here. This will be discussed in further detail in the next section.

Flow Rate Sampling

Since the objective of the simulations in this study was to characterize the flow rate patterns of flow through ventricular catheters, the values of the flow rates at the inlet holes and outlet needed to be sampled. Though methods of post-processed sampling are available in OpenFOAM, using the dictionary file *sampleDict*, it was decided that iterative sampling would be more useful as it could be used as another indicator of solution convergence (i.e. if the flow rate residuals were sufficiently small, it would serve as another criterion for convergence). Therefore the utility *topoSet* was chosen to create sets of faces through which the inlet hole flow rates could be monitored at specified points in the iterative solution.

Creation of the face sets was defined in the file *topoSetDict*, located in the "system" directory. In 2D, the faces were one cell thick in order to be easily defined using the *boxToFace* method, which uses vertex coordinates to define a box that surrounds the faces in question. Such a box was defined for each inlet hole, so that when the command *topoSet* was issued, face sets were generated and placed in the folder "constant/polyMesh/sets". In 3D, another method was utilized as the faces were not as easily defined as in the 2D case. In the file *controlDict*, these

face sets are referenced and the mass flow rate “phi” is summed over all the faces comprising each inlet hole to give a single flow rate value for each hole. When *simpleFoam* is run, this sampling is performed at the intervals specified in *controlDict*. In this study, values were sampled every 100 iterations, and reported to a newly generated folder, *postProcessing*, in the case directory. Each hole inlet is given a separate subdirectory and log within this folder. A Python script, *postProcessing.py* was written to collect this flow rate data and calculate statistics based on the flow rate distribution among the inlet holes.

3.2.3 Expanding the 2D model to 3D

Transitioning the 2D case to 3D involved several modifications, though the same basic principles for mesh creation, numerical solution, and flow rate sampling remained the same for both cases. In the 3D case, the symmetry of the domain was again used to simplify the problem: a quarter-section of the domain was used in order to preserve the fact that there were 4 rows of circular holes in the catheter (see Figure 3.4 below). This important design feature was not present in the 2D model and was the primary motivation for switching to a 3D representation for the later parts of this study. The 2D model used a symmetry that would have represented the inlet holes as rectangular slots or channels when expanded to 3D, rather than representing them as the round orifices found in real catheters.

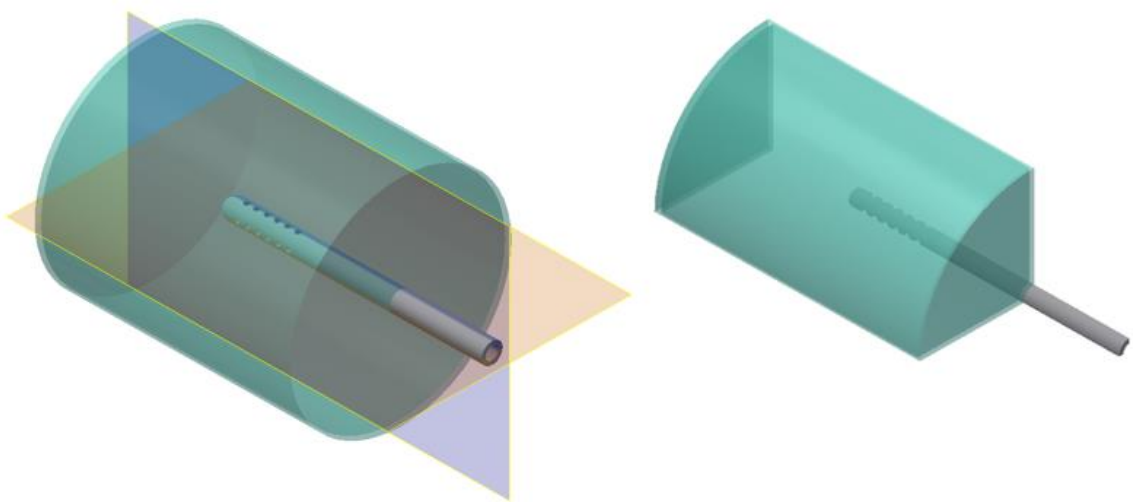

Figure 3.4 Example of a quarter-section model of the 3D domain, obtained by using 2 cutting planes.

While some of the flow characteristics of these two representations are comparable, they are nevertheless fundamentally different. This can be observed by taking the same catheter geometric parameters and implementing them in both the 2D and 3D models. The results, shown in Figure 3.5 on the following page, are qualitatively similar, but still markedly different, showing a 9.4% difference in the calculated standard deviation of the relative inlet flow rates. Since this standard deviation would serve as the value of interest in the later optimization stages, such an error was deemed unacceptable and therefore precluded the use of the 2D model as a sufficiently accurate representation of catheter flow.

The main challenge in adapting the methods used in the 2D case to a 3D domain was in creating a new meshing algorithm with *blockMesh*. In order for the meshing template to remain sensitive to the same parameters, it would have to be built “by-hand” again, so that the definition of the points, edges, and arcs remained consistent as parameters were changed. This was tedious to do in 2D, but was at least easy to follow visually, and the mesh skeleton consisted of only around 200 points and around 70 blocks. In 3D, such a task became unfeasible as the number of points grew to around 700 and the number of blocks to around 400. Therefore, after a schematic was built for a single section of the domain (for instance a section of the catheter that included a hole), the mesh definitions were automated and looped to create several such sections. See Figure 3.6 on page 37 for an example of a meshed 3D domain. This approach made meshing manageable, but other sections had to be meshed individually, such as the rounded catheter tip.

The meshing template was incorporated into the Python script *preProcessing.*py and modified for the 3D case. In order to make the 3D case ready for an automated iterative solver, this file contained not only instructions for generating *blockMeshDict* files based on a given parameter set (including the number of holes), but now also contained instructions for generating the *controlDict* and *topoSetDict* files that also depend on geometric parameters. The *controlDict* file normally wouldn’t be influenced by the geometry, but when the number of holes is changed, so is the number of required face sets to be iteratively sampled, a number defined in *controlDict*. Therefore the *preProcessing.py* script was a key component of streamlining the setup process for each individual 3D case.

Other modifications to the OpenFOAM input files had to be made as well. The domain boundaries no longer required the “empty” boundary conditions in the Z-direction, as this component of the velocity was now relevant. Also, the symmetry boundary condition had to be expanded to include the faces of the boundaries created by the quarter-section cut on the XY and XZ planes. In terms of sampling, the faces at the hole inlets that needed to be defined for *topoSetDict*

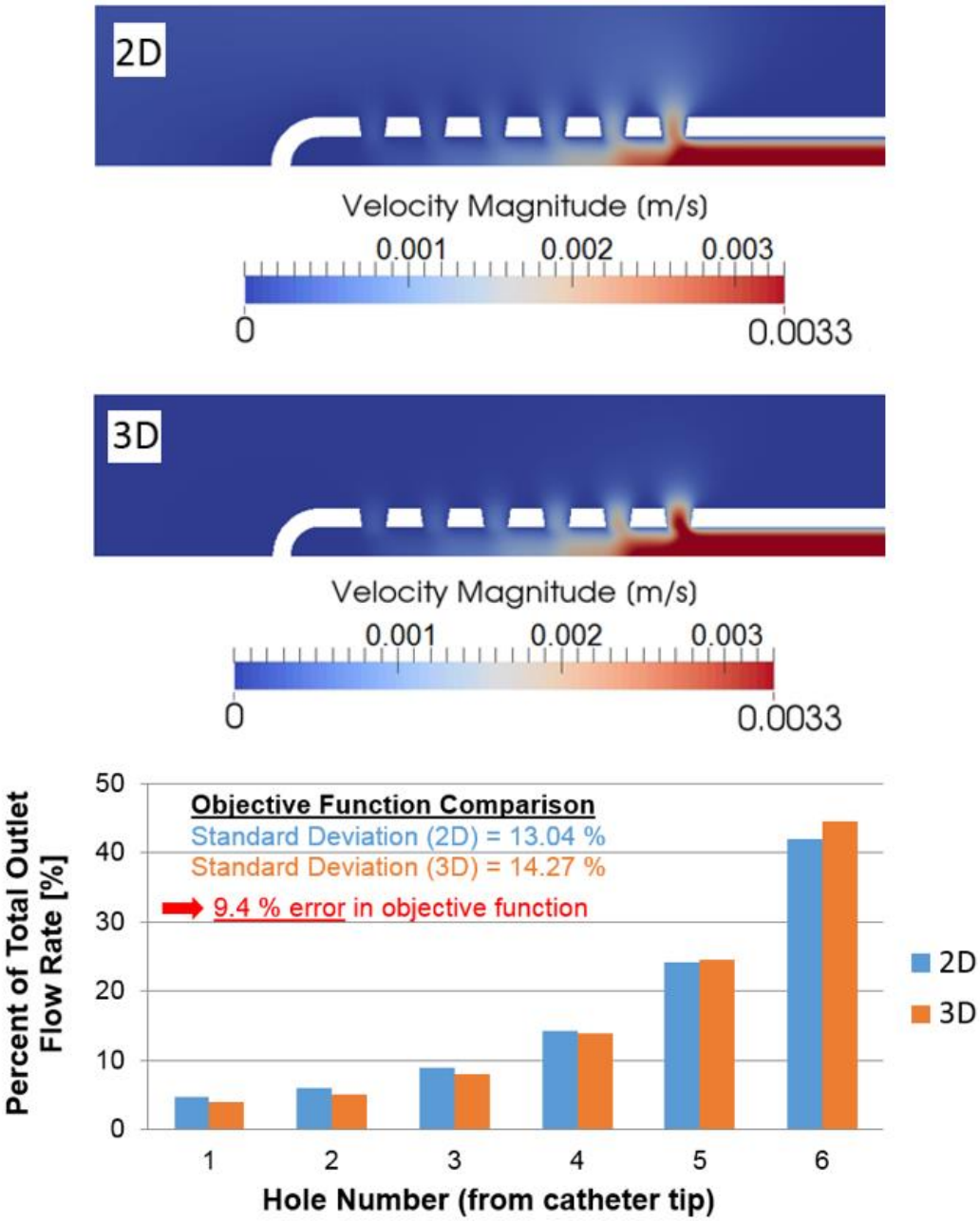

Figure 3.5: Results of running simulations in OpenFOAM with identical geometric parameters. *Top*: 2D planar domain velocity field. *Middle*: 3D quarter-domain velocity field (only XY plane shown). *Bottom*: Graph comparing flow rate distributions for the two simulations.

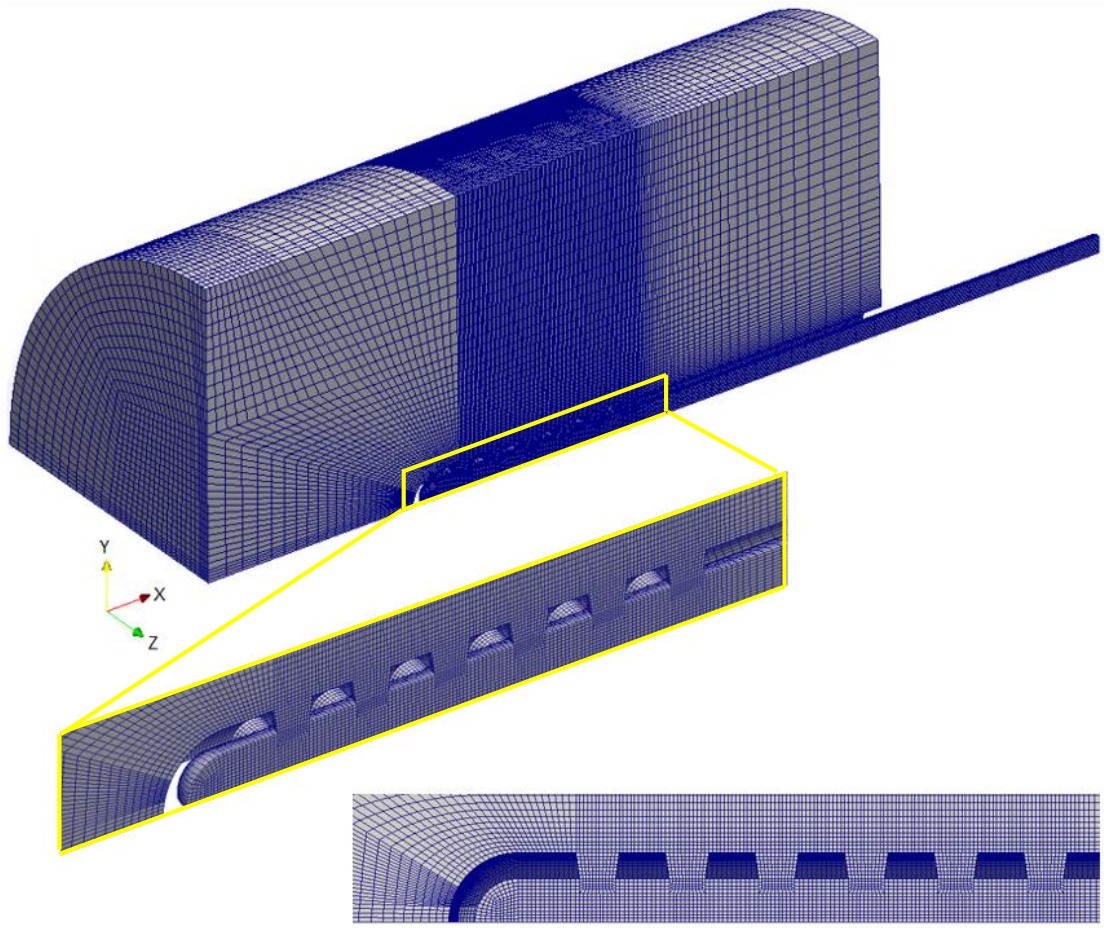

Figure 3.6 *Top*: Example of a 3D mesh over the entire domain. *Bottom*: Close-up views of the mesh around the hole inlets. Notice fluid filled holes extend in both +Y and -Z directions.

were now more complex, so patches for the hole inlets had to be separately defined in *blockMeshDict*. Then in *topoSetDict* these patches were converted into "cells" using the *zoneToCell* utility and to faces using the *cellToFace* utility. One of the most obvious disadvantages of the transition from 2D to 3D was the increase in computational complexity. While the 2D cases had on average 30,000 cells per model, the 3D cases averaged around 350,000 cells for a model with a similarly fine mesh. This dramatically increased the solver execution time; the measures taken to address this challenge will be discussed in more detail in Section 3.3.2. One of these measures included running each OpenFOAM simulation in parallel, by defining domain decomposition to a specified number of processing cores in the file *decomposeParDict* that is found in the "system" folder.

3.3 Parameter Studies and Optimization

After creating an effective CFD model in OpenFOAM, the next goal of this research was to utilize the model as a basis for iterative design exploration and optimization. The basic design of the catheter would be kept intact – a closed, narrow tube with rounded tip, and several rows of punched inlet holes near the tip. There are many existing variations on this design in clinical use today, each with slightly different hole sizing and locations. However, the subset of designs included in this study are ones with 4 parallel rows of holes, spaced equally around the tube circumference, since this is the partially axisymmetric design represented by the 3D quarter-model created in OpenFOAM. For example, designs with staggered rows of holes are omitted from this study, although they are some of the more popular configurations. These designs would require a more elaborate CFD model, requiring more computational resources to run, and would therefore be less efficient for iterative design exploration than the quarter-model representation.

The goal of performing such iterative design investigations was to improve the fluid flow performance of the catheter, specifically to increase the uniformity of the flow rate distribution among the catheter's inlet holes. The differentiator between this study and previous attempts to reach a similar goal [79-81, 100] is the ability to vary the catheter geometry on a larger scale, instead of testing just one or a few designs through simulation. By systematically varying the geometry, certain trends can be ascertained and later used as engineering criteria or used to identify potential candidates for optimal design. Again, in this study, optimization of design is only considered as it pertains to the aforementioned aspect of the catheter's fluid dynamics. Other design criteria can certainly be identified and explored in the future, perhaps utilizing the methods outlined here, but these are outside the scope of this study.

3.3.1 Building an Automated Simulation Framework: DAKOTA

In order to simulate the many geometries required for design optimization, it was necessary to introduce a governing parameter manager that would select values for the geometric parameters to be tested using the CFD model. Essentially, this component provided the geometric inputs for OpenFOAM, collected the processed outputs from each simulation, and then methodically selected the next set of inputs for simulation. The software chosen for this purpose was the free, open-source software Design Analysis Kit for Optimization and Terascale Applications (DAKOTA®, Release 6.2, Sandia Corporation).

DAKOTA provides a script-based interface that interacts with simulation software such as OpenFOAM, and several forms of iterative analysis for use in applications such as optimization, uncertainty quantification, sensitivity/variance studies, and parameter estimation with nonlinear least squares methods. By using these methods, DAKOTA can enhance the utility of traditional computational methods by enabling their use as design tools, so that simulations may be used not just for single-point predictions, but also for automated, iterative evaluations of simulated design performance. Coupling DAKOTA to OpenFOAM allowed for a systematic exploration of the ventricular catheter design space.

Another benefit of DAKOTA's software package is that a user can try different iterative methods or meta-algorithms by simply changing only a few commands in the text input file and executing the new analysis. Exploring the various methods does not require intimate knowledge of the underlying software package, only an understanding of the theoretical applicability of the methods to the problem in question. Additionally, DAKOTA can manage parallel, concurrent executions of the computational model, whether on a desktop or high-performance cluster computer. This feature makes it a user-friendly choice for executing large numbers of independent simulations, as was necessary for the some of the studies conducted in this work.

The interface with OpenFOAM was created by employing DAKOTA's most-commonly used "loosely-coupled" format. Also known as a "black-box" coupling, this type of interface does not require DAKOTA to have any direct awareness of the internal details of the computational model, only to exchange data with the model by reading and writing short data files. The type of analysis to be performed is specified by the user in a text input file, along with the directory and file names associated with the computational model, and then Dakota automatically executes the simulation code by creating a separate, external process. Each time a new OpenFOAM simulation is called for, a separate work directory is created.

Implementing the Interface

DAKOTA analyses are run within a directory with a standardized file structure. A subdirectory *casebase* contains a template of the data necessary to run each OpenFOAM simulation. Within this directory are located the standard OpenFOAM case structure (see Section 3.2.1) as well as Python scripts for pre-processing and post-processing. As described in Section 3.2.3, the *preProcessing* script controls the creation of the CFD geometry, mesh, and sampled faces. It is actually a template with "place holders" for values of the parameters that will be varied in the DAKOTA analysis. An input file *dakota.in* includes definitions for the iterative methods used for the analysis, the input variables and their ranges, the objective function and its derivatives, and specifies all interface and input/output methods. This file is the heart of the analysis and contains all of the pertinent user-supplied information for how DAKOTA should execute the iterative analysis. See Figure 3.7 for an example breakdown of a Dakota analysis directory.

As part of the interface definitions in *dakota.in*, a separate script is called as the "analysis driver". This script is called *simulator_script* and resides in the main analysis directory as well. It basically gives the sequence of commands that must be run during each DAKOTA iteration (in this case, for each OpenFOAM simulation). For each iteration, the *simulator_script* calls for the entire template case directory *casebase* to be copied within the analysis directory and assigns the directory a unique name, such as *workdir.1*, *workdir.2*, *workdir.3*, etc. These will

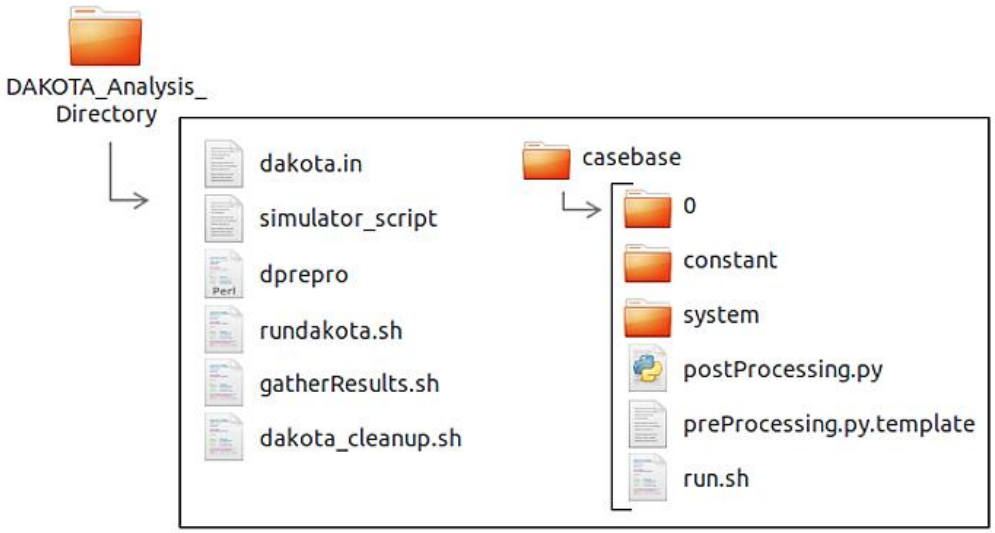

Figure 3.7 DAKOTA basic analysis directory file structure, before execution of an iterative method. *Note*: several files were added to reflect the typical analyses run in this study. Individual file structure may vary for other types of analyses.

serve as case directories for each individual CFD run. Next, the *simulator_script* begins the pre-processing stage of the iterative loop (see Figure 3.8).

Each copy of the case directory contains the template file for *preProcessing.py*, with the parameters intended for iteration marked with place holders. A Perl script *dprepro*, which is distributed with DAKOTA and is located in the analysis directory, is called by *simulator_script* to write a parameter input file for the copied case directory. Then *dprepro* replaces the place holders in the *preProcessing.py* template with values from the parameter file. Next, *simulator_script* executes the Python command for *preProcessing.py*, creating the *blockMeshDict*, *topoSetDict*, and *controlDict* files for the OpenFOAM case.

Following this, the rest of the typical OpenFOAM case commands and *postProcessing.py* are run by *simulator_script* and then the results of the CFD simulation are gathered and passed on to DAKOTA's result files. This constitutes the post-processing stage of the iterative loop. In such a fashion, each iteration is performed by DAKOTA until the desired number of executed evaluations is reached. The cases may be run in series or concurrently by DAKOTA, an option that is specified in the file *dakota.in*. When coupled with the "asynchronous" descriptor, the specified number of concurrent evaluations are all launched simultaneously. When running DAKOTA on multiple processors, this allows the cases to be run in parallel, saving time.

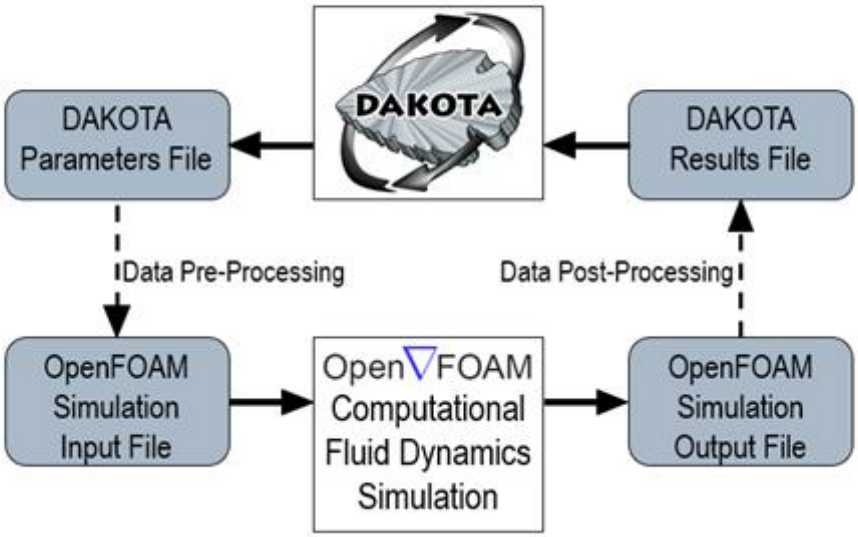

Figure 3.8 Flowchart loop showing the DAKOTA-OpenFOAM "black-box" or "loosely-coupled" interface format.

3.3.2 Minimizing CFD Execution Time

In preparation for the automated execution of thousands of simulations in OpenFOAM through the coupling with DAKOTA, the base 3D CFD case was reexamined for opportunities to reduce execution time as much as possible with minimal effect on the accuracy of the objective function. This involved utilizing the vector parameter study capability in DAKOTA, each time changing a different variable related to the execution of the CFD simulation, and analyzing the effects on execution time and on the objective function's accuracy. These variables included the computational domain size, the mesh fineness, and the simulation convergence criteria. By making small concessions in accuracy, the average simulation execution time and time per solution iteration were substantially reduced, in some cases from hours to minutes.

Slower-running, high-fidelity models were used for testing small sample groups, while the faster-running, low-fidelity models were used as a basis for the larger-scale studies. Because in the later stages, the objective was to compare flow profiles of various designs, the relatively minor reductions in accuracy did not present an obstacle to gaining a true understanding of the effects of changing the catheter geometry. Later, secondary simulations of designs of interest were conducted using the full degree of accuracy available.

Domain Reduction Study

In-vivo, the position of the catheter relative to the ventricle walls plays a significant role in the flow characteristics of CSF through the catheter. In future studies, a more accurate model of a catheter in a dynamic ventricular chamber that can expand or compress may shed some light on the interactions between the outflow of CSF from the ventricles and the corresponding changes in the catheter flow. However, the effects of the ventricle walls on flow and vice versa were not the focus of this study. Therefore, in this case, the boundaries of the fluid domain are placed far enough away from the catheter inlet holes so as to negate any noticeable effects on the flow.

However, in terms of computational efficiency, a relatively *small* domain is desirable so as to reduce the number of finite volume cells, and thereby reduce execution time required for the CFD simulation to converge. Therefore, a study was done to find the smallest computational domain that would still maintain a minimal influence of the chamber walls on the resulting inlet hole flow rates. Reduced computational domain boundaries were tested by incrementally bringing the walls closer in toward the catheter holes (see Figure 3.9 on page 44), while

keeping all other parameters constant, and recording the effects of these changes on the flow rate results. A relatively large initial domain with a distance $X = 16\,mm$ between the walls and the catheter holes was taken as a control, and subsequent simulation errors were calculated relative to the flow rates of this initial simulation. In this study, the simulations were all run until they satisfied the same convergence criteria, so each subsequent simulation required less iterations to reach convergence. Then, errors in both the relative flow rates of the individual holes and the flow rate standard deviation were calculated (see Table 3.1 below).

As can be noted in the results of the test in Table 3.1, the errors generally grow as the domain is made smaller, especially after the transition between $X = 6\,mm$ and $X = 4\,mm$, and the execution times improve. Both the average hole inlet flow rate errors and the flow rate standard deviation errors do not follow a consistently decreasing pattern. This is perhaps a sign that the domain size does not have a strong correlation to accuracy. Moreover, prior to the transition to $X = 4\,mm$, the errors observed were all extremely low, much less than 0.1%. This would indicate that only when the domain was significantly reduced to $X = 4\,mm$, were the “wall effects” noticeable.

After examining these results and considering their meaning, a value of $X = 8\,mm$ was chosen for the subsequent simulations, as it provided a drastic decrease in domain size while not significantly impacting accuracy. The low additional error of approximately 0.01% in the relative flow rates and standard deviation was deemed reasonably acceptable for the tradeoff in lower execution time to convergence (approximately 40% less than at $X = 16\,mm$). This substantial reduction in execution time justifies the small reduction in accuracy, as much of the outer domain does not contain the flow field of interest.

Table 3.1 Domain size reduction study results

X [mm]	Total Mesh Cells	Execution Time [s]		Average Hole Inlet Flow Rate Error [%]	Flow Rate Standard Deviation Error [%]
		Per Iteration	Until Convergence		
16	401412	0.870	1804.27	--	--
14	380108	0.945	1570.76	0.00695	0.00803
12	359156	0.936	1404.92	0.01109	0.01306
10	338684	0.871	1210.60	0.00452	0.00292
8	**316412**	**0.835**	**1060.11**	**0.01256**	**0.00846**
6	286412	0.844	906.86	0.03691	0.00474
4	239420	0.655	612.04	0.22852	0.09026

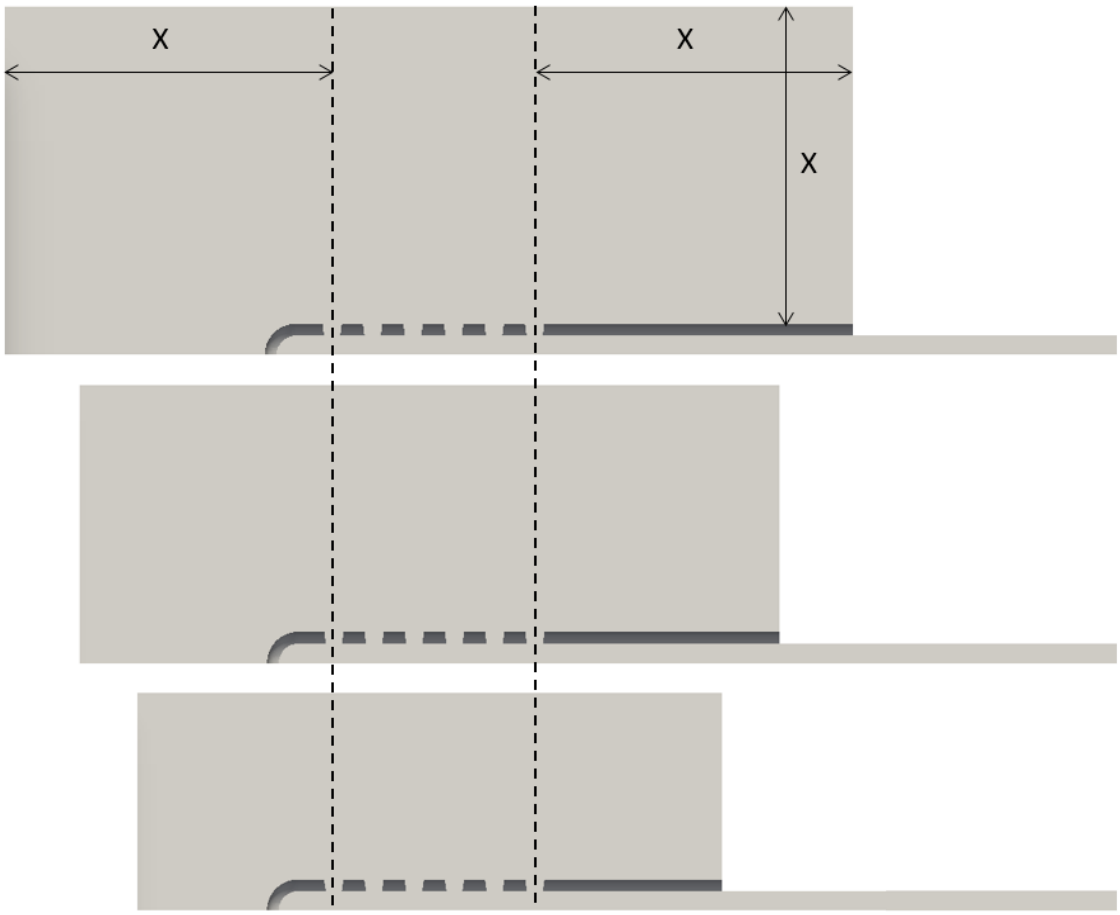

Figure 3.9 Example of 3 sample domains tested in the domain reduction study. Note that the catheter length and other dimensions were kept constant, while only the chamber size X was changed.

Mesh Refinement Study

Similarly, the minimal required mesh refinement for convergence was determined by testing several values for a parameter n, which represents the number of cells into which a given geometric length is divided. The results may be seen in Table 3.2. Since the areas of interest for sampling were the hole inlets, it was chosen to designate that n+2 would be the number of cells in the X-direction for all hole inlets. Other catheter dimensions could have also served this purpose, but the inlet holes were chosen to ensure that the mesh always contained a minimum number of elements from which to sample the flow rates through each hole. In case n was set to 0, there were at least 2 elements for each inlet.

This approach allowed for the smallest elements to be populated around the catheter inlets and wall boundaries, that were locations of significant behavior. The algorithm used for mesh population in the preProcessing.py script designated the element size to be used for each “block”. The number of elements and the linear “element stretching factor” in each direction (x,y,z) of a block are defined in the *blockMeshDict* file of each OpenFOAM case. A relatively fine mesh of n = 10 (each inlet hole with 12 cells in the X-direction) was used as a control for this study. Then the n value was incrementally decreased and the flow rate errors relative to the control were calculated, as well as the standard deviation error (see Table 3.2).

As expected, as n gets smaller, the errors generally increase. To achieve a target goal of relative errors less than 0.5%, in either the average flow rate error or the flow rate standard deviation error, the lowest n value permissible is n = 8. This provides approximately a 40% improvement in execution time per iteration, compared to the n = 10 case. Although there is a slight dip in the errors for n = 5, it is not consistent with the other error patterns and is therefore not an alternative to n = 8. An example of increases in mesh refinement is shown in Figure 3.10.

Table 3.2 Mesh refinement study results

n	Total Mesh Cells	Execution Time [s]		Average Hole Inlet Flow Rate Error [%]	Flow Rate Standard Deviation Error [%]
		Per Iteration	Until Convergence		
10	436104	1.209	2043.73	--	--
9	372652	1.029	1496.59	0.21229	0.17017
8	**300464**	**0.749**	**946.46**	**0.35902**	**0.28380**
7	215870	0.438	487.83	0.67439	0.53624
6	160807	0.316	295.70	0.81517	0.64639
5	105556	0.170	136.89	0.54448	0.43964
4	75280	0.123	74.50	1.06895	0.87774

Solver Convergence Criteria Study

The last variables to be tested in the effort to reduce computational time were those relating to solver convergence. As discussed in Section 3.2.2, the convergence of each CFD simulation is governed by several convergence criteria, specified for each case in the *fvSolution* and *controlDict* files of the “system” subdirectory. A simulation will be terminated when any one of the following three criteria is satisfied:

1. if the residuals for U and p (velocity and pressure respectively) fall below given solver **tolerances**, specified in *fvSolution*
2. if, for a given iteration, the ratio of final to initial residuals for both U and p fall below given **relative tolerances**, specified in *fvSolution*
3. if the number of iterations exceeds a **maximum number of iterations**, specified in *controlDict*

Since these criteria obviously affect the solution accuracy and execution time in a very direct way, it was determined that they should be tested for their effect on the flow rate and standard deviation errors. The selected values for domain size and mesh fineness from the previous studies in this section were set as a base for this study as well. All other parameters, including the domain geometry, were also kept constant. Both solver tolerances and relative tolerances were set to the same values respectively in both their U and p definitions, to limit the number of variations. It is important to note that although the simulated pressure values were not directly of interest for these studies, the accuracy of the pressure values does affect the accuracy of the velocity values, as these outputs are linked by the SIMPLE algorithm.

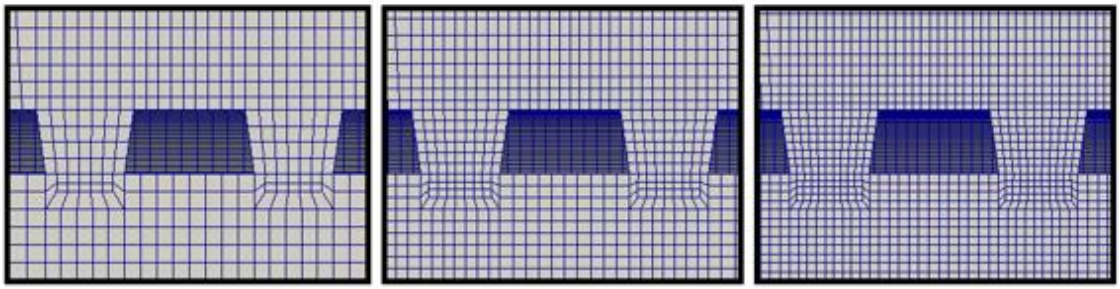

Figure 3.10 Example close-up views of inlet hole meshes with increasing mesh fineness number *n*. *Left*: *n* = 5, *Middle*: *n* = 7, *Right*: *n* = 9.

To isolate the effect of changing the solver tolerances, the relative tolerances were all set to 0 in order to force the solution to converge to the solver tolerance. Also, the maximum number of iterations was set to a very high value of 10,000 to allow the solver to reach the various tested tolerances without being cut off by this additional limiting criterion. The control test was performed with a very demanding tolerance of 1×10^{-8}. Subsequent tests increased this tolerance on a logarithmic scale, thereby causing the number of iterations required to convergence to grow.

From the results, shown in Table 3.3, it can be seen that increasing the tolerances from 1×10^{-8} to 1×10^{-6} had almost no effect on the accuracy of the values of interest. Only when increased to 1×10^{-5} was there a noticeable effect on the accuracy. Tolerances of 1×10^{-4} and 1×10^{-3} produced extremely fast convergence, but the errors in the values of interest grew to over 1%. Therefore, it was decided that tolerances of 1×10^{-5} were acceptable, producing errors less than 0.005%, but that further increases to the tolerance would not be acceptable. Next, the parameter of relative tolerance was reviewed in a similar way, beginning with a small relative tolerance and gradually growing larger. However, the results of the study for relative tolerance were inconclusive. For relative tolerances above 1, the simulation did not converge properly and so those results were discarded. For relative tolerances below 1 (0.1, 0.01, 0.001, etc.), the convergence patterns for the simulations were nearly identical, indicating that the relative tolerance criterion was not the one responsible for ending the iterative process in these cases. Rather, it seems, that solver tolerance was again the controlling criterion. It was determined that a constant relative tolerance of 0.01 should be used.

A similar problem existed with varying the maximum number of allowed iterations. Such a test would also have been inconclusive, since the changes in accuracy would have stemmed from forcing the simulation to end prior to it rea-

Table 3.3 Solver tolerance study results

Tolerance	**Execution Time [s]**		**Average Hole Inlet Flow Rate Error [%]**	**Flow Rate Standard Deviation Error [%]**
	Per Iteration	**Until Convergence**		
1×10^{-8}	0.655	1684.49	--	--
1×10^{-7}	0.561	1037.09	< 0.0001	< 0.0001
1×10^{-6}	0.527	590.12	0.00053	< 0.0001
1×10^{-5}	**0.530**	**289.47**	**0.00381**	**0.00255**
1×10^{-4}	0.587	100.34	1.61748	1.14882
1×10^{-3}	0.709	39.68	15.5939	13.8822

ching convergence. Using results with differing levels of convergence would not allow for a quantifiable or robust comparison. After performing many simulations, it was found that if given the same boundary conditions, most simulations converged to the solver tolerance before reaching 1000 iterations. So, to act as a cap for the time spent on each simulation, 1000 was chosen as the maximum number of allowed iterations for the subsequent simulations. See Figure 3.11 for an example graph of the numerical residuals for a typical simulation.

3.3.3 Design Parameters

When broken down into its constituent dimensions, one finds that even the relatively simple geometry of the ventricular catheter is defined by a large set of variables. For example, each individual inlet hole has several dimensions associated with it; so, if each hole is considered separately, the total number of design parameters can easily exceed 20 or even 30, depending on the number of holes per row. Although 20 or 30-dimensional design investigation is *not impossible*, especially with the help of high-performance computing, it still presents many mathematical and computational challenges that make it unfeasible and impractical for this investigation. Therefore, the number of design variables had to be reduced in order to bring the dimensionality of the parameter space down to a more manageable number. In addition, the ranges of each variable were minimized to the extents possible in order to further reduce the parameter space allowed for exploration.

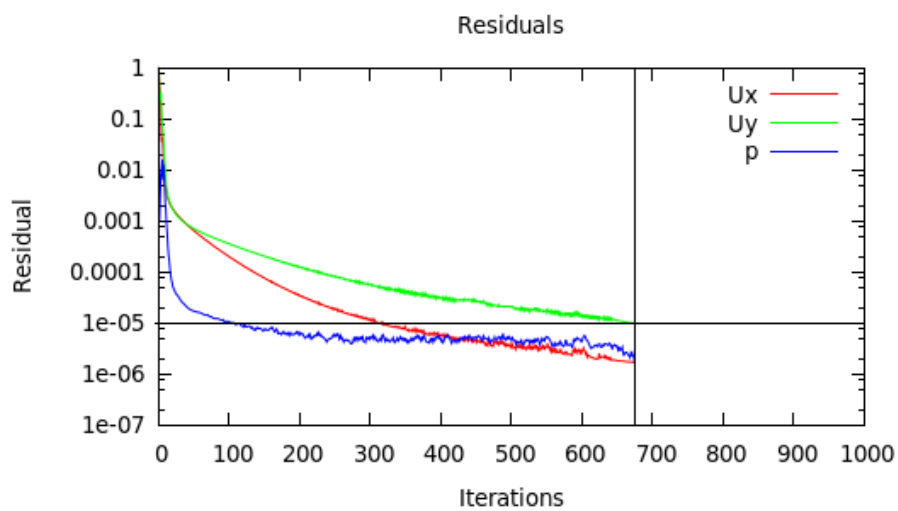

Figure 3.11 Example graph of CFD simulation numerical residuals. Ux is velocity in x-direction, Uy is velocity in y-direction (Uz is the same), and p is pressure. Note that the simulation ends at around 675 iterations, converging prior to the 1000 iteration limit.

This reduction required the application of certain assumptions and simplifications, as well as some knowledge of the engineering physics behind the catheter's geometry. The parameters of interest included catheter wall thickness, distance from catheter tip to the first inlet hole, spacing distances between inlet holes, inlet hole diameters (interior), and inlet hole degree of tapering (see Figure 3.12). These parameters were chosen because they had the greatest likelihood of affecting the inlet hole flow rate distribution, both intuitively and based on evidence in the literature. Individual inlet hole diameters were characterized by the diameter measured at the interior lumen of the catheter, as opposed to the larger exterior diameter created by the hole taper, because it is the interior diameter which limits the inlet flow rate and so this parameter was of greatest interest. Maximum diameters were defined as the diameter at which two holes, spaced 90° apart, would begin to intersect at the interior catheter lumen.

Tapering of the holes is usually a byproduct of the hole punching process. Compressive and tensile stresses cause distortions at either end of the hole during punching and the taper is created after the material undergoes relaxation. Drilling and laser hole fabrication techniques may reduce this phenomenon and can produce nearly straight holes. Therefore, this parameter is dependent on both the materials and manufacturing process involved. To estimate a range for possible tapers, photographs of punched sample catheters, from a study demonstrating the

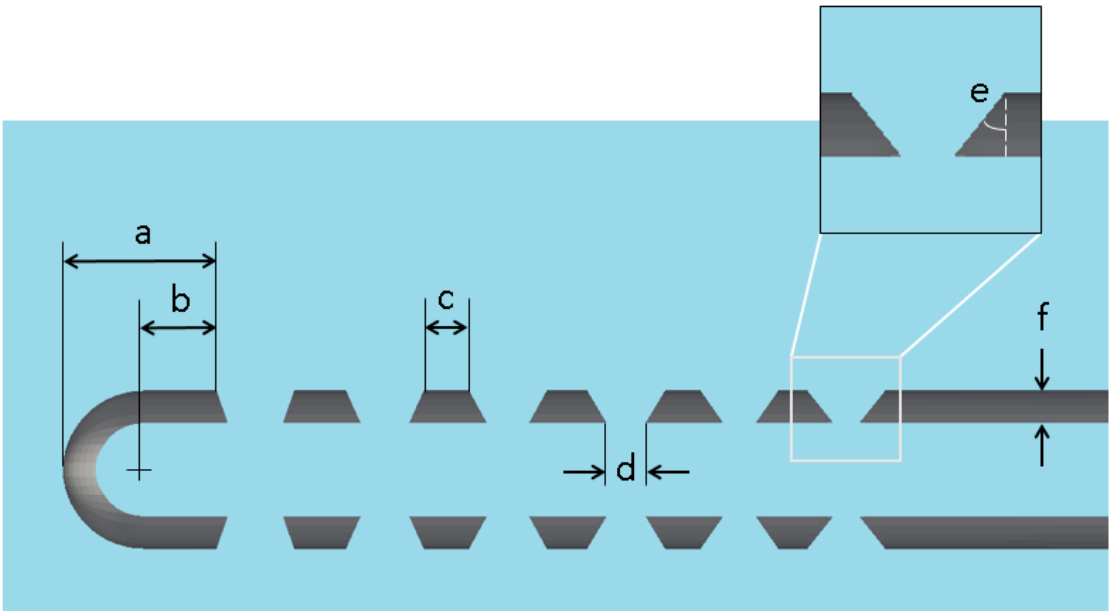

Figure 3.12 Cross-sectional schematic of catheter geometric parameters: a) distance from catheter tip to the first inlet hole, b) first hole spacing, c) subsequent hole spacing, d) interior hole diameter, e) degree of hole tapering, f) catheter wall thickness.

effects of catheter hole size on cellular adhesion [91] were examined to estimate common degrees of tapering. As for hole spacing, it was deemed most important to track the exterior spacing, as opposed to the interior spacing, as the hole tapers cause exterior spacing to be the smaller of the two. The minimum spacing between holes must be above a certain minimum value in order to preserve the structural viability of the catheter; therefore, it was of greater interest to track the exterior spacing parameter. Additionally, the overall section length containing the inlet holes is commonly limited to the 1.5 cm closest to the catheter tip, in order to increase the probability that the inlet holes remain inside the ventricle after surgical placement. These design considerations are summarized in Table 3.4.

Other variables remained fixed, such as the catheter internal diameter (ID) and number of holes. The ID was not varied, since doing so would require also iteratively changing the outlet velocity to maintain constant flow rate across simulations. For the fixed catheter ID of 1.5 mm used in the studies, the outlet velocity is set to 0.0033 m/s in order to meet the required 0.35 mL/min physiological flow rate. For a smaller ID of 1.2, for instance, the velocity would need to be 0.00515 m/s to attain the same flow rate. Changing the catheter geometry and the fluid velocity would not allow for direct comparisons between the models. Similarly, the number of holes was not varied, since changing this parameter fundamentally changes the flow rate distribution pattern. So it was decided to conduct separate sensitivity and optimization studies for each variation in the number of holes. Variations on configurations with any number of holes per row could be explored with the same CFD model template, by each time changing the parameter for “number of holes”. However, iterative analyses for the 6-hole design are the focus of the studies in this thesis.

Table 3.4 Design considerations for parameter ranges

Parameter	**Parameter Range**		**Considerations**
	Minimum	**Maximum**	
Inlet hole diameters	0.25 mm	Catheter ID x sin(45°)	Structural integrity of interior lumen, preventing large obstructions
Distances between inlet holes	2 x Wall Thickness	2.00 mm	Structural integrity, max. length of perforated catheter segment
Inlet hole degree of tapering	0°	20°	Fabrication process, sample values extracted from previous study
Catheter wall thickness	0.30 mm	0.70 mm	Structural integrity, PDMS extrusion limitations

3.3.4 Selecting an Optimization Strategy

Optimization is a general concept that can include the use of many different types of numerical methods, individually or in various combinations. In most design optimization problems, input parameters of interest are called “design variables” and the output or target variable is called the “objective function”. Selecting the best method(s) for an optimization problem is generally based on the characteristics of the objective function to be optimized and on the computational resources available. Here is a brief summary of the main choices to be made when selecting an optimization method in DAKOTA [114]:

1) Local vs global: Local methods are best suited for navigation to a minimum in the near vicinity of an initial point provided to the algorithm, while global methods can be used to search the entire range of a set of given input variables. Local methods, therefore, require identification of a “favorable” initial point, close to the function minimum.

2) Gradient-based vs. derivative-free: Gradient-based optimization methods are used to explore smooth, continuous objective functions, while derivative-free methods can be used to explore nonsmooth functions, like those containing noise or discontinuous peaks. Global methods are generally derivative-free. All optimization methods in DAKOTA require continuous variables.

The objective function chosen to explore catheter fluid performance was the standard deviation of the relative flow rates of the catheter’s inlet holes. The values comprising this function are derived from calculating the standard deviation of flow rates, which are a numerical approximation of a physical problem. Therefore, it is not likely that this function exhibits the smooth, continuous properties required for identification of a minimum using gradient-based methods. As the function is described in a hypervariate space, with more than 10 input variables, it is not easy to visualize the function using conventional plotting methods and to confirm this hypothesis. However, it is logical to assume that it is not a “well-behaved” function. Thereby, the use of gradient-based methods, while not to be ruled out completely, should at least be questioned in terms of the validity of the results they would produce.

Each of the input variables has, at least to begin with, a large, independent range of values that it can assume. With each of the values in the range having equal probability to be part of the optimal combination of variables, a global,

derivative-free optimization method would seem to be the best choice. However, most of these methods are relatively inefficient and would require many tens of thousands of function evaluations in order to sufficiently explore such an expansive, hypervariate parameter space. If, however, it would be possible to identify areas of interest within the parameter space, this could bring the optimization problem to a point where local methods may be used more effectively. For example, if a few thousand variable combinations are tested and between 5 - 10 points showing very low values of the objective function are identified, they may be used as the initial points for local methods.

With this strategy in mind, a few methods were used to perform an initial exploration of the parameter space, independent of any of the aforementioned optimization methods. The goal of this investigation was to characterize the influence of each parameter individually and to identify initial values for local optimization. The first method was to perform one-at-a-time sensitivity studies on each of the parameters of interest, in order to identify those parameters that individually had the most critical impact on the objective function. This knowledge helped to reduce the dimensionality of the parameter space, as well as to give guidance in selecting the best ranges of the remaining parameters for subsequent testing. After this series of tests, the remaining parameter space was explored in its entirety by using a Latin Hypercube Sampling (LHS) method. This is a statistical method used to generate a collection of input parameter sets that effectively cover the entire space. LHS divides the range of n variables into m subdivisions, which are equally probable, and ensures that there is one sample in each of the multivariate rows and columns created by the subdivisions.

This method ensures that the ensemble of random input selections is representative of the actual variability of the parameters, which puts it a step above completely random sampling. Orthogonal sampling is a further step above that ensures that the selections are a *very good* representation of the real variability; but generally, it has a requirement on the minimum number of samples for a given dimensionality. One of the advantages of LHS is that the number of samples is independent of the number of dimensions, allowing the user to select the desired number of samples. LHS was chosen for this reason, as orthogonal sampling would have required a very large number of samples for such a high-dimensional parameter space. Several thousand function evaluations were systematically performed using the LHS method, starting with very general parameter ranges, and subsequently zeroing in on specific ranges or variables. As described in Section 3.3.2, these large simulations were performed using the low-fidelity settings in OpenFOAM, so as to save on computational time. A 1000-sample LHS run could be performed on the single Dell workstation in 9.5 hours.

The high degree of coverage of the parameter space can be seen in Figure 3.13, where a 5-dimensional space, in this case of five hole radii, is shown as 2D couplings of each of the variables. A 10-dimensional parameter space, for instance, could similarly be decomposed using 100 2D plots. That notwithstanding, with a high-dimension parameter space, there is no guarantee that multiple iterations of similar combinations are sampled – each parameter set is unique and with so few samples, there is not much repetition of similar sets. This is the main disadvantage of LHS as opposed to orthogonal sampling.

After this initial exploration, several of the parameter sets that minimized the objective function in these LHS runs were gathered. Each one was verified to be unique, as opposed to simply a derivative of one of the others, and was set as an initial point for a subsequent local optimization run. The optimization method chosen for this study was the “coliny pattern search” method. This local, derivative-free optimization method was chosen as it can “walk” through the domain using a defined stencil of search directions. It is best suited for navigation to a local minimum in the vicinity of the initial point; however, it can sometimes exhibit limited

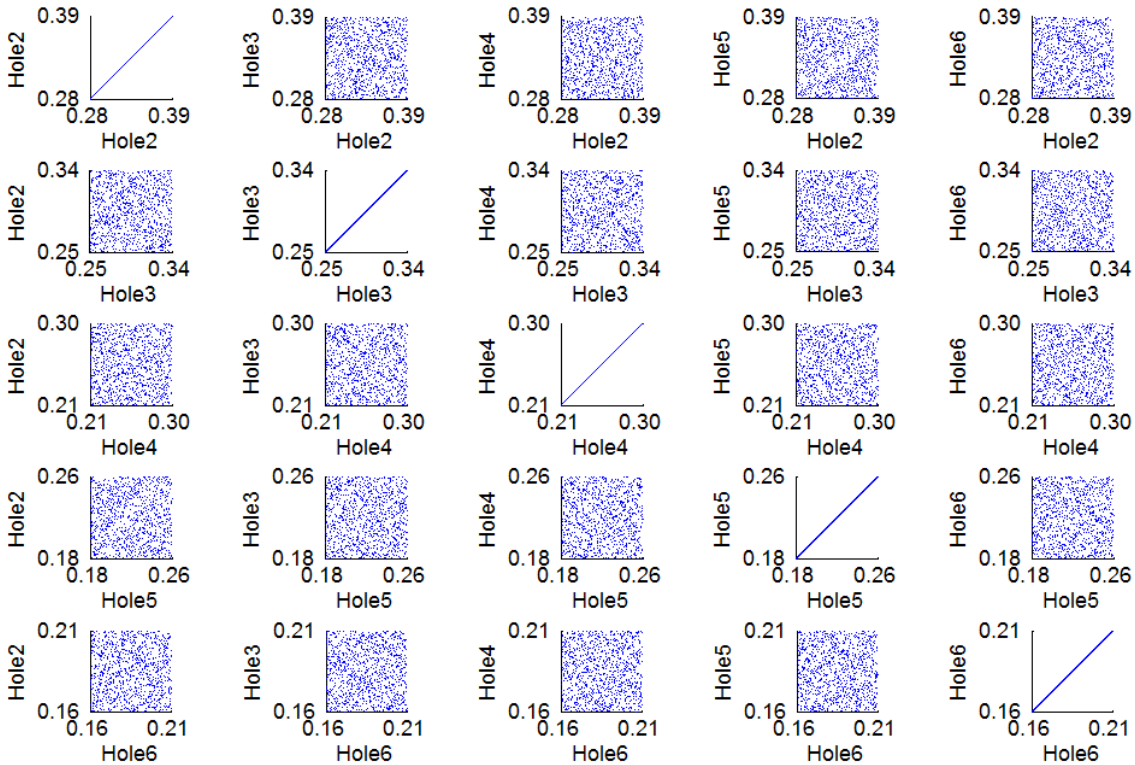

Figure 3.13 Coverage of 5-dimensional parameter space, in this case the radii of holes 2 to 6, sampled by 1000 samples using LHS. Parameter space is decomposed to 25 pairs of 2-parameter combinations.

global optimization abilities if the stencil allows it to “step over” local minima [114]. Optimized results from these final runs were run again using the high-fidelity CFD model and their fluid performance compared to standard catheter designs.

3.3.5 Running in Parallel

On the Dell workstation, using 4 core decomposition in OpenFOAM and serial evaluations in DAKOTA, 1000 low-fidelity runs took 9.5 hours. Low-fidelity runs were set with a wall distance X = 6, mesh fineness n = 5, and solver tolerance of 5 x 10-5. The result of these reductions in computational time amounted to estimated errors of between 0.1 and 1% in individual flow rate errors and less than 1% in the standard deviation (objective function) calculation. In order to further reduce execution time during these long runs, the high-performance computing resources, described in Section 3.1.1, were utilized.

After installing DAKOTA on the Darter supercomputer, which was done in the user’s directory of the Lustre parallel file storage system, it was coupled with Darter’s already installed OpenFOAM module, which is available to all users. Darter allowed DAKOTA to run several OpenFOAM simulations simultaneously from the subdivision of the system’s processors called the ‘aprun nodes’. DAKOTA is activated through the ‘login nodes’ subdivision using a PBS job scheduler and then runs as a higher level process, further scheduling each OpenFOAM run to individual compute nodes using the ‘asynchronous’ and ‘concurrent evaluations’ settings. A schematic of the parallel running structure of this DAKOTA-OpenFOAM framework on the Darter supercomputer can be found in Figure 3.14 on the following page.

For example, requesting 20 compute nodes via the PBS job scheduler gives DAKOTA the ability to run 20 function evaluations concurrently. Each of these is further decomposed by OpenFOAM’s *decomposePar* utility into each node’s 16 cores. Such a configuration reduces the total time required for the same 1000 low-fidelity runs, such as one of the LHS runs, from 9.5 hours to around half an hour, a much more acceptable time for such an engineering optimization application. Additionally, when high-fidelity OpenFOAM simulations are required in large numbers, running in parallel is the only *feasible* option for use in an actual engineering situation. Though running on more nodes can proportionally influence the run time, it was not appropriate for the studies run here. This is because the Darter supercomputer is a shared resource and requesting large portions of its compute nodes requires users to wait in a queue until the requested resources are made available. Therefore, 20 nodes was the maximum number requested at a time, and in this way, queue times were kept to a reasonable length.

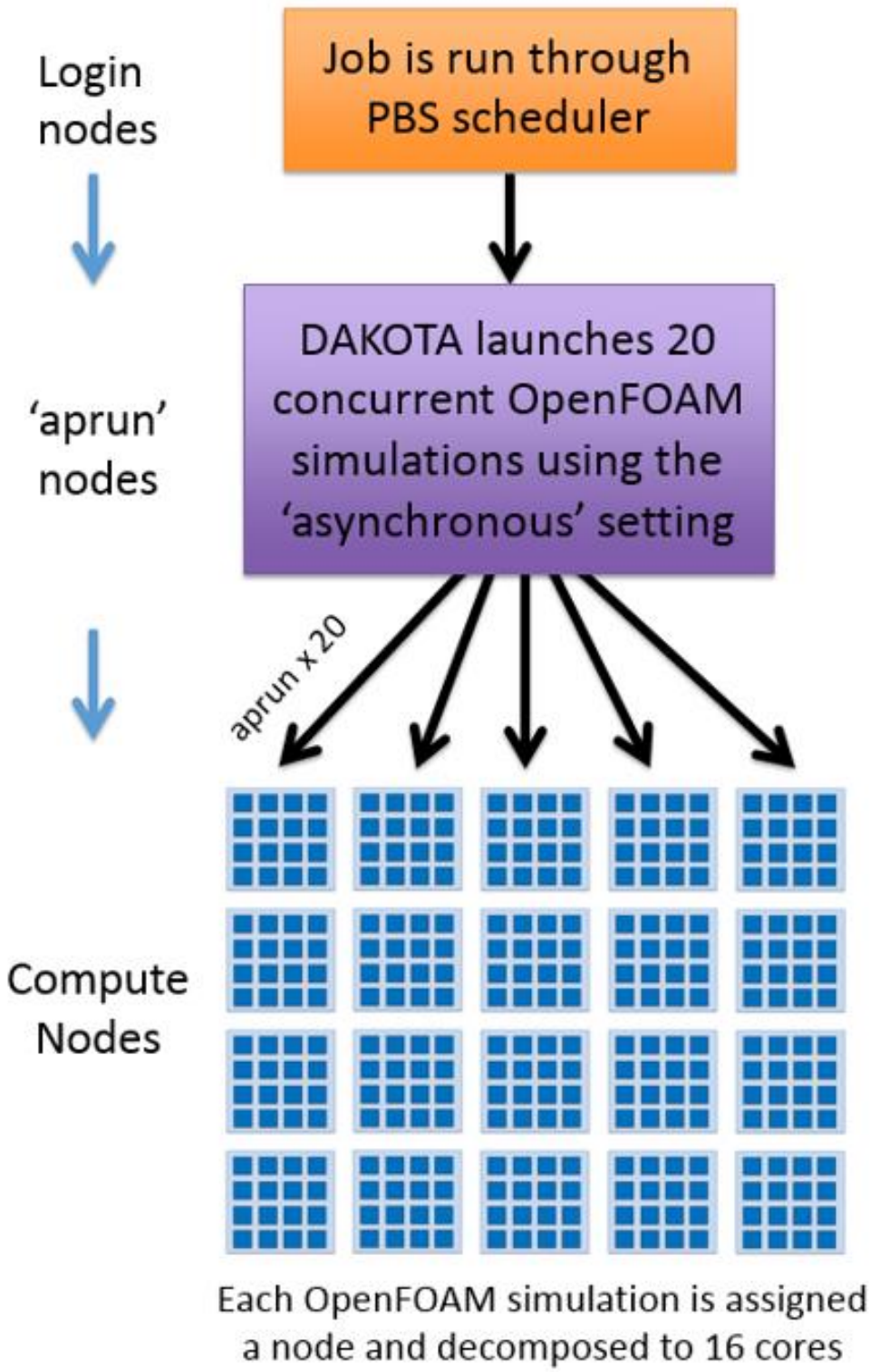

Figure 3.14 Schematic of the parallel organization used to run DAKOTA and OpenFOAM on the Darter supercomputer, utilizing 20 compute nodes.

3.4 Experimental Validation

3.4.1 Water and India Ink Demonstration

As an initial validation of the computational model, and of the models presented in previous studies, a water and ink test setup was implemented to visualize the streamlines of water flowing through a commercial catheter. The silicone catheter used in the demonstration features a design and hole configuration which is available for clinical use: it has 4 rows of inlet holes, each containing 5 holes, in a staggered configuration around the catheter. The catheter was suspended in a beaker of water, with the tip facing downward. The outlet of the catheter was connected to a peristaltic pump, set at a constant average flow rate. India ink, a water-based ink often used in artistic pens, was injected into the flow stream near the catheter tip. Figure 3.15 below shows the bench test setup.

The pump was set to a high average flow rate of about 75 mL/min. This high flow rate, more than 200 times higher than the physiological CSF flow rate of 0.35 mL/min, was necessary in order to create the visualization. A slower pump setting would have allowed the ink enough time to settle to the bottom of the beaker or to dissolve into the surrounding water. Therefore, the results of the demonstration cannot be directly compared to results seen in the computational model. This higher velocity flow can, however, demonstrate the kind of flow field seen at the time of a shunt valve opening. During such opening events, the high pressure buildup at the ventricular end of the shunt creates a driving force that could certainly cause fluid in the catheter region to reach flow rates of up to 10 - 20 mL/min. Such flows in-vivo would exhibit a flow regime similar in magnitude to the one observed in this demonstration.

Figure 3.15 Water and India ink demonstration setup.

3.4.2 Nuclear Imaging Test Using PEPT

As another method to visualize flow through a ventricular catheter, the nuclear imaging technique of positron emission particle tracking (PEPT) was utilized as an additional in-vitro bench test. A photograph of the test setup can be seen in Figure 3.16. PEPT is performed in a positron emission tomography (PET) scanner, a machine often used clinically to create medical images of soft tissues such as cardiac tissue, neural tissue, and even cancerous tumors. The subject is injected with a radionuclide tracer and placed within the scanner's horizontal bore. The tracer emits positrons which, upon collision with electrons in the near vicinity, are annihilated and create two coincident 511 keV gamma rays. These gamma rays are detected by sensors in the bore and can be used to construct three-dimensional images of radionuclide concentration in the subject. PEPT can be similarly used to image fluids into which tracer-laden particles have been introduced [115, 116]. Processing the raw data produces time series images of relative particle positions in the fluid, which can then be used to construct an approximation of the fluid velocity field. The machine used in this test was the Inveon® preclinical PET scanner (Siemens Medical Solutions).

In this experiment, a scaled-up version of a standard 32-hole catheter with a parallel 4-row configuration was used. Scaling the catheter was necessary in this case, as the resolution of the scanner would not have been sufficient to image the flow to the inlet holes of a commercial catheter, which are on the scale of less than 1 mm. A rigid catheter was machined out of clear plastic (PETG) tubing with inner diameter 0.25" (approximately 4.5 times larger than a commercial catheter). The

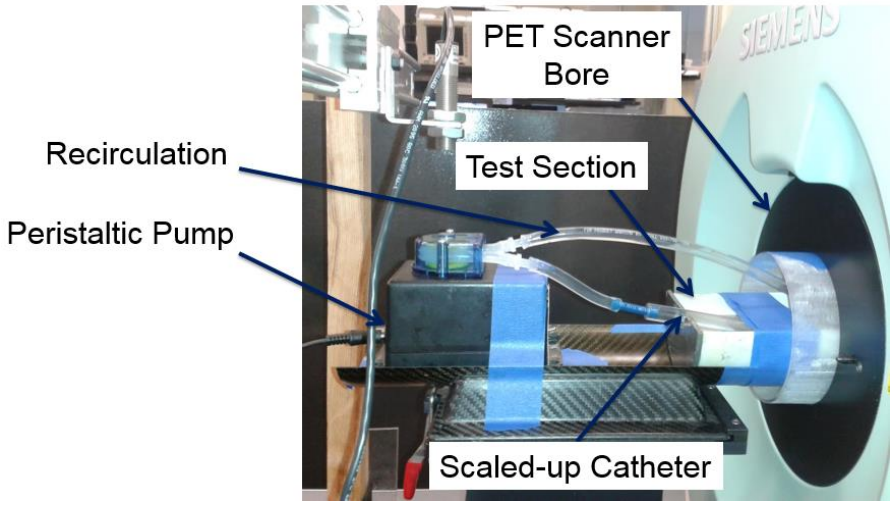

Figure 3.16 Photo of the test section and catheter in the bore, connected to the peristaltic pump.

other dimensions of the model catheter were all similarly scaled. Tapering of the inlet holes was not modeled – all were straight bores of approximately 4.5 mm diameter. With inlet holes of this size, the goal of the test was to track the fluid velocity at the entry to the holes and then to compare these inlet flow rates to those observed in the computational simulations. A schematic of the scaled catheter in the test section within the scanner bore may be seen in Figure 3.17.

In order to achieve such a comparison, with an enlarged catheter model, the flow regime also had to be scaled appropriately to mimic the flow seen in the computational model using Reynold's scaling principles. The Reynold's number of flow in a tube or pipe, like the catheter, is defined by the following equation:

$$Re = \frac{Qd}{\nu A}$$

where Re is the dimensionless Reynold's number, Q is the volumetric flow rate, d is the tube diameter, ν is the kinematic viscosity of the fluid, and A is the cross-sectional area of the tube. The Reynold's scaling principle allows the flow properties of a fluid domain to be analyzed using a scaled model, as long as the Reynold's number is maintained constant between the models. Since the geometric dimensions in this case had to be scaled up, causing a decrease in the ratio of d to A, the ratio of Q to ν had to be increased proportionally in order to keep the Reynold's number the same. The full calculation of the Reynold's scaling for the catheter model and fluid is presented in Appendix A-1 Reynold's Scaling Calculation for Nuclear Imaging Test.

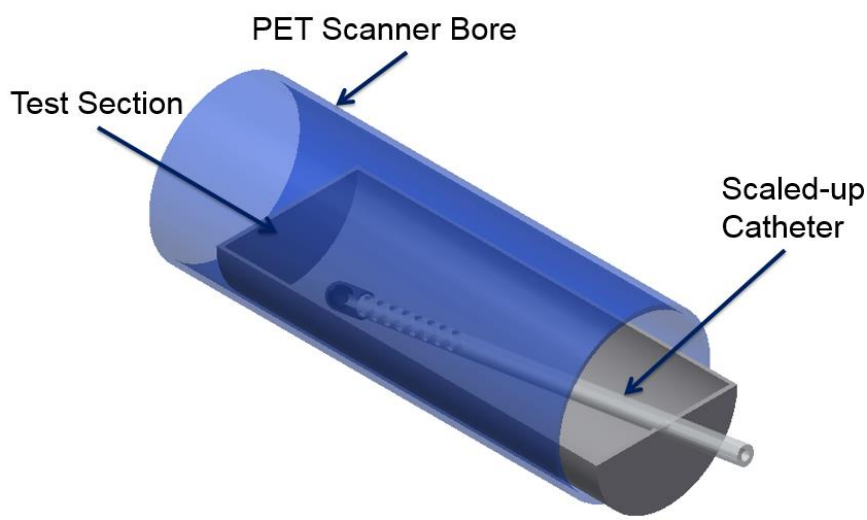

Figure 3.17 Schematic of the scaled catheter in the test section within the scanner bore

The viscosity ν of the fluid in the test had to meet another condition as well, due to the requirement that the particles used to carry the radionuclide tracer would be neutrally buoyant in the surrounding fluid. This buoyancy requirement was necessary so that the particles would indeed follow the trajectory of the fluid as accurately as possible. The particles used were hollow, spherical anion exchange resin beads with a mean diameter of about 75 microns. Though the beads absorb the fluid in which they are immersed, allowing for partial density matching, they still eventually sink in pure water. Therefore, in order to meet the requirement, the density of the fluid was increased by adding sucrose to the water. The solution was brought to approximately 37.5% sucrose to water by mass, and allowed to fully dissolve, increasing the density to 1.165 g/cc and the viscosity by a factor of 14.45.

The flow rate Q was again dictated by the flow rate of the peristaltic pump. For any appreciable movement to be detected visually in the fluid, the maximum pump setting of about 75 mL/min was again used. The flow rate was measured several times, averaged, and recorded as 76.2 mL/min or 1.27 mL/s. Because the flow rate was dictated by the pump, an adjustment was made to the computational flow rate in order to continue to meet the Reynold's scaling requirement. Therefore, the outlet velocity in the CFD simulation was increased from 0.0033 m/s to 0.01175 m/s. This increase in velocity, by a factor of about 3.5, did not significantly affect the simulated flow profile, with an average of less than 10% difference in the calculated relative flow rates. Accordingly, the experiment could still be used to effectively compare catheter performance statistics with the computational model, such as percent flow rate at a given hole.

The scaled catheter was placed in an open-top test section specifically machined to fit the PET scanner bore (see Figure 3.17). Approximately 650 mL of the sucrose solution was poured into the test section and the pump was initialized to prime the fluid into all of the test section tubing. A tube for recirculation of the fluid was also inserted so that the fluid level would not decrease during the test and so that the number of particles in the fluid would remain constant. As the flow rates were still relatively slow, this recirculation did not significantly impact the flow in the area of interest around the catheter inlet holes.

After testing for density matching, the resin beads were activated with the radionuclide tracer, fluorine-18 (F-18). Approximately 200 of these particles, containing a total of around 2 millicuries of radioactivity, were injected via pipette into the fluid of the test section. These activated particles were circulated through the catheter and back into the test section by the pump, while the scanner acquired data about their relative positions in the bore. Twenty consecutive tests of 5 minutes each were conducted in such a fashion, and the fluid was stirred manually after each test to assure that the particles remained continuously buoyant and well

mixed in the fluid. The number and length of tests reflected a desire to have as many particle “traces” or trajectories recorded as possible, so that any post-test analysis would contain statistically significant data. However, due to radioactive decay, the particle tracking was no longer effective after the seventh such test; this only became clear after post-processing of the acquired data. The declining levels of radioactivity can be seen in Figure 3.18, which shows the number of lines of response (LORs), proportional to the positron detections by the PET scanner over the course of the test. During the first run, there was a problem with data acquisition, so the data for this run is missing in this plot. After the fifth test, approximately 50 additional particles were injected into the fluid to attempt to counteract this decline in activity, a known issue from previous tests. However, this attempt did not meaningfully improve the data gathered from subsequent tests.

With the usable raw data gathered from the tests, a collection of approximately 1600 particle traces was constructed using a C++ code to post-process the crystal readings acquired by the PET scanner. These traces consisted x,y,z position data documenting the movements of single particles, sometimes heavily fragmented so that a single particle’s trajectory was mapped by several “piecewise continuous” traces. This data was further processed by a MATLAB code that calculated the velocities along the trace data and averaged these velocities within the elements of a grid to form an approximation of the average velocities at various locations in the test section fluid domain. The coarser the grid used, the more velocities were included in the average velocity calculation for the various locations.

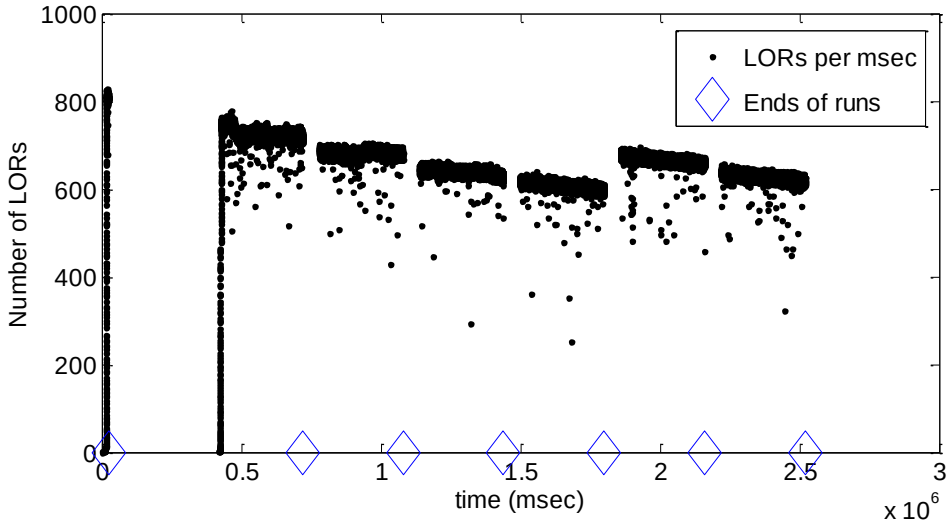

Figure 3.18 Plot of the number of lines of response (LORs) per millisecond, proportional to the positron detections by the PET scanner, over the course of the test.

CHAPTER 4:
RESULTS AND DISCUSSION

4.1 Overview

The results of both the computational and experimental tests are presented in the following sections. Some of the baseline results of the 2D and 3D CFD model can be found in Figure 3.5, in Section 3.2.3. The 3D model in OpenFOAM served as the base case for the iterative studies using DAKOTA. The results presented from these DAKOTA runs represent the sequence in which optimization was achieved. Some of these analyses were achieved on the single Dell workstation and a portion were performed on the Darter supercomputer (see Section 3.1.1).

First, one-at-a-time parameter sensitivity studies are shown, and their conclusions discussed. Then, some of the more influential LHS study results are discussed, though these are summarized, as they represent thousands of individual runs. The subsequent selections for optimization initial points are also presented. Finally, the results of two of the local, derivative-free optimization methods are shown, and a summary of their “winning” parameters is given. These results constitute the best simulated catheter designs for attaining flow rate uniformity among the catheter inlet holes. A significant improvement in uniformity was achieved compared to currently existing designs.

Experimental validation of the computational model was demonstrated in two parts: a qualitative, visual water and ink study and a quantitative nuclear imaging study using PEPT. The results of both tests indicate that in current catheter designs featuring uniform hole diameters and spacing, the majority of the flow enters through the proximal hole set. This can be seen visually in the water and ink demonstration, as most of the injected ink is clearly routed to the holes furthest from the catheter tip. It can also be seen in the velocity field plot produced by the PEPT test. Though the latter test is performed with a scaled-up catheter and fluid domain, it is shown to be a good representation of the flow behavior in an unscaled catheter. Additionally, the results of this test, when compared to an OpenFOAM model of the scaled parameters, show a remarkably accurate reproduction of the experimental data.

With these results, it is evident that there is significant value in using computational fluid dynamics modelling and an iterative framework to optimize the design of ventricular catheters. This framework can be used by both researchers and commercial shunt manufacturers to improve the fluid performance of existing designs, and can be validated by experimental testing of scaled prototypes.

4.2 Parameter Study and Optimization Results

4.2.1 Parameter Sensitivity Studies

In order to identify the most critical parameters of interest to be tested for design optimization, it was necessary to perform one-at-a-time parameter sensitivity studies. In each test, only the parameter of interest was varied while the others were held constant. This allowed for each parameter to be tested independently of the others, and its effect on the objective function to be isolated and analyzed with regard to the magnitude of the effects. Parameters of interest (see Figure 3.12) tested using this method were as follows:

- linear factors for increasing/decreasing inner hole diameters and hole spacing, multiplied over each hole segment, with the hole closest to the tip (hole 1), serving as the initial value
- hole diameter and hole spacing between holes 1 and 2
- distance from the catheter tip to hole 1
- degree of tapering of the inlet holes
- catheter wall thickness

Next, a value called the sensitivity index was calculated, using the following formula: $SI = 1 - F_{min}/F_{max}$, in which SI is the sensitivity index, F_{max} is the maximum value of the objective function, and F_{min} is the minimum value of the objective function. This type of sensitivity study has been used in past studies [117, 118], when comparing parameters that have different ranges and possibly different units, as is the case with degree of hole tapering. The results of the studies take the form of 2D plots (Figure 4.1), with the parameter of interest as the independent variable and the objective function as the dependent variable. The ranges and sensitivity indices are shown in Table 4.1.

Table 4.1 Ranges and Sensitivity Indices of Parameters of Interest

Parameter	Parameter Range		Sensitivity Index
	Minimum	Maximum	
Linear factor for inner hole diameters	0.825	1.025	0.9538
Diameter for hole 1 [mm]	0.50	1.00	0.9107
Linear factor for hole spacing	0.95	1.15	0.4693
Spacing between holes 1 and 2 [mm]	1.00	2.00	0.8194
Degree of tapering of the inlet holes [°]	0.00	19.28	0.8335
Catheter wall thickness [mm]	0.30	0.70	0.5246
Distance from the catheter tip to hole 1 [mm]	1.00	4.50	0.0003

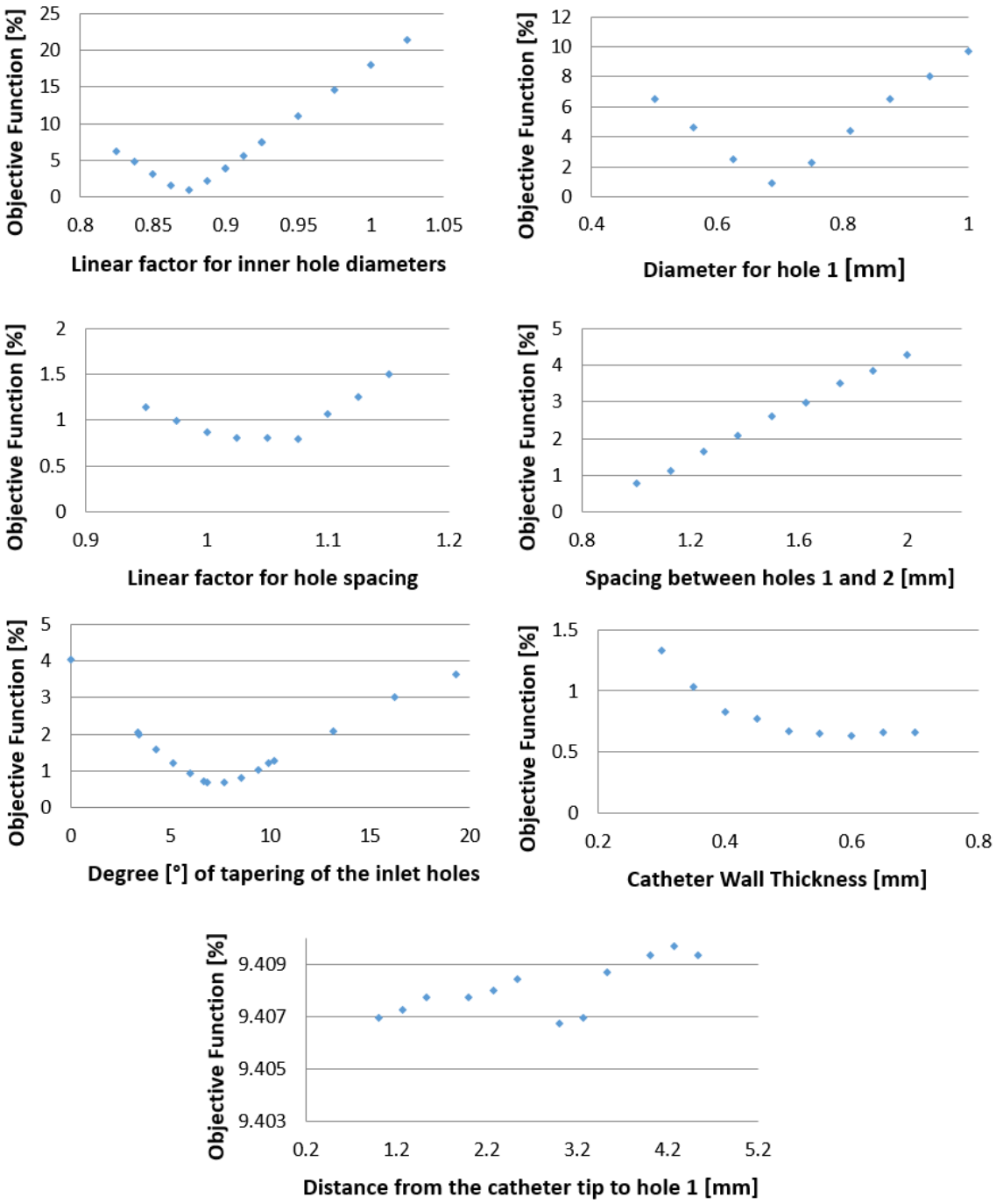

Figure 4.1 Parameter sensitivity study results, showing 2D plots with the parameter of interest as the independent variable and the objective function as the dependent variable.

The sensitivity studies provided crucial guidance for selecting the parameters that most affect the objective function and selecting the most influential ranges for those variables. The results shown are from analyses performed on a catheter design featuring 6 holes, as were the subsequent iterative analyses. When similar tests were conducted for 4 and 8 hole designs, the conclusions about the parameter of interest were similar. The principle conclusions were as follows:

- The parameter representing the distance from the catheter tip to hole 1 was the least influential, with a sensitivity index several scales of magnitude less than those of the other parameters.
- The diameters of the holes are the most influential parameters; both the diameter of the first hole and subsequent applications of a linear factor to the remaining holes caused significant changes in the objective function.
- Linear scaling factors of less than 1 for the hole diameters produced favorable objective functions, confirming past studies showing that designs featuring decreasing hole diameters improve flow rate uniformity.
- Surprisingly, linear factors between 1 – 1.1 showed the most promise with regards to hole spacing, indicating that increasing spaces between the holes would produce favorable results. However, the sensitivity index for this parameter was relatively low, so its influence was not very substantial.
- Degree of hole tapering was quite influential, and though this parameter is not easily modified in catheter manufacturing, it is apparent that some tapering (between 5 - 10 degrees) of the holes is actually beneficial in terms of improving flow rate uniformity.
- Wall thickness was less influential, but lower objective function values were observed for thicker catheter walls.

These conclusions provided a basis for excluding certain parameters from more detailed investigation. A standard distance from the catheter tip to hole 1 was selected as 1.2 mm, since this parameter proved the least influential. Moderately influential factors, such as degree of hole tapering and wall thickness were tested with only 1 or 2 values. For degree of hole tapering, these were around the minimum value of 7.5 degrees. For wall thickness, standard thicknesses of extruded silicone tubing of 0.5 mm or 0.6 mm were tested. Since the material properties of the catheter (flexibility, structural integrity) depend on this factor, it was important not to test significantly thicker or thinner catheters as these may not be viable for use in-vivo. With these parameters limited (or set), the remaining parameters were carried forward for further testing.

4.2.2 Latin Hypercube Sampling (LHS) Results

After performing the sensitivity studies, 4 parameters of interest were identified for further testing: linear factor for increasing/decreasing inner hole diameters, linear factor for hole spacing, hole 1 diameter, and hole spacing between holes 1 and 2. However, the sensitivity studies only provided an initial understanding of these parameters and their effects on the objective function. As for the linear factors, they only showed limited behavior for certain increasing or decreasing hole configuration parameters. In order to avoid the restriction of testing linear patterns only, it was necessary to test individual diameter and spacing parameters. This greatly increases the number of dimensions of the parameter space. Therefore, as explained in Section 3.3.4, a Latin Hypercube Sampling method was utilized to explore the parameter space at a general level and to detect further trends in the objective function.

The advantage of this method was the uniform coverage over the entirety of the parameter space (see Figure 3.13). One method to visualize the results of such a test is by creating a parallel coordinates plot, as shown in Figure 4.2. The coverage of a 5-dimensional space can be seen again here and in the 2D contour plots shown in Figure 4.3 on the following page. Both show an LHS run of 1000 function evaluations on a limited parameter space of only 5 dimensions – in this

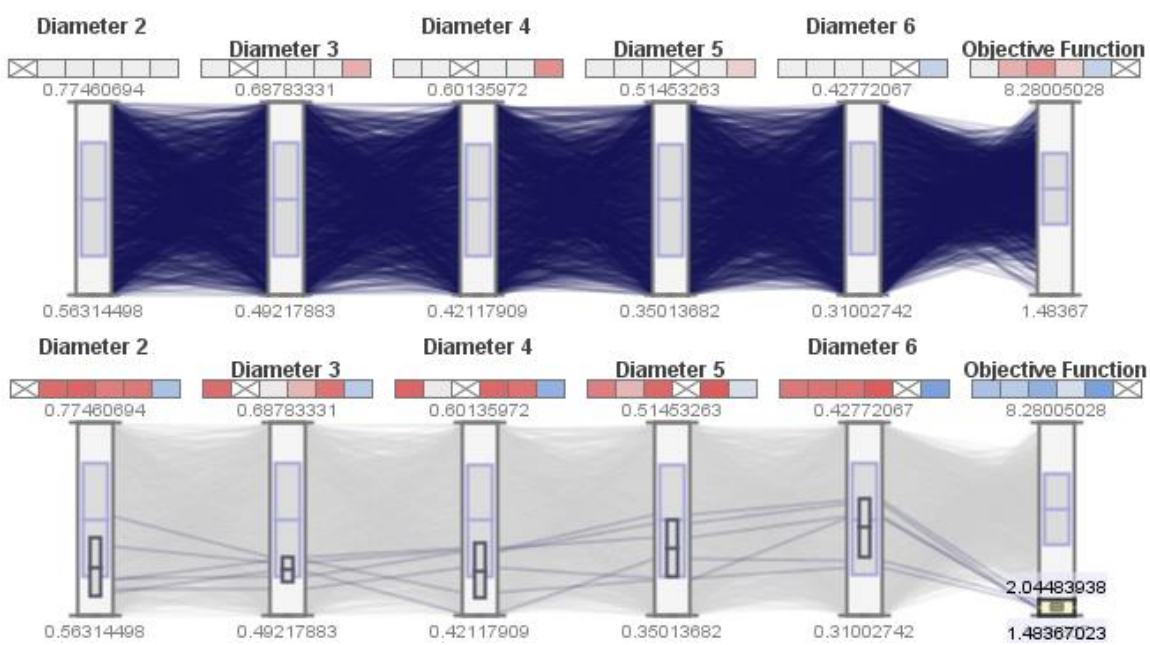

Figure 4.2 Parallel coordinate plot of LHS results on a 5-dimensional parameter space of hole diameters 2-6. *Top*: all 1000 runs. *Bottom*: 6 most successful runs.

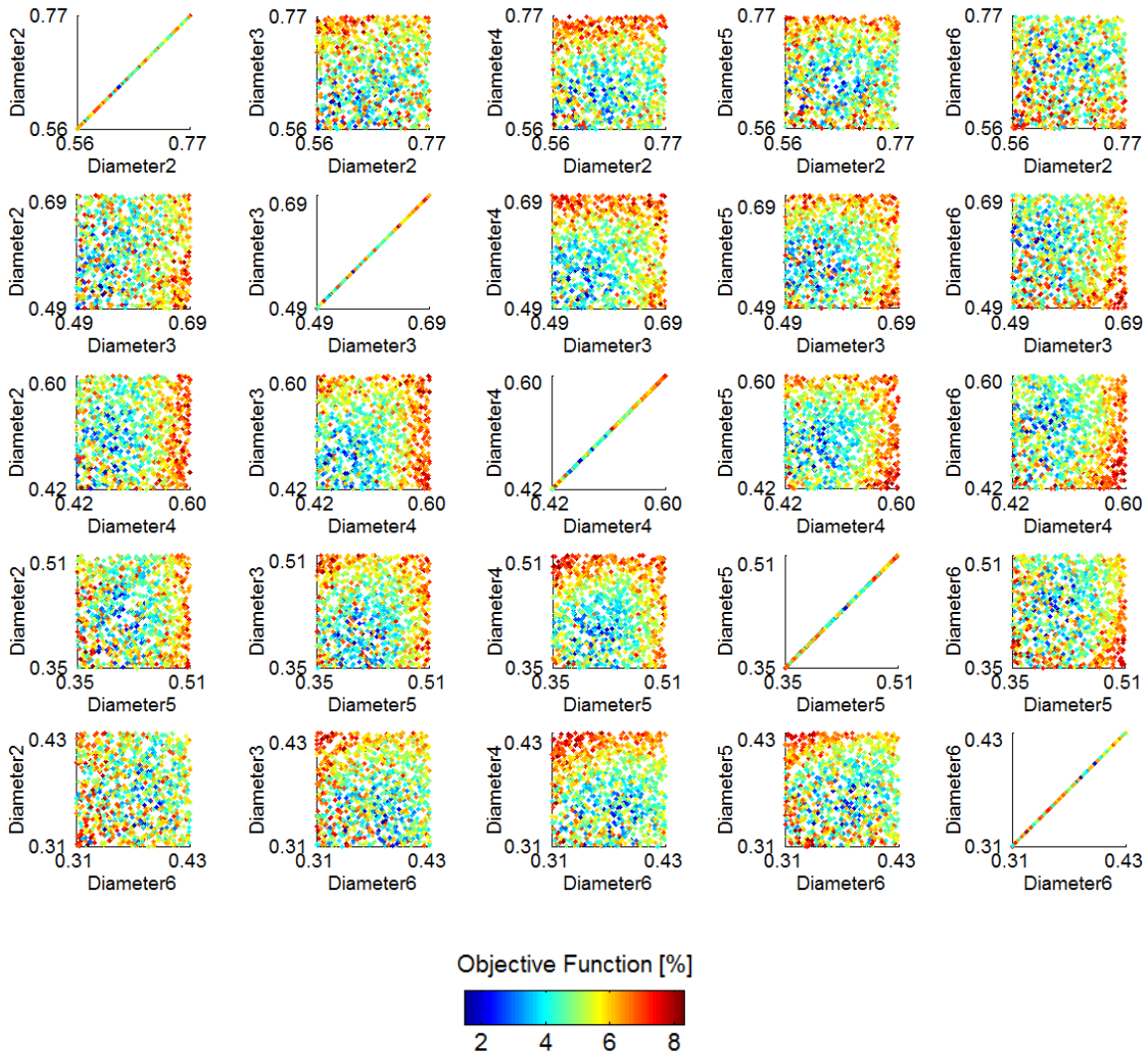

Figure 4.3 LHS results shown as 2D colored scatter plots of parameter pairs in a 5-dimensional parameter space of hole diameters 2-6.

case testing the objective function response to changing hole diameters 2-6, while hole diameter 1 and the other parameters are held constant. Parallel coordinates is a convenient way to visualize the different parameter combinations. This plot (Figure 4.2) was created using EDEN, a visual analytics tool for exploring quantitative multivariate data developed at Oak Ridge National Laboratory [119]. Each line across the 5 parameters represents one parameter combination and its resulting objective function. The 5 x 5 2D plot array (Figure 4.3) shows the same data as colored scatter plots, so that colors can be used to identify trends in the objective function. Both visual techniques were helpful for analyzing the thousands of LHS results. The colored scatter ("contour") plots specifically gave helpful data on the response function. For example, combinations with a pairing of low values for both diameter 3 and diameter 4 show an area of low objective functions, so this is a design consideration that may be favorable to take into account.

The main disadvantage, which is most apparent in the parallel coordinates representation, was a lack of repeated parametric patterns in areas of interest. Only 5 out of 1000 runs showed objective function results under 2%, the area of interest. The other 995 runs only play a supportive role, but are eventually of minimal interest. This disadvantage was a result of the independent nature of the runs in LHS method: all parameter sets are established at the outset of the analysis and therefore, the method has no ability to focus on any region after discovering areas of objective function minimization. This meant that the results had to be analyzed "manually" by the user. Nevertheless, the LHS runs allowed for a broader view of the parameter space, especially of individual hole diameters and hole spacing values. These runs, along with the sensitivity studies, showed "slices" of the parameter space and objective function response behavior. By focusing parameter ranges and performing subsequent runs, the objective function was minimized to 0.67%. The best runs from these pre-optimization explorations provided good candidates to use as initial points in the next stage of optimization.

4.2.3 Optimization Results

After completing the pre-optimization exploration of the parameter space, as described in the two previous sections, the most promising catheter design parameter sets were used as initial points for running an optimization routine using the coliny pattern search method (local, derivative-free), as explained in Section 3.3.4. The high-fidelity OpenFOAM simulation results of the most successful of these optimization analyses is shown in Figure 4.4 on the following page, along with the optimized parameter set. Each analysis ran for approximately 400-500 function evaluations before reaching convergence to a specific set of

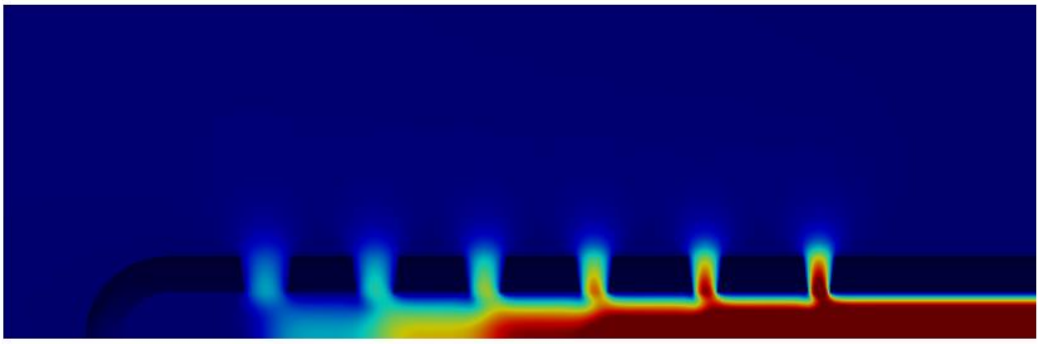

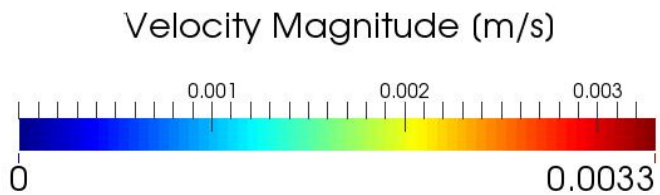

Catheter Inner Diameter	1.50 mm
Wall Thickness	0.60 mm
Degree of Hole Tapering	7.688°
Total Length of Perforated Segment	10.495 mm

Interior Hole Diameters [mm]	Exterior Hole Diameters [mm]	Hole Spacing Distance [mm]
ID 1 = 0.6876	OD 1 = 0.8496	SP 1 = 1.2000
ID 2 = 0.6112	OD 2 = 0.7732	SP 2 = 1.0000
ID 3 = 0.5254	OD 3 = 0.6874	SP 3 = 1.0750
ID 4 = 0.4560	OD 4 = 0.6180	SP 4 = 1.1556
ID 5 = 0.4030	OD 5 = 0.5650	SP 5 = 1.2423
ID 6 = 0.3616	OD 6 = 0.5236	SP 6 = 1.3355

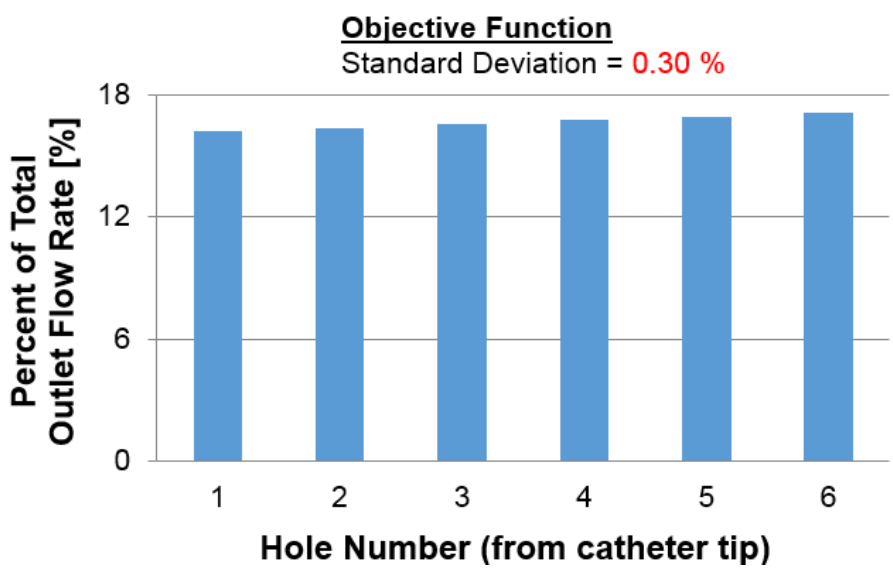

Figure 4.4 Optimized design results. *Top*: CFD results from high-fidelity OpenFOAM simulation. *Mid*: Parameter values for optimized design. *Bottom*: Graph showing relative flow rate distribution among inlet holes, with minimized objective function at 0.30%.

parameters. The maximum number of function evaluations was set to 1000 and was not reached during the analyses, indicating that the optimization algorithm indeed identified minimizing sets of parameters.

This optimization method was found to be satisfactory in the identification of minima in the response function, when given a favorable initial point. Derivative-based methods that were attempted did not prove similarly effective for this problem, as they would not converge, even after hundreds of runs. This is perhaps a further indication of the non-smooth, perhaps non-continuous nature of the objective function in this problem. Nevertheless, as the optimization method chosen was a local method, the identification of favorable initial points prior to the execution of the optimization analysis was a critical step. The results of the design optimization demonstrated a drastic improvement over the “standard” catheter, with uniform hole diameters and spacing. The standard design had a computed objective function of 14.27% (see Figure 3.5), an obviously flawed flow profile compared to the optimized result of 0.30%, which demonstrates nearly complete uniformity of flow rates between the inlet holes.

4.3 Experimental Results

The experimental portion of the research was used as a means by which to validate the fluid flow behavior in ventricular catheters, which was observed in previous studies and throughout the computational simulations in this current research. The designs of interest for this validation were those of most current commercial catheters, specifically designs featuring uniform inlet hole diameters and uniform hole spacing. These were taken as the standard for this testing for two main reasons:

1. These are the catheter designs that are currently most likely to be implanted in individuals requiring a CSF shunt.
2. The anticipated “skewed” flow rate distribution profile among the inlet holes of such a design was the one most likely to be identifiable with the flow measurement techniques used. Using a pump at a very slow flow rate, if the majority of the flow volume goes through the inlet holes furthest from the catheter tip, there is a high chance of being able to visually see this pattern and to possibly quantify this majority flow rate.

The first test was a water and India ink demonstration, which allowed for an initial visual confirmation of flow behavior in such a commercial catheter design. This was an important confirmation to do before going on to use the more quantitative fluid imaging technique PEPT and using highly sophisticated and costly testing equipment.

4.3.1 Water and India Ink Demonstration

Utilizing the bench test setup described in Section 3.4.1, several water and ink demonstrations were conducted. The results in the figures below show a clear preference for the ink to flow toward the holes furthest from the tip. Images were retrieved at 1 second intervals from video footage of the demonstrations. The holes closest to the tip saw little to no visible flow that was stained by the ink. The catheter pictured in Figure 4.5 (left) is the 5-hole per row catheter described in Section 3.4.1.

The 5-hole design generally produced the most visually viable results due to the larger inlet holes. An 8-hole design was used to provide a comparison and can be seen in Figure 4.5 (right). Both demonstrations exhibit the same flow behavior, but the smaller and greater number of holes in the 8-hole design prevented the flow into the holes from being as visually obvious as that of the 5-hole design. The 8-hole design divides the total flow rate between 32 holes, allowing each hole a smaller portion of the flow, while the 5-hole design only divides the flow between 20 holes.

The high flow rate applied proved necessary for the visualization of the flow. Lower pump settings were used initially and were not able to adequately pull the ink toward the holes, allowing the ambient convective flow of the water disperse the ink before it could reach the inlet holes. Although the high flow rate does not mimic physiological flow, it can be representative of flow during a valve opening event. Even at such high flow rates, during which the flow regime is no longer strictly laminar, the majority of the flow was still confined to the holes farthest from the tip. This may indicate that even turbulence in the catheter does not promote flow entering holes closest to the tip, though this hypothesis would require further testing and validation.

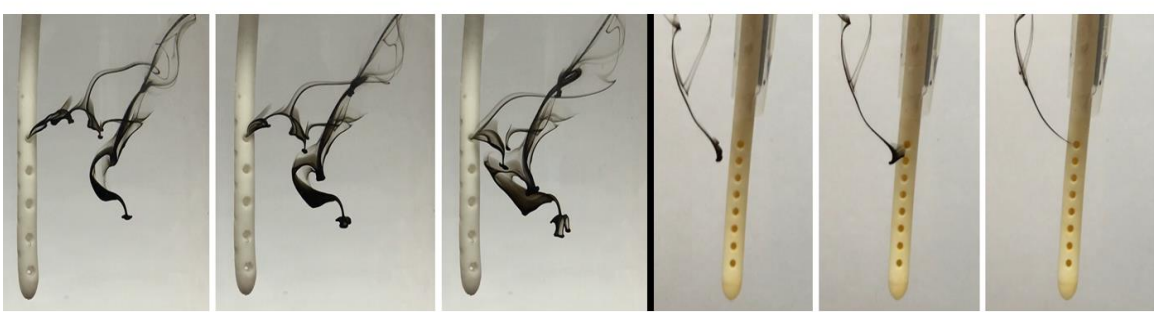

Figure 4.5 Water and India ink demonstrations. Images are taken at 1 second intervals. *Left*: Using a 5-hole per row catheter design. *Right*: Using a 8-hole per row catheter design.

4.3.2 Nuclear Imaging Test Using PEPT

From the over 1600 reconstructed particle traces, a MATLAB code calculated the velocities along the trace data and averaged these velocities within the elements of a grid to form an approximation of the average velocities at various locations in the test section fluid domain. As stated previously, the coarser the grid used, the more velocities were included in the average velocity calculation for the various locations. An example of such a velocity plot may be seen in Figure 4.6 on the following page, featuring a 1 mm x 1 mm grid. An outline of the catheter's location is overlaid on the velocity plot.

Many of the grid areas are only sparsely populated with recorded velocities, and even those areas with relatively more densely populated velocities are only averaged from the data of no more than about 20-25 traces. Though this assessment reduces the statistical robustness of the velocity results, they nevertheless form a coherent pattern which can be visually compared to results of the CFD model of the experiment (using scaled-up geometry and sucrose solution fluid properties). Such a comparison can be seen in Figure 4.7 on page 73. If the average inlet face velocities at the set of holes farthest from the catheter tip are estimated visually, they would appear to fall in the 0.020 - 0.025 m/s range. Similarly, those velocities in the CFD simulation of the experimental model visually appear to fall in approximately the same range, and are calculated to have an average velocity of 0.01925 m/s.

This would suggest that the CFD simulations are a comparatively accurate source of flow data, when observed in conjunction with experimental flow data. Though both models feature rigid catheters and constant flow rates, conditions which are not necessarily found in-vivo, they do represent a strong basis by which to evaluate the flow profiles of different catheter designs for comparative purposes. Moreover, when the scaled-up results are compared to CFD results of an unscaled catheter in water, the percent of fluid entering the proximal hole set is again very similar. From the experimental results and CFD model of the experiment, the relative flow rate percentage at this hole set is calculated to be approximately 57% and in the case of the unscaled catheter, it is calculated as 56.06%.

Therefore, when the objective is to compare relative flow rate profiles of different designs, it is again apparent that the CFD simulation is an accurate representation of realistic catheter flow. In future catheter engineering, this type of imaging can be helpful as various designs can be modeled and prototyped using larger, easier to fabricate dimensions by employing advanced techniques such as additive manufacturing (3D printing) or basic ones such as the machining used for this series of tests.

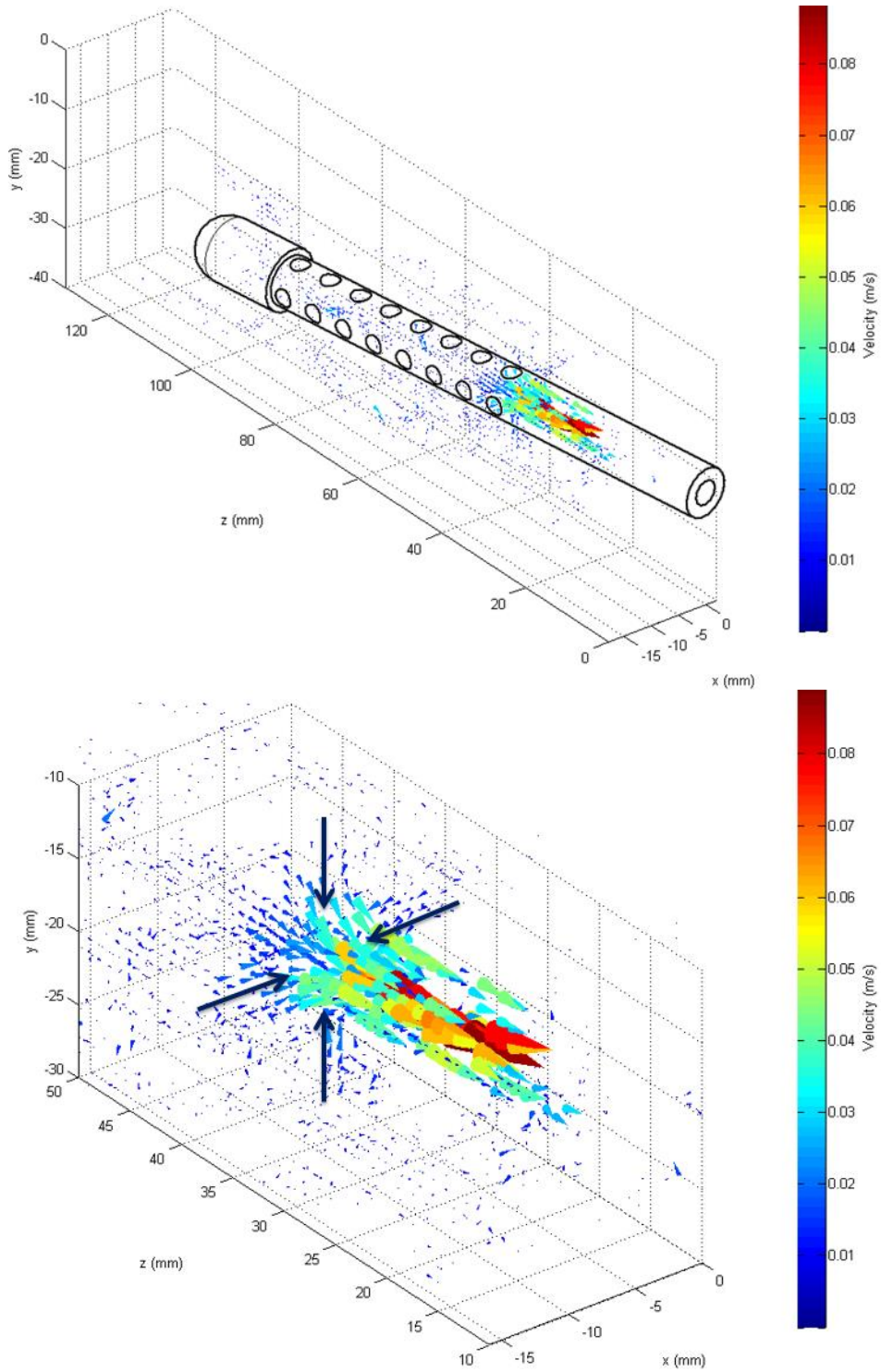

Figure 4.6 *Top*: Plot of the averaged particle velocity, computed based on a 1 mm x 1 mm grid. Catheter shape is overlayed. *Bottom*: Close-up of proximal hole set region with arrows indicating the influx of particles through the inlet holes.

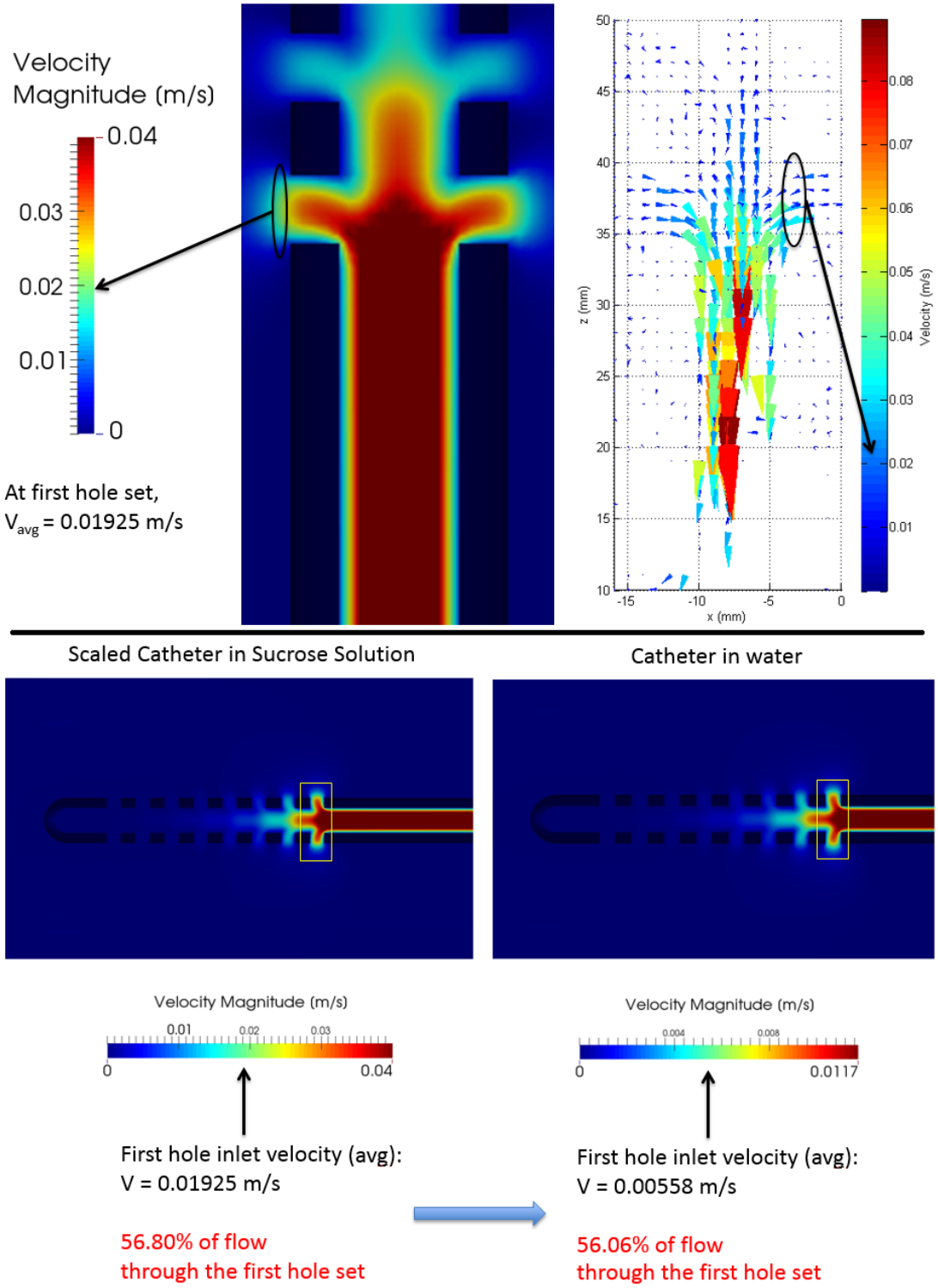

Figure 4.7 *Top*: Comparison of results for the scaled OpenFOAM simulation (left) and averaged experimental particle velocity (right). Catheter shape is overlayed. *Bottom*: Comparison of results for scaled and unscaled OpenFOAM simulations.

CHAPTER 5:
CONCLUSIONS AND RECOMMENDATIONS

In this research work, computational and experimental models of flow through a ventricular catheter were explored and used to improve catheter design. A three-dimensional computational fluid dynamics model was developed and served as a basis for an automated simulation framework, which in turn was used to identify an optimized catheter design, providing high uniformity of relative flow rates among the catheter's inlet holes. The computational models were run on both a single workstation and on a high-performance supercomputer, serving as a proof-of-concept that such an optimization framework can be utilized in both commercial and research settings. Furthermore, by coupling two open-source software toolkits, OpenFOAM and DAKOTA, it was shown that such a framework can be built with free, user-supported software, making it a cost-effective means of improving engineered medical device designs.

The results shown in this study provide guidelines for those involved in the engineering of ventricular catheters, and they provide at least one optimized design suggestion to improve the inlet flow profile of standard 4-hole per row, parallel row designs. The CFD model used in this work can easily be adapted for other numbers of holes per row, but is limited to parallel-row designs. Staggered row designs, which are also popular among the leading catheter manufacturers, would require modification of the pre-processing script used to generate the fluid domain and mesh for each simulation. However, as a complementary extension of this thesis, optimizing the staggered row design would be beneficial and should be part of the future efforts of researchers in this field.

The CFD model itself could also be modified to include features that bring it closer to the real in-vivo performance of a catheter draining CSF from a ventricle. Most importantly, the steady-state aspect of the simulations used in this thesis do not take into account the transient nature of flow induced by the opening of normally closed differential pressure valves, which are used in the majority of most shunt systems. Unfortunately, statistics about this transient behavior – specifically transient flow rates at the time of valve opening – are not described in the literature made available to the public by shunt manufacturers. In order to more accurately analyze the influence of catheter fluid dynamics on catheter obstruction rates, the instantaneous opening flow rates should be experimentally determined for the various valve and shunt designs. Valveless shunts, though not as heavily marketed, may provide flow with a steady state nature, but these should be acquired and tested alongside valved shunts.

In terms of the optimization strategy outlined in this thesis, the pre-optimization methods used to locate favorable initial points for optimization may be taken further to locate additional favorable points within the design space and possible in other design spaces. These points can serve as a strong basis for a more comprehensive multi-start local optimization algorithm. Using such a method, a user could hone in on parameter combinations that minimize the objective function even further. There also exist additional objective functions that could be explored using the framework outlined in this thesis. One important example is the minimization of wall shear stress in and around the catheter inlet holes. In one study [84], increases in wall shear stress have been correlated to the incidence of cellular adhesion on the catheter walls and could therefore also be tied to the incidence of obstruction.

Another possible optimization method, not attempted in this work but certainly achievable with the computational resources available, is to create a surrogate model of the objective function response curve. A surrogate is essentially a best-fit estimation of the response function, and can replace costly full evaluations of the objective function. Surrogate methods are supported in DAKOTA, so it would not be require a large additional time investment to set up such a case and build a surrogate from a few thousand simulated design points. Then using the surrogate, the design space could be efficiently explored using global optimization methods, or possibly even derivative-based methods. The capabilities of high performance computing systems, which were used on a limited scale in this study, would be critical for developing and rigorously validating the model. However, the surrogate would be so computationally compact that further analyses could easily be done on a single workstation.

Experimental validation of the fluid performance of optimized designs is the next critical step toward making such designs a clinical reality. This thesis provided a proof-of-concept for using the PEPT imaging technique to produce quantitative 3D velocity field approximations for scaled-up models of catheter designs. The results shown in this research work represent an initial attempt to use this method to validate the computational model. However, by perfecting this technique, perhaps by using less particles with higher amounts of radioactivity, the number of viable particle traces can grow significantly. With a high number of particle traces, the statistical characteristics of the estimated velocity field can be improved. Additionally, due to the small size of the particles, it may even be possible to image an unscaled catheter. This would allow for impressive pre-clinical testing of prototypes – the first step toward improving ventricular catheter performance and toward the goal of reducing the rates of revision surgeries required for shunted patients, eventually improving their quality of life.

REFERENCES

[1] (2008). *Hydrocephalus Fact Sheet*. Available online: www.ninds.nih.gov/disorders/hydrocephalus/detail_hydrocephalus.htm

[2] J. H. Chi, H. J. Fullerton, and N. Gupta, "Time trends and demographics of deaths from congenital hydrocephalus in children in the United States: National Center for Health Statistics data, 1979 to 1998," *J Neurosurg,* vol. 103, pp. 113-8, Aug 2005.

[3] T. D. Simon, J. Riva-Cambrin, R. Srivastava, S. L. Bratton, J. M. Dean, and J. R. Kestle, "Hospital care for children with hydrocephalus in the United States: utilization, charges, comorbidities, and deaths," *J Neurosurg Pediatr,* vol. 1, pp. 131-7, Feb 2008.

[4] R. V. Patwardhan and A. Nanda, "Implanted ventricular shunts in the United States: the billion-dollar-a-year cost of hydrocephalus treatment," *Neurosurgery,* vol. 56, pp. 139-44; discussion 144-5, 2005.

[5] Wikipedia. *Cerebrospinal fluid*. Available: http://en.wikipedia.org/wiki/Cerebrospinal_fluid#cite_note-7

[6] J. M. Ling and R. Tiruchelvarayan, "A Review of Endoscopic Treatment of Hydrocephalus in Paediatric and Adult Patients," *Proceedings of Singapore Healthcare,* vol. 22, pp. 203-212, 2013.

[7] P. Spennato, G. Cinalli, C. Ruggiero, F. Aliberti, V. Trischitta, E. Cianciulli*, et al.*, "Neuroendoscopic treatment of multiloculated hydrocephalus in children," *J Neurosurg,* vol. 106, pp. 29-35, Jan 2007.

[8] T. Appelgren, S. Zetterstrand, J. Elfversson, and D. Nilsson, "Long-term outcome after treatment of hydrocephalus in children," *Pediatr Neurosurg,* vol. 46, pp. 221-6, 2010.

[9] J. J. Stone, C. T. Walker, M. Jacobson, V. Phillips, and H. J. Silberstein, "Revision rate of pediatric ventriculoperitoneal shunts after 15 years," *J Neurosurg Pediatr,* vol. 11, pp. 15-9, Jan 2013.

[10] J. M. Drake, J. R. Kestle, R. Milner, G. Cinalli, F. Boop, J. Piatt, Jr.*, et al.*, "Randomized trial of cerebrospinal fluid shunt valve design in pediatric hydrocephalus," *Neurosurgery,* vol. 43, pp. 294-303; discussion 303-5, Aug 1998.

[11] S. Tuli, B. O'Hayon, J. Drake, M. Clarke, and J. Kestle, "Change in ventricular size and effect of ventricular catheter placement in pediatric patients with shunted hydrocephalus," *Neurosurgery,* vol. 45, pp. 1329-33; discussion 1333-5, Dec 1999.

[12] P. Collins, A. D. Hockley, and D. H. Woollam, "Surface ultrastructure of tissues occluding ventricular catheters," *J Neurosurg,* vol. 48, pp. 609-13, Apr 1978.

[13] S. Hakim, "Observations on the physiopathology of the CSF pulse and prevention of ventricular catheter obstruction in valve shunts," *Dev Med Child Neurol Suppl,* vol. 20, pp. 42-8, 1969.

[14] L. N. Sekhar, J. Moossy, and A. Norman Guthkelch, "Malfunctioning ventriculoperitoneal shunts," *Journal of Neurosurgery,* vol. 56, pp. 411-416, 1982.

[15] C. A. Harris and J. P. McAllister, "What We Should Know About the Cellular and Tissue Response Causing Catheter Obstruction in the Treatment of Hydrocephalus," *Neurosurgery,* vol. 70, pp. 1589-1601, Jun 2012.

[16] J. M. Drake, J. R. Kestle, and S. Tuli, "CSF shunts 50 years on--past, present and future," *Childs Nerv Syst,* vol. 16, pp. 800-4, Nov 2000.

[17] B. A. Kaufman and T. S. Park, "Ventricular anatomy and shunt catheters," *Pediatr Neurosurg,* vol. 31, pp. 1-6, Jul 1999.

[18] E. J. Hermann, H. H. Capelle, C. A. Tschan, and J. K. Krauss, "Electromagnetic-guided neuronavigation for safe placement of intraventricular catheters in pediatric neurosurgery Clinical article," *J Neurosurg Pediatr,* vol. 10, pp. 327-333, Oct 2012.

[19] C. G. Janson, L. G. Romanova, K. D. Rudser, and S. J. Haines, "Improvement in clinical outcomes following optimal targeting of brain ventricular catheters with intraoperative imaging," *J Neurosurg,* vol. 120, pp. 684-96, Mar 2014.

[20] C. K. Lee, L. L. Tay, W. H. Ng, I. Ng, and B. T. Ang, "Optimization of ventricular catheter placement via posterior approaches: a virtual reality simulation study," *Surg Neurol,* vol. 70, pp. 274-7; discussion 277-8, Sep 2008.

[21] U. W. Thomale, T. Knitter, A. Schaumann, S. A. Ahmadi, P. Ziegler, M. Schulz*, et al.*, "Smartphone-assisted guide for the placement of ventricular catheters," *Childs Nerv Syst,* vol. 29, pp. 131-139, Jan 2013.

[22] R. Fox and J. Norton, "A novel device for the clearance and prevention of blockages within biomedical catheters," *Medical Engineering & Physics,* vol. 36, pp. 1526-1529, 11// 2014.

[23] L. Hyowon, K. Kolahi, M. Bergsneider, and J. W. Judy, "Mechanical Evaluation of Unobstructing Magnetic Microactuators for Implantable Ventricular Catheters," *Microelectromechanical Systems, Journal of,* vol. 23, pp. 795-802, 2014.

[24] W. A. Christens-Barry, M. Guarnieri, and B. S. Carson, Sr., "Fiberoptic delivery of laser energy to remove occlusions from ventricular shunts: technical report," *Neurosurgery,* vol. 44, pp. 345-9; discussion 349-50, Feb 1999.

[25] C. C. Duncan, "Management of proximal shunt obstruction. Technical note," *J Neurosurg,* vol. 68, pp. 817-9, May 1988.

[26] S. H. Weisenberg, S. C. TerMaath, C. E. Seaver, and J. A. Killeffer, "Ventricular catheter development: past, present, and future," *Journal of neurosurgery,* pp. 1-9, 2016.

[27] J. H. Piatt, Jr. and M. Cosgriff, "Monte Carlo simulation of cerebrospinal fluid shunt failure and definition of instability among shunt-treated patients with hydrocephalus," *J Neurosurg,* vol. 107, pp. 474-8, Dec 2007.

[28] C. Sainte-Rose, J. H. Piatt, D. Renier, A. Pierre-Kahn, J. F. Hirsch, H. J. Hoffman*, et al.*, "Mechanical complications in shunts," *Pediatr Neurosurg,* vol. 17, pp. 2-9, 1991.

[29] K. G. Go, E. J. Ebels, and H. van Woerden, "Experiences with recurring ventricular catheter obstructions," *Clin Neurol Neurosurg,* vol. 83, pp. 47-56, 1981.
[30] J. Kestle, J. Drake, R. Milner, C. Sainte-Rose, G. Cinalli, F. Boop*, et al.*, "Long-term follow-up data from the Shunt Design Trial," *Pediatr Neurosurg,* vol. 33, pp. 230-236, 2000/11// 2000.
[31] G. Zemack and B. Romner, "Seven years of clinical experience with the programmable Codman Hakim valve: a retrospective study of 583 patients," *J Neurosurg,* vol. 92, pp. 941-948, 2000.
[32] B. Borgbjerg, F. Gjerris, M. Albeck, J. Hauerberg, and S. Børgesen, "Frequency and causes of shunt revisions in different cerebrospinal fluid shunt types," *Acta Neurochir (Wien),* vol. 136, pp. 189-194, 1995.
[33] A. Aschoff, P. Kremer, B. Hashemi, and S. Kunze, "The scientific history of hydrocephalus and its treatment," *Neurosurg Rev,* vol. 22, pp. 67-93; discussion 94-5, Oct 1999.
[34] A. Demerdash, R. Singh, M. Loukas, and R. S. Tubbs, "A historical glimpse into treating childhood hydrocephalus," *Childs Nerv Syst,* pp. 1-3, 2015/02/24 2015.
[35] J. M. Drake and C. S. Rose, *The Shunt Book*: Wiley, 1995.
[36] J. I. Lifshutz and W. D. Johnson, "History of hydrocephalus and its treatments," *Neurosurg Focus,* vol. 11, pp. 1-5, 2001.
[37] M. M. Mortazavi, N. Adeeb, C. J. Griessenauer, H. Sheikh, S. Shahidi, R. I. Tubbs*, et al.*, "The ventricular system of the brain: a comprehensive review of its history, anatomy, histology, embryology, and surgical considerations," *Childs Nerv Syst,* vol. 30, pp. 19-35, Jan 2014.
[38] E. Rustamzadeh and C. H. Lam, "Cerebrospinal Fluid Shunts," in *The Bionic Human: Health Promotion for People With Implanted Prosthetic Devices*, ed Totowa, NJ: Humana Press Inc., 2006, pp. 333-358.
[39] J. Lister, "On the Antiseptic Principle in the Practice of Surgery," *Br Med J,* vol. 2, pp. 246-248, 1867.
[40] W. W. Keen, "Surgery of the Lateral Ventricles of the Brain," *Lancet,* vol. 136, pp. 553-555, 9/13/ 1890.
[41] V. M. Srinivasan, B. R. O'Neill, D. Jho, D. M. Whiting, and M. Y. Oh, "The history of external ventricular drainage," *J Neurosurg,* vol. 120, pp. 228-236, Jan 2014.
[42] N. Senn, "Subcutaneous Drainage in the surgical treatment of hydrocephalus internus," *Alienist & Neurol.,* vol. 24, pp. 316-324, 1903.
[43] L. M. Davidoff, "Treatment of hydrocephalus: Historical review and description of a new method," *JAMA Surg,* vol. 18, pp. 1737-1762, 1929.
[44] A. Henle, "Beitrag zur pathologie und therapie des hydrocephalus," *Mitt. ad Grenzgeb. d. Med. u. Chir.,* vol. 1, p. 264, 1896.
[45] G. Sutherland and W. W. Cheyne, "The treatment of hydrocephalus by intracranial drainage," *Br Med J,* pp. 1155-1157, 1898.

[46] E. W. Andrews, "An improved technique in brain surgery. Glass tubes versus gold or platinum for subdural drainage of the lateral ventricles in internal hydrocephalus," *Quarterly Bulletin of the Northwestern University Medical School,* vol. 12, pp. 171-179, 1911.

[47] F. Krause, "Subcutane Dauerdrainage der Hirnventrikel beim Hydrocephalus," *Verh Berl Med Ges,* vol. 39, pp. 213-215, 1908.

[48] A. Kosyrew, "Drainage der Hirnventrikel durch Netzstreifen," *Langenbecks Arch Klin Chir Ver Dtsch Z Chir,* vol. 141, pp. 691-701, 1926.

[49] W. Sharpe, "The operative treatment of hydrocephalus: A preliminary report of forty one patients.," *Am J Med Sci,* vol. 153, pp. 563-571, 1917.

[50] J. V. Pattisapu, E. R. Trumble, K. R. Taylor, P. D. Howard, and T. M. Kovach, "Percutaneous endoscopic recanalization of the catheter: a new technique of proximal shunt revision," *Neurosurgery,* vol. 45, pp. 1361-6; discussion 1366-7, Dec 1999.

[51] A. Torkildsen, "A new palliative operation in cases of inoperable occlusion of the Sylvian aqueduct," *Acta Psychiatrica Scandinavica,* vol. 14, pp. 221-221, 1939.

[52] N. Morota, S. Ihara, and T. Araki, "Torkildsen shunt: re-evaluation of the historical procedure," *Childs Nerv Syst,* vol. 26, pp. 1705-10, Dec 2010.

[53] A. Torkildsen, "A Follow-Up Study 14 To 20 Years After Ventriculocisternostomy," *Acta Psychiatrica Scandinavica,* vol. 35, pp. 113-121, 1960.

[54] F. E. Nulsen and E. B. Spitz, "Treatment of hydrocephalus by direct shunt from ventricle to jugular vain," *Surg Forum,* pp. 399-403, 1951.

[55] F. D. Ingraham, E. Alexander, Jr., and D. D. Matson, "Polyethylene, a new synthetic plastic for use in surgery; experimental applications in neurosurgery," *JAMA,* vol. 135, pp. 82-7, Sep 13 1947.

[56] R. H. Ames, "Ventriculo-Peritoneal Shunts in the Management of Hydrocephalus," *J Neurosurg,* vol. 27, pp. 525-529, 1967.

[57] A. Colas and J. Curtis, "Silicone biomaterials: history and chemistry," *Biomaterials science: an introduction to materials in medicine,* vol. 2, pp. 80-85, 2004.

[58] R. R. De Nicola, "Permanent artificial, silicone, urethra," *J Urol,* vol. 63, pp. 168-72, 1950.

[59] R. H. Pudenz, F. E. Russell, A. H. Hurd, and C. H. Shelden, "Ventriculo-auriculostomy; a technique for shunting cerebrospinal fluid into the right auricle; preliminary report," *J Neurosurg,* vol. 14, pp. 171-9, Mar 1957.

[60] H. D. Portnoy, "New ventricular catheter for hydrocephalic shunts. Technical note," *J Neurosurg,* vol. 34, pp. 702-3, May 1971.

[61] J. Haase and R. Weeth, "Multiflanged ventricular Portnoy catheter for hydrocephalus shunts," *Acta Neurochir (Wien),* vol. 33, pp. 213-8, 1976.

[62] L. N. Sekhar, J. Moossy, and A. Norman Guthkelch, "Malfunctioning ventriculoperitoneal shunts: clinical and pathological features," *J Neurosurg,* vol. 56, pp. 411-416, 1982.

[63] D. Schley, J. Billingham, and R. J. Marchbanks, "A model of in-vivo hydrocephalus shunt dynamics for blockage and performance diagnostics," *Math Med Biol,* vol. 21, pp. 347-68, Dec 2004.
[64] S. Sood, S. Kim, S. D. Ham, A. I. Canady, and N. Greninger, "Useful components of the shunt tap test for evaluation of shunt malfunction," *Childs Nerv Syst,* vol. 9, pp. 157-61; discussion 162, Jun 1993.
[65] S. Nakamura and N. Moriyasu, "Floating ventricular catheter. A new shunting device," *Monogr Neural Sci,* vol. 8, pp. 191-194, 1982.
[66] J. E. Corbett, inventor, "Ventricular catheter," US 4655745 A, Apr 7, 1987.
[67] P. Ruzicka and M. Ruzicka, inventors, "Cerebrospinal fluid shunt system," US 4950232 A, Aug 21, 1990.
[68] R. Bayston and R. D. Milner, "Antimicrobial activity of silicone rubber used in hydrocephalus shunts, after impregnation with antimicrobial substances," *J Clin Pathol,* vol. 34, pp. 1057-1062, 1981.
[69] B. A. Banks, inventor, "Ion beam sputter-etched ventricular catheter for hydrocephalus shunt," Dec 15, 1982.
[70] S. L. Miller and L. Pinchuk, "Porous ventricular catheter," ed: Google Patents, 1988.
[71] J. E. Medow, "The Permeable Proximal Catheter Project: A Novel Approach To Preventing Shunt Obstruction," presented at the American Association of Neurological Surgeons Annual Meeting, Pediatric Section, 2005.
[72] T.-T. Wong, L.-S. Lee, R.-S. Liu, S.-H. Yeh, T. Chang, D. M. Ho*, et al.*, "Hydrogel ventriculo-subdural shunt for the treatment of hydrocephalus in children," in *Hydrocephalus*, ed: Springer, 1991, pp. 438-449.
[73] O. Wichterle and D. Lim, "Hydrophilic gels for biological use," 1960.
[74] D. J. Gower, D. Watson, and D. Harper, "e-PTFE ventricular shunt catheters," *Neurosurgery,* vol. 31, pp. 1132-5; 1134, Dec 1992.
[75] F. Çağavi, N. Akalan, H. Celik, D. Gür, and B. Güçiz, "Effect of hydrophilic coating on microorganism colonization in silicone tubing," *Acta Neurochir (Wien),* vol. 146, pp. 603-610, 2004.
[76] H. H. Chen, J. Riva-Cambrin, D. L. Brockmeyer, M. L. Walker, and J. R. Kestle, "Shunt failure due to intracranial migration of BioGlide ventricular catheters," *Journal of Neurosurgery: Pediatrics,* vol. 7, pp. 408-412, 2011.
[77] K. Sylvia, "AdvaMed Combination Products Workshop Case Study -- Antibacterial Orthopedic and Neurological Devices," in *AHWP Combination Products Workshop*, 2012.
[78] M. J. Ellis, C. J. Kazina, M. R. Del Bigio, and P. J. McDonald, "Treatment of recurrent ventriculoperitoneal shunt failure associated with persistent cerebrospinal fluid eosinophilia and latex allergy by use of an "extracted" shunt," *J Neurosurg Pediatr,* vol. 1, pp. 237-9, Mar 2008.
[79] J. Lin, M. Morris, W. Olivero, F. Boop, and R. A. Sanford, "Computational and experimental study of proximal flow in ventricular catheters. ," *J Neurosurg,* vol. 99, pp. 426-31, Aug 2003.

[80] M. Galarza, A. Gimenez, O. Pellicer, J. Valero, and J. M. Amigo, "New designs of ventricular catheters for hydrocephalus by 3-D computational fluid dynamics," *Childs Nerv Syst,* Aug 6 2014.

[81] M. Galarza, A. Gimenez, J. Valero, O. P. Pellicer, and J. M. Amigo, "Computational fluid dynamics of ventricular catheters used for the treatment of hydrocephalus: a 3D analysis," *Childs Nerv Syst,* vol. 30, pp. 105-16, Jan 2013.

[82] H. L. Brydon, R. Bayston, R. Hayward, and W. Harkness, "Reduced bacterial adhesion to hydrocephalus shunt catheters mediated by cerebrospinal fluid proteins," *J Neurol Neurosurg Psychiatry,* vol. 60, pp. 671-5, Jun 1996.

[83] H. L. Brydon, G. Keir, E. J. Thompson, R. Bayston, R. Hayward, and W. Harkness, "Protein adsorption to hydrocephalus shunt catheters: CSF protein adsorption," *J Neurol Neurosurg Psychiatry,* vol. 64, pp. 643-7, May 1998.

[84] C. A. Harris, J. H. Resau, E. A. Hudson, R. A. West, C. Moon, and J. P. McAllister Ii, "Mechanical contributions to astrocyte adhesion using a novel in vitro model of catheter obstruction," *Exp Neurol,* vol. 222, pp. 204-210, 4// 2010.

[85] S. Suresh and R. A. Black, "Electrospun polyurethane as an alternative ventricular catheter and in vitro model of shunt obstruction," *J Biomater Appl,* vol. 29, pp. 1028-38, Feb 2015.

[86] U. Kehler, N. Langer, J. Gliemroth, U. Meier, J. Lemcke, C. Sprung*, et al.*, "Reduction of shunt obstructions by using a peel-away sheath technique? A multicenter prospective randomized trial," *Clin Neurol Neurosurg,* vol. 114, pp. 381-4, May 2012.

[87] M. A. Williams, J. P. McAllister, M. L. Walker, D. A. Kranz, M. Bergsneider, M. R. Del Bigio*, et al.*, "Priorities for hydrocephalus research: report from a National Institutes of Health-sponsored workshop," *J Neurosurg,* vol. 107, pp. 345-57, Nov 2007.

[88] C. A. Harris, J. H. Resau, E. A. Hudson, R. A. West, C. Moon, A. D. Black*, et al.*, "Reduction of protein adsorption and macrophage and astrocyte adhesion on ventricular catheters by polyethylene glycol and N-acetyl-L-cysteine," *J Biomed Mater Res A,* vol. 98, pp. 425-33, Sep 1 2011.

[89] D. B. Hazer, M. Mut, N. Dincer, Z. Saribas, B. Hazer, and T. Ozgen, "The efficacy of silver-embedded polypropylene-grafted polyethylene glycol-coated ventricular catheters on prevention of shunt catheter infection in rats," *Childs Nerv Syst,* vol. 28, pp. 839-846, Jun 2012.

[90] S. E. Boergesen, inventor, "Shunt system with coating and flow restricting component exerting a passive and essentially constant resistance to outflow," WO 2005051473 A2, Jun 9, 2005.

[91] C. A. Harris and J. P. McAllister, 2nd, "Does drainage hole size influence adhesion on ventricular catheters?," *Childs Nerv Syst,* vol. 27, pp. 1221-32, Aug 2011.

[92] U. W. Thomale, H. Hosch, A. Koch, M. Schulz, G. Stoltenburg, E. J. Haberl, *et al.*, "Perforation holes in ventricular catheters--is less more?," *Childs Nerv Syst,* vol. 26, pp. 781-9, Jun 2010.
[93] H. J. Ginsberg, A. Sum, J. M. Drake, and R. S. Cobbold, "Ventriculoperitoneal shunt flow dependency on the number of patent holes in a ventricular catheter," *Pediatr Neurosurg,* vol. 33, pp. 7-11, Jul 2000.
[94] H. J. Ginsberg, J. M. Drake, T. M. Peterson, and R. S. Cobbold, "Recanalization of obstructed cerebrospinal fluid ventricular catheters using ultrasonic cavitation," *Neurosurgery,* vol. 59, pp. ONS403-12; discussion ONS412, Oct 2006.
[95] B. Tavakoli, X. Y. Guo, R. H. Taylor, J. U. Kang, and E. M. Boctor, "Detecting occlusion inside a ventricular catheter using photoacoustic imaging through skull," *Proc SPIE Int Soc Opt Eng,* vol. 8943, 2014.
[96] A. J. Dextradeur and D. McCusker, inventors, "Fluid management catheter and methods of using same," US 20130253266 A1, Sep 26, 2013.
[97] A. A. Mohan, A. L. Mohan, and M. J. Bernhard, inventors, "Occlusion resistant catheter and method of use," US 20140288479 A1, Sep 25, 2014.
[98] K. R. Wan, J. A. Toy, R. Wolfe, and A. Danks, "Factors affecting the accuracy of ventricular catheter placement," *J Clin Neurosci,* vol. 18, pp. 485-8, Apr 2011.
[99] S. M. Yamada, R. Kitagawa, and A. Teramoto, "Relationship of the location of the ventricular catheter tip and function of the ventriculoperitoneal shunt," *J Clin Neurosci,* vol. 20, pp. 99-101, Jan 2013.
[100] M. Galarza, A. Giménez, O. Pellicer, J. Valero, and J. Amigó, "Parametric study of ventricular catheters for hydrocephalus," *Acta neurochirurgica,* vol. 158, pp. 109-116, 2015.
[101] C. A. Harris, J. H. Resau, E. A. Hudson, R. A. West, C. Moon, and J. P. McAllister, 2nd, "Mechanical contributions to astrocyte adhesion using a novel in vitro model of catheter obstruction," *Exp Neurol,* vol. 222, pp. 204-10, Apr 2010.
[102] K. Ambarki, O. Baledent, G. Kongolo, R. Bouzerar, S. Fall, and M. E. Meyer, "A new lumped-parameter model of cerebrospinal hydrodynamics during the cardiac cycle in healthy volunteers," *IEEE Trans Biomed Eng,* vol. 54, pp. 483-91, Mar 2007.
[103] J. Ekstedt, "CSF hydrodynamic studies in man," *Journal of Neurology, Neurosurgery, and Psychiatry,* pp. 345-353, 1978.
[104] F. Loth, M. A. Yardimci, and N. Alperin, "Hydrodynamic modeling of cerebrospinal fluid motion within the spinal cavity," *J Biomech Eng,* vol. 123, pp. 71-9, Feb 2001.
[105] J. H. Masserman, "Cerebrospinal hydrodynamics: Iv. clinical experimental studies," *Archives of Neurology & Psychiatry,* vol. 32, pp. 523-553, 1934.
[106] R. D. Penn, M. C. Lee, A. A. Linninger, K. Miesel, S. N. Lu, and L. Stylos, "Pressure gradients in the brain in an experimental model of hydrocephalus," *J Neurosurg,* vol. 102, pp. 1069-75, Jun 2005.

[107] R. D. Penn and A. Linninger, "The physics of hydrocephalus," *Pediatr Neurosurg,* vol. 45, pp. 161-74, 2009.
[108] L. Howden, D. Giddings, H. Power, A. Aroussi, M. Vloeberghs, M. Garnett*, et al.*, "Three-dimensional cerebrospinal fluid flow within the human ventricular system," *Comput Methods Biomech Biomed Engin,* vol. 11, pp. 123-33, Apr 2008.
[109] J. Sotelo, "The hydrokinetic parameters of shunts for hydrocephalus might be inadequate," *Surgical Neurology International,* vol. 3, p. 40, 2012.
[110] E. Frank, M. Buonocore, and L. Hein, "The use of magnetic resonance imaging to assess slow fluid flow in a model cerebrospinal fluid shunt system," *Br J Neurosurg,* vol. 4, pp. 53-7, 1990.
[111] D. Greitz, A. Franck, and B. Nordell, "On the pulsatile nature of intracranial and spinal CSF-circulation demonstrated by MR imaging," *Acta Radiol,* vol. 34, pp. 321-8, Jul 1993.
[112] J. T. Cheatle, A. N. Bowder, S. K. Agrawal, M. D. Sather, and L. C. Hellbusch, "Flow characteristics of cerebrospinal fluid shunt tubing," *J Neurosurg Pediatr,* vol. 9, pp. 191-7, Feb 2012.
[113] C. Kadowaki, M. Hara, M. Numoto, K. Takeuchi, and I. Saito, "CSF shunt physics: factors influencing inshunt CSF flow," *Child's Nervous System,* vol. 11, pp. 203-206, 1995/04/01 1995.
[114] B. M. Adams, M. S. Ebeida, M. S. Eldred, J. D. Jakeman, L. P. Swiler, A. J. Stephens*, et al.* (2015). *Dakota, A Multilevel Parallel Object-Oriented Framework for Design Optimization, Parameter Estimation, Uncertainty Quantification, and Sensitivity Analysis: Version 6.3 User's Manual*.
[115] A. E. Ruggles, Zhang, B, Y, and Peters, S. M, "Positron Emission Tomography (PET) for Flow Measurement," *Advanced Materials Research,* vol. 301-303, pp. 1316-1321, 2011.
[116] D. J. Parker, C. J. Broadbent, P. Fowles, M. R. Hawkesworth, and P. McNeil, "Positron emission particle tracking - a technique for studying flow within engineering equipment," *Nuclear Instruments and Methods in Physics Research Section A: Accelerators, Spectrometers, Detectors and Associated Equipment,* vol. 326, pp. 592-607, 3/10/ 1993.
[117] L. Bauer and D. Hamby, "Relative sensitivities of existing and novel model parameters in atmospheric tritium dose estimates," *Radiation protection dosimetry,* vol. 37, pp. 253-260, 1991.
[118] F. Hoffman and R. Gardner, "Evaluation of uncertainties in radiological assessment models," in *Radiological Assessment: A Textbook on Environmental Dose Analysis*, ed: United States Nuclear Regulatory Commission Washington, DC, 1983, pp. 11dash1-11dash55.
[119] C. A. Steed, D. M. Ricciuto, G. Shipman, B. Smith, P. E. Thornton, D. Wang*, et al.*, "Big data visual analytics for exploratory earth system simulation analysis," *Computers & Geosciences,* vol. 61, pp. 71-82, 12// 2013.

APPENDIX

Appendix A: Calculations

A-1 Reynold's Scaling Calculation for Nuclear Imaging Test

Table A-1 Reynold's Scaling Calculation for Nuclear Imaging Test

	Scaled-up Catheter Model in Sucrose Solution (Experimental)	**Original Catheter in Water (Simulated)**
Inner catheter diameter	$d_1 = 0.25" \approx 0.00635\ m$	$d_2 = 1.5\ mm = 0.0015\ m$
Cross Sectional Area	$A_1 = \pi(0.003175\ m)^2$ $= 3.167 \times 10^{-5}\ m^2$	$A_2 = \pi(0.00075\ m)^2$ $= 1.767 \times 10^{-6}\ m^2$
Fluid Kinematic Viscosity	~37.5% mass fraction sucrose solution @ 20 °C $\rho = 1165 \frac{kg}{m^3}$ (measured) $\mu = 11.8\ cp$ $= 0.0118\ Pa \cdot s$ $\nu_1 = \frac{\mu}{\rho} = 1.013 \times 10^{-5}\ \frac{m^2}{s}$	Water @ 37 °C $\nu_2 = 0.7009 \times 10^{-6}\ \frac{m^2}{s}$
Flow Rate	$Q_1 = 1.27 \frac{mL}{s}$ $= 1.27 \times 10^{-6}\ \frac{m^3}{s}$ (Measured pump flow rate)	$Q_2 = \frac{Re_2\ \nu_2 A_2}{d_2}$ $= 2.076 \times 10^{-8}\ \frac{m^3}{s}$
Velocity at catheter outlet	$V_1 = \frac{Q_1}{A_1} = 0.040\ m/s$	$V_2 = \frac{Q_2}{A_2} = 0.01175\ m/s$
Reynold's Number	$Re_1 = \frac{Q_1 d_1}{\nu_1 A_1} = 25.14$ (laminar)	$Re_2 = Re_1 = 25.14$

Appendix B: Computational Scripts

B-1 OpenFOAM Scripts

B-1.1 Initial Pressure Boundary Conditions (0/p)

```
/*------------------------------- OpenFOAM Header Omitted---------------------------------*\

FoamFile
{
   version     2.0;
   format      ascii;
   class       volScalarField;
   object      p;
}
// * * * * * * * * * * * * * * * * * * * * * * * * * * * * * * * * * * * * * * * * * * * * //

dimensions      [0 2 -2 0 0 0 0];

internalField   uniform 0;

boundaryField
{
   inlet
   {
      type            fixedValue;
      value            uniform 0;
   }
   outlet
   {
      type            zeroGradient;
   }
   walls
   {
      type            zeroGradient;
   }
   outerR
   {
      type            zeroGradient;
   }
   lend
   {
      type            zeroGradient;
   }
   hole0
   {
      type            zeroGradient;
   }
   hole1
   {
      type            zeroGradient;
   }
```

```
    hole2
    {
        type            zeroGradient;
    }
    hole3
    {
        type            zeroGradient;
    }
    .
    .
    .
    hole15
    {
        type            zeroGradient;
    }
    symXY
    {
        type            symmetry;
    }
    symYZ
    {
        type            symmetry;
    }
    front
    {
        type                    empty;
    }
    back
    {
        type                    empty;
    }


}

// ************************************************************************* //
```

B-1.2 Initial Velocity Boundary Conditions (0/U)

```
/*--------------------------------- OpenFOAM Header Omitted----------------------------------*\

FoamFile
{
    version     2.0;
    format      ascii;
    class       volVectorField;
    object      U;
}
// * * * * * * * * * * * * * * * * * * * * * * * * * * * * * * * * * * * * * * * * * * * * * //

dimensions      [0 1 -1 0 0 0 0];
```

```
internalField   uniform (0 0 0);

boundaryField
{
    inlet
    {
        type            zeroGradient;
    }
    outlet
    {
        type            fixedValue;
        value            uniform (0.0033 0 0);
    }
    walls
    {
        type            fixedValue;
        value            uniform (0 0 0);
    }
    outerR
    {
        type            fixedValue;
        value            uniform (0 0 0);
    }
    lend
    {
        type            fixedValue;
        value            uniform (0 0 0);
    }
    hole0
    {
        type            fixedValue;
        value            uniform (0 0 0);
    }
    hole1
    {
        type            fixedValue;
        value            uniform (0 0 0);
    }
    hole2
    {
        type            fixedValue;
        value            uniform (0 0 0);
    }
    hole3
    {
        type            fixedValue;
        value            uniform (0 0 0);
    }
    .
    .
    .

    hole15
```

```
    {
        type            fixedValue;
        value            uniform (0 0 0);
    }
    symXY
    {
        type            symmetry;
    }

    symYZ
    {
        type            symmetry;
    }

    front
    {
        type            empty;
    }

    back
    {
        type            empty;
    }

}

// ************************************************************************* //
```

B-1.3 RAS Properties (Constant/RASProperties)

```
/*------------------------------- OpenFOAM Header Omitted---------------------------------*\

FoamFile
{
    version     2.0;
    format      ascii;
    class       dictionary;
    location    "constant";
    object      RASProperties;
}
// * * * * * * * * * * * * * * * * * * * * * * * * * * * * * * * * * * * * * * * * * * * * //

RASModel        laminar;

turbulence      off;

printCoeffs     off;


// ************************************************************************* //
```

B-1.4 Transport Properties (Constant/transportProperties)

```
/*------------------------------- OpenFOAM Header Omitted---------------------------------*\

FoamFile
{
   version     2.0;
   format      ascii;
   class       dictionary;
   location    "constant";
   object      transportProperties;
}
// * * * * * * * * * * * * * * * * * * * * * * * * * * * * * * * * * * * * * * * * * * * * //

transportModel  Newtonian;

nu              nu [ 0 2 -1 0 0 0 0 ] 7.5e-07;

CrossPowerLawCoeffs
{
   nu0             nu0 [ 0 2 -1 0 0 0 0 ] 1e-06;
   nuInf           nuInf [ 0 2 -1 0 0 0 0 ] 1e-06;
   m               m [ 0 0 1 0 0 0 0 ] 1;
   n               n [ 0 0 0 0 0 0 0 ] 1;
}

BirdCarreauCoeffs
{
   nu0             nu0 [ 0 2 -1 0 0 0 0 ] 1e-06;
   nuInf           nuInf [ 0 2 -1 0 0 0 0 ] 1e-06;
   k               k [ 0 0 1 0 0 0 0 ] 0;
   n               n [ 0 0 0 0 0 0 0 ] 1;
}


// ************************************************************************* //
```

B-1.5 Numerical Scheme Definitions (system/fvSchemes)

```
/*------------------------------- OpenFOAM Header Omitted---------------------------------*\

FoamFile
{
   version     2.0;
   format      ascii;
   class       dictionary;
   location    "system";
   object      fvSchemes;
}
// * * * * * * * * * * * * * * * * * * * * * * * * * * * * * * * * * * * * * * * * * * * * //

ddtSchemes
{
   default         steadyState;
}

gradSchemes
{
   default         Gauss linear;
   grad(p)         Gauss linear;
   grad(U)         Gauss linear;
}

divSchemes
{
   default         none;
   div(phi,U)      bounded Gauss upwind;
   div(phi,k)      bounded Gauss upwind;
   div(phi,epsilon) bounded Gauss upwind;
   div(phi,R)      bounded Gauss upwind;
   div(R)          Gauss linear;
   div(phi,nuTilda) bounded Gauss upwind;
   div((nuEff*dev(T(grad(U))))) Gauss linear;
}

laplacianSchemes
{
   default         none;
   laplacian(nuEff,U) Gauss linear corrected;
   laplacian((1|A(U)),p) Gauss linear corrected;
   laplacian(DkEff,k) Gauss linear corrected;
   laplacian(DepsilonEff,epsilon) Gauss linear corrected;
   laplacian(DREff,R) Gauss linear corrected;
   laplacian(DnuTildaEff,nuTilda) Gauss linear corrected;
}

interpolationSchemes
{
   default         linear;
   interpolate(U)  linear;
```

```
}

snGradSchemes
{
    default         corrected;
}

fluxRequired
{
    default         no;
    p               ;
}


// ************************************************************************* //
```

B-1.6 Numerical Solution Definitions (system/fvSolution)

```
/*------------------------------- OpenFOAM Header Omitted---------------------------------*\
FoamFile
{
   version     2.0;
   format      ascii;
   class       dictionary;
   location    "system";
   object      fvSolution;
}
// * * * * * * * * * * * * * * * * * * * * * * * * * * * * * * * * * * * * * * * * * * * * * //

solvers
{
   p
   {
      solver          PCG;
      preconditioner  DIC;
      tolerance       1e-06;
      relTol          0.01;
   }
   U
   {
      solver          PBiCG;
      preconditioner  DILU;
      tolerance       1e-06;
      relTol          0.1;
   }
}
SIMPLE
{
   nNonOrthogonalCorrectors 1;

   residualControl
   {
      p               1e-6;
      U               1e-6;
   }
}
relaxationFactors
{
   fields
   {
      p               0.7;
   }
   equations
   {
      U               0.7;
   }
}

// ************************************************************************* //
```

B-1.7 Parallel Decomposition Definitions (system/decomposeParDict)

```
/*------------------------------- OpenFOAM Header Omitted---------------------------------*\

FoamFile
{
   version     2.0;
   format      ascii;
   class       dictionary;
   object      decomposeParDict;
}
// * * * * * * * * * * * * * * * * * * * * * * * * * * * * * * * * * * * * * * * * * * * * //

numberOfSubdomains 4;

method          scotch;

simpleCoeffs
{
   n               (4 1 1);
   delta           0.001;
}

hierarchicalCoeffs
{
   n               (16 1 1);
   delta           0.001;
   order           xyz;
}

manualCoeffs
{
   dataFile        "cellDecomposition";
}

metisCoeffs
{
}

// ************************************************************************* //
```

B-2 DAKOTA Scripts

B-2.1 Dakota Input File (dakota.in): Example of a single parameter sensitivity study

```
# -------------------------
# DAKOTA Input File
# -------------------------

# Usage:
# dakota.sh -i dakota.in -o run.out > stdout.out

environment
   tabular_graphics_data
      tabular_graphics_file = 'dakota_tabular.dat'

method
  vector_parameter_study
    final_point = 0.7
    num_steps = 10

model
  single

variables
          continuous_design = 1
            initial_point    0.3
            descriptors       'w_th'

interface
          fork
            asynchronous
            evaluation_concurrency = 4
            analysis_driver = 'simulator_script'
            parameters_file = 'params.in'
            results_file    = 'results.out'
            work_directory directory_tag

responses
  num_objective_functions = 1
  no_gradients
  no_hessians
```

B-2.2 Dakota Input File (dakota.in): Example of Latin Hypercube Sampling

```
# -------------------------
# DAKOTA Input File
# -------------------------

# Usage:
# dakota.sh -i dakota.in -o run.out > stdout.out

environment
   tabular_graphics_data
      tabular_graphics_file = 'dakota_tabular.dat'

method
  sampling
    sample_type lhs
    samples = 1000

model
  single

variables
  continuous_design = 5
    cdv_lower_bounds      0.2707 0.2369 0.2073 0.1813 0.1587
    cdv_upper_bounds      0.3309 0.2895 0.2533 0.2216 0.1939
    cdv_descriptors       'r_hi02' 'r_hi03' 'r_hi04' 'r_hi05' 'r_hi06'

interface
            fork
              asynchronous
              evaluation_concurrency = 4
              analysis_driver = 'simulator_script'
              parameters_file = 'params.in'
              results_file    = 'results.out'
              work_directory directory_tag

responses
  num_objective_functions = 1
  no_gradients
  no_hessians
```

B-2.3 Dakota Input File (dakota.in): Example of Local, Derivative-Free Optimization

```
# -------------------------
# DAKOTA Input File
# -------------------------

# Usage:
# dakota.sh -i dakota.in -o run.out > stdout.out

environment
   tabular_graphics_data
       tabular_graphics_file = 'dakota_tabular.dat'

method
  max_iterations = 1000
  max_function_evaluations = 1000
  coliny_pattern_search
    solution_accuracy = 1e-4
    initial_delta = 0.5
    threshold_delta = 1e-4
    exploratory_moves basic_pattern
    contraction_factor = 0.75

model
  single

variables
  continuous_design = 5
    initial_point     0.3008 0.2632 0.2303 0.2015 0.1763
    lower_bounds      0.2707 0.2369 0.2073 0.1813 0.1587
    upper_bounds      0.3309 0.2895 0.2533 0.2216 0.1939
    descriptors       'r_hi02' 'r_hi03' 'r_hi04' 'r_hi05' 'r_hi06'

interface
            fork
              asynchronous
              evaluation_concurrency = 4
              analysis_driver = 'simulator_script'
              parameters_file = 'params.in'
              results_file    = 'results.out'
              work_directory directory_tag

responses
  num_objective_functions = 1
  no_gradients
  no_hessians
```

B-2.4 Dakota Simulator Script (simulator_script)

```
# ---------------------
# Simulator Script
# ---------------------

# In parent DAKOTA directory, copy casebase folder

pwd
cp -rf ../casebase/* .


# Create and execute preProcessing.py script using the inserted parameters of interest

cp preProcessing.py.template preProcessing.py
dprepro --left-delimiter='[[' --right-delimiter=']]' $1 preProcessing.py.template preProcessing.py
python preProcessing.py > preProcessing.log


# Execute OpenFOAM mesh and simulation

blockMesh > blockMesh.log
checkMesh > checkMesh.log
sh run.sh

# or if not using run.sh, uncomment the following:
#decomposePar > decomposePar.log
#mpirun –np 4 topoSet -parallel > toposet.log
#mpirun –np 4 simpleFoam -parallel > simpleFoam.log


# Extract objective function result and pass to DAKOTA results file

python postProcessing.py > postProcessing.log
tail -n 1 case_summary.dat | cut -c 23-  > tmp.txt
mv tmp.txt $2
```

VITA

Sofy Weisenberg is a biomedical engineer, completing a Master's degree and an Interdisciplinary Graduate Minor in Computational Science from the Institute of Biomedical Engineering at the University of Tennessee, Knoxville. Her research efforts have been focused on improving cerebrospinal fluid shunts, specifically the ventricular catheter component of shunts. Mentoring undergraduate researchers and high school students, as well as encouraging more women to take an interest in engineering careers have been some of her most important social goals while at the university. Additionally, she has participated in community outreach with the Graduate Association of MABE (Mechanical, Aerospace and Biomedical) Engineers, bringing STEM activities into local elementary school classrooms through "science day" demonstrations.

Previously, Sofy was employed as a test systems engineer at Pratt & Whitney in East Hartford, Connecticut. While working for the jet engine manufacturer, she was involved in designing parts for use in a jet-fuel ice testing rig, the first of its kind to be utilized in jet engine conformance testing. Along with the project lead, she oversaw the physical construction of the rig and participated in the development of the version which is in use today at Pratt & Whitney's engine testing facilities. She had also been previously employed at Rafael Advanced Defense Systems Ltd. in Haifa, Israel. As an R&D mechanical engineer in the Energy and Optics Integrated Technologies unit, she was exposed to many novel technologies and led several research projects involving the use of smart materials as strain sensors for structural health monitoring.

She completed her undergraduate studies in mechanical engineering at the Technion – Israel Institute of Technology, where she met and married her husband Niv Weisenberg, a fellow mechanical engineer. Her final undergraduate research project focused on optimizing centrifugal pump impeller design for cost reduction, based on fluid dynamics and mechanical design principles. During this time, she held an active role in the mechanical engineering department as a member of the Technion Student Association and took part in many community service projects. Before entering her undergraduate studies, Sofy volunteered for two years of service in the Israel Defense Forces and joined the Education Corps., a unique military unit devoted to educating soldiers. She taught mathematics and English and helped soldiers with learning disabilities earn their high school diplomas while they completed their mandatory army service.